UNIVERSITY OF Southampton

University of Southampton Research Repository
ePrints Soton

Copyright © and Moral Rights for this thesis are retained by the author and/or other copyright owners. A copy can be downloaded for personal non-commercial research or study, without prior permission or charge. This thesis cannot be reproduced or quoted extensively from without first obtaining permission in writing from the copyright holder/s. The content must not be changed in any way or sold commercially in any format or medium without the formal permission of the copyright holders.

When referring to this work, full bibliographic details including the author, title, awarding institution and date of the thesis must be given e.g.

AUTHOR (year of submission) "Full thesis title", University of Southampton, name of the University School or Department, PhD Thesis, pagination

http://eprints.soton.ac.uk

University of Southampton

FACULTY OF ENGINEERING, SCIENCE AND MATHEMATICS

School of Engineering Sciences

Design Optimisation of a Slotless Brushless Permanent Magnet DC Motor with Helically-Wound Laminations for Underwater Rim-Driven Thrusters

by

Shu Hau Lai

Thesis for the degree of Doctor of Philosophy

March 2006

UNIVERSITY OF SOUTHAMPTON

ABSTRACT

FACULTY OF ENGINEERING, SCIENCE AND MATHEMATICS

SCHOOL OF ENGINEERING SCIENCES

Doctor of Philosophy

DESIGN OPTIMISATION OF A SLOTLESS BRUSHLESS PERMANENT MAGNET DC MOTOR WITH HELICALLY-WOUND LAMINATIONS FOR UNDERWATER RIM-DRIVEN THRUSTERS

By Shu Hau Lai

Rim (or tip) driven thrusters with structurally integrated brushless PM motors are now an established technology with an increasing range of applications. In these thrusters, the stator of the motor is housed within the thruster duct, and the rotor forms a ring around the tips of the propeller. Such high pole number motors tend to be very thin radially, have very small axial length to diameter ratios, and have relatively large airgaps to accommodate corrosion protection layers on the surfaces of the rotor and stator. The relatively large diameter stator laminations of such machines tend, therefore, to have a very thin back of core and narrow teeth, which make them expensive and difficult to manufacture. This thesis proposes an alternative motor topology featuring a toothless stator whose laminations are manufactured from a single strip of steel that is edge wound into a spiral.

The electromagnetic design of the motor was optimised for maximum efficiency for a given propeller torque and speed. The airgap flux density in was obtained from an analytical solution of Laplace and Poisson's equations of scalar magnetic potential. Electromagnetic torque was calculated for ideal square wave current distribution. Copper and core losses were estimated in the usual manner. Design of the machine was refined using transient finite element analysis, allowing for rotation of the rotor. The design optimisation revealed that there is an optimum radial thickness for the permanent magnet and number of poles at which the efficiency is maximum. A demonstrator machine was built and tested, and yield a 10% lower efficiency when compared with an existing slotted machine of the same diameter, with an increased volume in the slotless machine of 15%. A cost analysis yielded that the slotless edge-wound laminations are cheaper to manufacture than slotted laser-cut laminations, however the costs of the increased magnet material required are higher. This project has demonstrated a potential cost savings in the manufacture of laminations, however, for this specific thruster application the costs are offset by the need for more magnet material.

Table of Contents

List of Figures

List of Tables

DECLARATION OF AUTHORSHIP

I, Shu Hau Lai, declare that the thesis entitled

Design Optimisation of a Slotless Brushless Permanent Magnet DC Motor with Helically-Wound Laminations for Underwater Rim-Driven Thrusters

and the work presented in it are my own. I confirm that:

- this work was done wholly or mainly while in candidature for a research degree at this University;
- where any part of this thesis has previously been submitted for a degree or any other qualification at this University or any other institution, this has been clearly stated;
- where I have consulted the published work of others, this is always clearly attributed;
- where I have quoted from the work of others, the source is always given. With the exception of such quotations, this thesis is entirely my own work;
- I have acknowledged all main sources of help;
- where the thesis is based on work done by myself jointly with others, I have made clear exactly what was done by others and what I have contributed myself;
- parts of this work have been published (please refer to Appendix 1)

Signed: ……..

Date:…….

Acknowledgements

I would like to thank Mr. Ian Edwards and Subsea 7 for supporting this project and giving me the opportunity to pursue my doctorate.

I would like to thank Dr. Suleiman Abu-Sharkh for his never-ending support, advice and guidance that he has given me over the course of this doctorate.

I would like to thank the technicians of the School of Engineering Sciences, in particular Mr. Bryan Clarke, for all the help that they have given me and for putting up with all the bother I have given them. I would also like to thank my colleagues, in particular Dennis Doerffel, Alan Sumption, Ashraf Abdul-Rahman, Liza Lam and June Sun for making my experience during the pursuit of this degree more enjoyable and special. I would like to thank TSL Technology Limited for their support in the project in providing parts for building the demonstrator thruster.

I would like to thank my family for giving me the opportunity to be where I am in life, and for all their support and encouragement throughout my endeavours. I would like to thank my girlfriend Pui Yee, for all of her love and support that means so much to me, and for having the patience to put up with me through all my different moments.

Chapter 1 Introduction

1.1 General Introduction

Rim (or tip) driven thrusters with structurally integrated brushless PM motors are now an established technology with an increasing range of applications. In these thrusters, the stator of the motor is housed within the thruster duct, and the rotor forms a ring around the tips of the propeller. Such high pole number motors tend to be very thin radially, have very small length to diameter ratios, and have relatively large airgaps to accommodate corrosion protection layers on the surfaces of the rotor and stator. The relatively large diameter stator laminations of such machines tend therefore to have very thin back of core and narrow teeth, which make them expensive and difficult to manufacture.

One such application of such thrusters is for use on underwater Remotely Operated Vehicles (ROVs). An industry where ROVs have been used for many years is the oil and gas industry. The ROV aids in performing a variety of underwater tasks, many of which cannot be performed by divers. Operational and maintenance costs of ROVs are significant, and there is a drive into looking at methods or new technologies that aid in improving the reliability, efficiency and cost of systems on an ROV. The project described in this thesis proposes an alternative potentially lower cost motor topology featuring a slotless stator whose laminations are manufactured from a single

strip of steel that is edge wound into a spiral, in replacing conventional stator laminations, and then fitted over the windings that are preformed on the outside surface of a non-conducting former.

At low vehicle advance speeds, the performance and efficiency of a propeller is enhanced by the addition of a duct surrounding the propeller[1]. The duct also serves to protect the propeller blades. As mentioned before, the stator of the motor is integrated within the structure of the duct, while the rotor forms a ring around the propeller rim (hence sometimes known as rim driven thrusters), thus resulting in a very compact unit, compared to thrusters with hub electric motors, with comparable efficiency. Conventional thruster systems (hydraulic or electric) consist of a propeller driven by a motor via a shaft.

1.2 Novelty

There has been no attempt at applying the slotless motor topology to tip-driven thrusters, and as such this attempt is made in this work and a study of the use of the slotless motor in tip-driven thrusters is conducted. An additional novelty devised within this research is in the manufacture of the slotless stator laminations as well as the winding of coils on to the stator, where a helical slotless (toothless) stator will be investigated for replacing the conventional stacked lamination method of manufacture for stators. This is done by using a rectangular-sectioned strip of wire edge-wound to form a spiral, much like a

'Slinky' spring. The individual coils of this spiral are then insulated and glued together to form a laminated stator. Winding the coils on a toothless stator is also a difficult task. The windings will also be wound on a non-electrically and non-magnetically conducting former in this research, and the performance of the motor investigated using these methods of manufacture.

1.3 History of the project

Halliburton, a US-based company that provides products and services to the petroleum and energy industries, sponsored this project. This project has been running since 1993, and its objectives were to develop methods and tools to optimise the design of a thruster, as well as to demonstrate the viability of the concept of a tip-driven thruster[2].

To date, these project objectives have been met, with integrated thrusters built and tested in a variety of sizes. The University of Southampton presently has built 50mm, 70mm, 250mm, and 300mm diameter propeller thrusters, which are manufactured under license by TSL Technology Limited. Analytical and computational methods were also developed for both electromagnetic and hydrodynamic designs for this thruster. A sensorless drive system was also developed and tested[3]. This project continues the research and development work to reduce the cost of manufacture of the thrusters.

1.4 Issues addressed in this research

There are a few issues identified with the Integrated Thruster design, which will be shown in the review of thrusters designs in Section 1.6. There are additional issues that involve the manufacture of the Integrated Thruster design, and this research will be concerned with addressing these manufacturing issues. The current motor design for the integrated thruster utilises a toothed brushless DC motor:

a) The motor stator laminations are expensive to make due to the high costs for labour and manufacturing. The typical process involves either laser cutting or stamping lamination shapes out of metal sheets, and manually stacking and gluing these laminations into a stack. In order to reduce the overall costs of producing a motor for the integrated thruster unit, methods need to be found to reduce these labour and manufacturing costs.

b) There is some material waste generated when producing steel laminations from metal sheets. It is advantageous to seek a method of manufacture that will allow less material waste to be generated, hence improving the efficiency of material use and reduce overall costs of production of a motor unit.

1.5 Objectives of this research

With the issues identified in the section above in mind, the original objectives of this research were:

1. To investigate a new motor topology for use with the tip-driven thruster concept with the objective to potentially reduce the costs of producing such a thrusters
2. To build and test this new motor topology

Throughout the development of this project, however, the objectives were refined and developed to be more specific achievables. As such, these achievable objectives are:

1. To develop a combinational approach to designing electric motors for the integrated thruster through the use of analytical and generic Finite Element (FE)/circuit model of brushless Permanent Magnet (PM) motors;
2. To use analytical and FEA tools to optimise the design of a slotless motor for an integrated motor, and investigating the difficulties of manufacture of this topology;
3. To build a demonstrator slotless PM motor thrusters;
4. To test and investigate the characteristics of this new motor design and validate the design results obtained.

1.6 Review of literature on Integrated Thrusters

1.6.1 Brief Description of the Environment

The remotely operated vehicle (ROV)

ROVs range from light vehicles used for observations and inspection (typically less than 100 kg), to medium work class vehicles (typically 800-3500 kg), to heavy work class vehicles (3500-15000 kg)[4]. Typical tasks carried out by ROVs for the oil and gas industry are pipeline inspection and bottom survey, rig inspections, drilling and construction support, repair, maintenance and operations support[5]. On some of these tasks, the ROV would be required to use specially constructed tooling (such as cutters, welders, etc) in order to complete these tasks. This tooling would be fitted on to an ROV vehicle when required. Hence, it is advantageous for thrusters of ROVs to be short in length, in order to maximise the space available on these vehicles to accommodate these additional tooling. Having a short thruster length has the added advantage of minimising the length of the thruster that protrudes beyond the frame of the ROV, and hence prevents the thruster from damage from collisions externally.

For some ROVs, such as medium work class vehicles, their operating depths are as deep as 3000m under the sea, for tasks such as bottom surveys. As such, thrusters designed for such vehicles would need to withstand the enormous water pressure at such depths. Under normal operating conditions for an ROV,

the vehicle is constructed so as to have neutral buoyancy under the water. Changes in depth or lateral motion would then be generated by thrust from the thrusters mounted on them. This neutral buoyancy is achieved by the addition of buoyancy material to the frame of the ROV, in order to provide an up thrust to balance against the weight of the vehicle. In order to keep the costs of the ROV low, having a thruster that is compact and light is advantageous, as buoyancy material is costly. ROVs can have a thruster layout of anywhere between 5 - 8 or more thrusters, depending on the number of degrees of freedom desired for the ROV vehicle. In order to minimise costs by having a minimal thruster layout, it is desirable that the thrusters should produce equal amount of thrust in either direction.

The seabed environment

As most ROV operations take place close to the seabed, there is quite a harsh environment that both the vehicle and the thruster have to endure. Erosion from large volumes of grit and sand in the seawater at the seabed poses a serious problem to the thruster. It is also entirely possible that sand may cause the thruster to seize, if a sufficient volume of sand is collected in the physical air gap between the rotating parts of the thruster. Additionally, the corrosive nature of saltwater poses an additional design issue that needs to be considered, when designing a thruster for use on ROVs.

Thrusters on ROVs

Motor Type	Advantages	Disadvantages
Hydraulic Motors	1. High specific torque	1. Many mechanical parts makes reliability an issue 2. Efficiency of a hydraulic motor system is low
Brushed DC Motors	1. Proven technology 2. Simple control	1. Low specific torque 2. Wear on brushes make reliability an issue 3. Due to brushes there are also interference noises
Induction Motors	1. Robust and inexpensive 2. Technology is well understood	1. Motor size tends to be large for this application 2. Control is complex and expensive
Switched Reluctance Motors	1. Construction is robust and simple 2. Bulk of losses appear on stator which is easy to cool 3. Torque is independent of polarity of phase current which allows the reduction of semiconductor switches in the controller in certain applications 4. Torque-speed characteristics can be tailored	1. Has inherent high torque ripple that causes vibrations and noise 2. High peak currents and high controller chopping frequency can cause electromagnetic interference 3. Higher controller switching frequency also causes higher core losses and the motor requires a more expensive grade of steel

	more easily compared to induction motors or permanent magnet motors	
Brushless Permanent Magnet (PM) Motors	1. Brushes are eliminated hence removing the problems of speed limitation and electromagnetic interference, as well as has a better reliability when compared to Brushed DC motors 2. The armature is on the outside stator which allows better cooling and higher specific outputs 3. Permanent magnet excitation reduces rotor losses and improves efficiency	1. Rare earth magnets are costly 2. Magnets can suffer from corrosion and demagnetization under fault conditions
Variable Reluctance Permanent Magnet (VRPM) Motor	1. High specific torque	1. Suffers from high axial flux losses 2. Technology is not well understood

Table 1: Table showing the comparison of various motor technologies

Table 1 shows a table comparing various motor topologies that could be used as drive for thrusters systems. Conventional thrusters for work class

underwater Remotely Operated Vehicles are driven by hydraulic motors. They are normally used because hydraulic motors are able to produce a higher specific torque when compared to traditional electric motors (such as induction motors). This would mean that if traditional electric motors were used to drive thrusters for ROVs, they would result in a much larger electric thruster unit. This is undesirable, as a larger electric motor would impede the flow of water through the propeller, as well as increase the overall space required on the vehicle to accommodate the thruster unit and increases the overall weight of the vehicle. There are many disadvantages, however, with the use of hydraulic thrusters. Hydraulic thruster systems tend to be significantly less reliable compared to their electric counterparts[6]. This is due to the many mechanical parts in a hydraulic thruster system that tend to wear with time, with broken seals and water leakage into the system being amongst some of the common faults. A hydraulic system breakdown can be very costly because it takes a long time to repair. A typical system breakdown would involve replacing the broken part, followed by flushing the hydraulic system and refilling it with oil, priming and testing the system. This is a process that can take 7-10 hours, and operational costs such as the ROV operator and the ROV support vessel are still being paid during this time.

In addition to this, hydraulic thruster systems are inefficient. Most hydraulic thruster systems have efficiencies that are at less than 53%[5], which is very low when compared to possible efficiencies that may be achieved by an all-

electric thruster system of 80-85% system efficiency. This improved efficiency has implications on other components of an ROV system such as the reduction in size of the transformer, switchgear, and umbilical, due to the required power transmitted for the job.

Advances made in permanent magnet material and alternative electric motor topologies have made the use of all-electric thruster systems feasible. Electric motors can now be designed to have similar efficiencies and torque outputs for a much smaller size compared to traditional electric motors, albeit at a significant increase of cost if expensive rare earth magnets are used. There are many advantages to the use of electric thruster systems. Electric motors used for thruster systems have a linear response of torque to control signal when compared to hydraulic motors that have dead bands at low velocities. This is an important feature for ROV tasks that require better positioning and accurate repeatability of motion, such as tasks like repair, maintenance and construction[7]. Electric thruster systems that use these new electric motor designs become more compact, with the elimination of many parts that are associated with hydraulic thruster systems such as a power pack.

The electric thruster system designed in this project is the tip-driven electric thruster, where the motor is structurally integrated into the propeller and duct. This removes blockage of flow through the propeller, resulting in an improved thrust production for a similar power requirement, as well as allowing for a

shorter thruster length and bi-directional thrust, which are advantageous for thrusters of remotely operated vehicles. A literature search that was conducted on underwater tip-driven electric thrusters for ROVs resulted in a small number of relevant papers and a few patents. A summary of tip-driven thruster designs as well as a summary of some prior literature review presented in a technical report[8] written for this project in the past will now be presented, in order to bring together all the various designs and information available on thrusters that are similar to the work undertaken for this thesis. Some of these thrusters were not designed specifically for ROVs, but they are presented here for completeness. Appendix 1 also contains a list of these tip-driven thrusters described in greater detail.

1.6.2 Tip-driven thrusters

Work has been carried out by various institutions in the design of a tip-driven electric thruster. The earliest found tip-driven propeller thruster design is a patent that was filed by Luwig Kort, in Hannover, in 1940[9] (Figure 1). This patent was on the concept of a tip-driven ducted propeller thruster, with the rotor on a ring around the propeller, and the stator coils housed within the duct of the thruster. On the figure, a is the rotor, b is the stator, c, d and e are possible different bearing arrangements. f is the propeller, and g is the duct. No further details were given on this design.

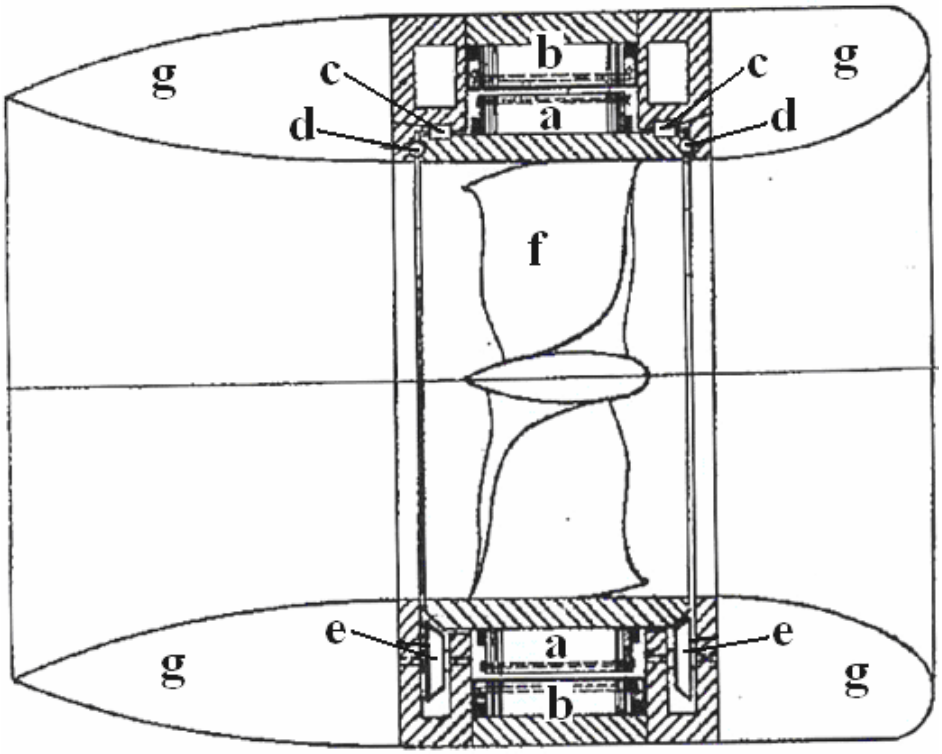

Figure 1: The propeller tip-driven thruster by Kort[9]

Following that, in 1963, a patent for a submarine hydrodynamic control system was filed by F.R.Haselton[10]. This is a patent for a rotating propeller assembly where the propeller blades are mounted externally on the submarine's hull (Figure 2). Through mechanical means, these propeller blades have the ability to change their orientation and thus provide thrust for the submarine in 6 degrees of freedom. The relevance of this design to tip-driven thruster designs is the fact that motion of the propellers in this design utilises a similar concept of a shaftless propeller, with the ring upon which the blades (16) are mounted upon is placed between two field coils (22) which can be energized by any suitable AC power source.

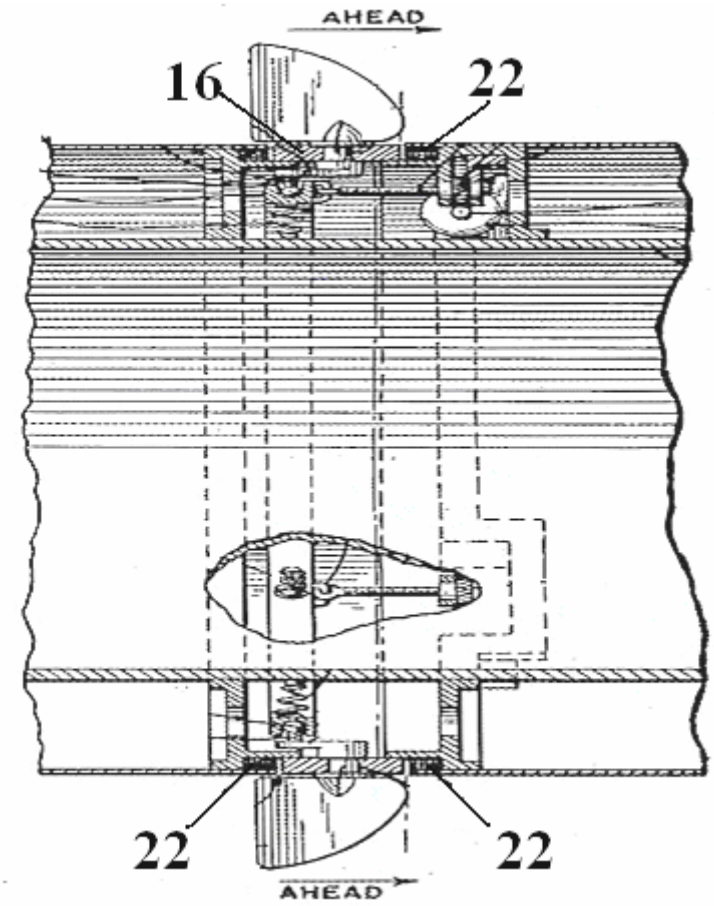

Figure 2: The Haselton thruster[10]

In 1965, a patent filed by G.W.Lehmann (Figure 3) for the structure of a submarine jet propulsion[17] was filed. In effect this design is a jet thruster, by drawing water from outside the vessel and propelling this water by means of two impellers (27a and 27b) and this water is propelled out through a single shaft, as a jet of water (35). The novelty of this design is that the impellers in the jet are shaftless, and similar to that of the tip-driven propeller thruster design, the impellers are driven by a ring (25a and 25b) attached to the tips of

the impeller blades, which is rotated by electromagnetic coils (29a and 29b) in the walls of the duct around the ring.

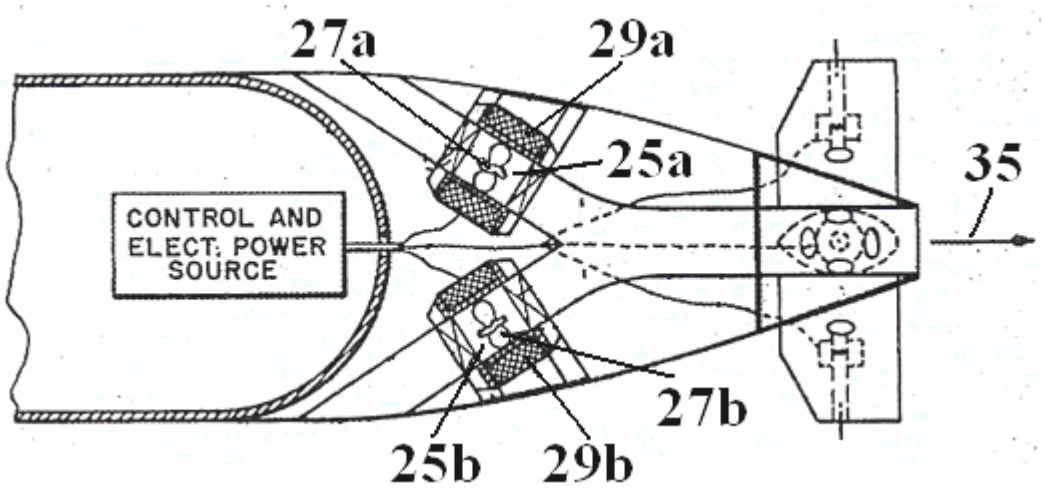

Figure 3: Impeller thrusters designed by Lehmann[17]

Mitsui Shipbuilding and Engineering Company, Limited, filed a patent for an electrically driven propeller in 1976[11] (Figure 4). This is a tip-driven propeller which has an I-shaped guide ring (3) attached to the tips of the blades. A squirrel-cage rotor (9) which contains secondary windings (10) is attached to the periphery of this guide ring, and stator coils (8) are located in the outer duct. This in effect is an induction motor. The bearings (4) for the propeller's rotation are located on a central hub.

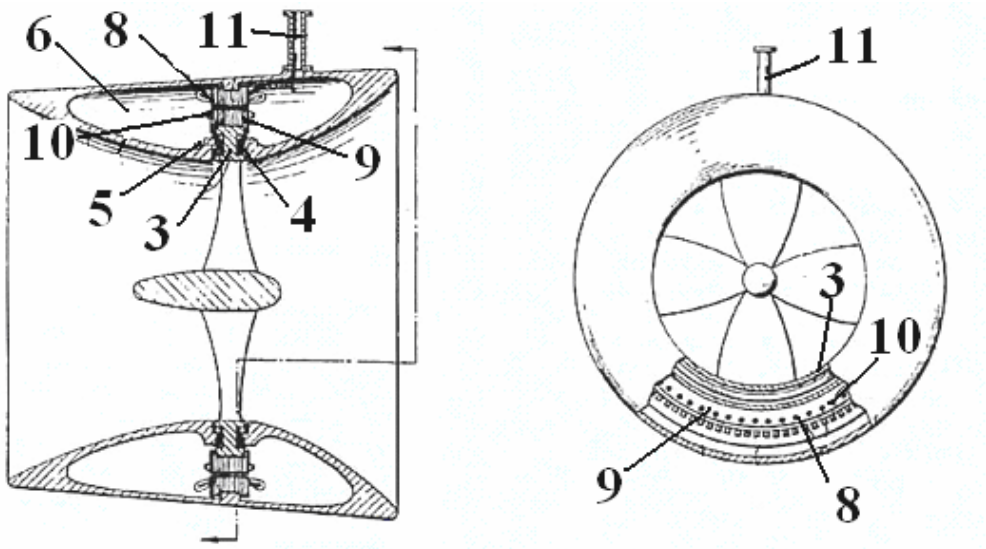

Figure 4: Matsui's tip-driven propeller thruster[11]

Compressed air is supplied into the chamber (6) through a pipe (11) in order to increase the internal pressure of the chamber. This is done in order to prevent leakage of water through the bearings and sealing rings.

Another version for a tip-driven propeller which has its propeller blades attached circumferentially extending beyond the vessel's housing is a thruster design patented by Newport News Shipbuilding and Dry Dock Company[15] (Figure 5). The propeller (22) is mounted on a hub (24) which can be removed from the rotor (30). Two stators (26, 28) are mounted on either side of the rotor. This is done so that the electromagnetic forces can be controlled in order to offset thrust forces and reduce the magnitude of propulsor induced structural vibration. The motor topology used for this thruster design was not

stated however, with the patent specifying that this thruster can either use an induction motor or a PM motor.

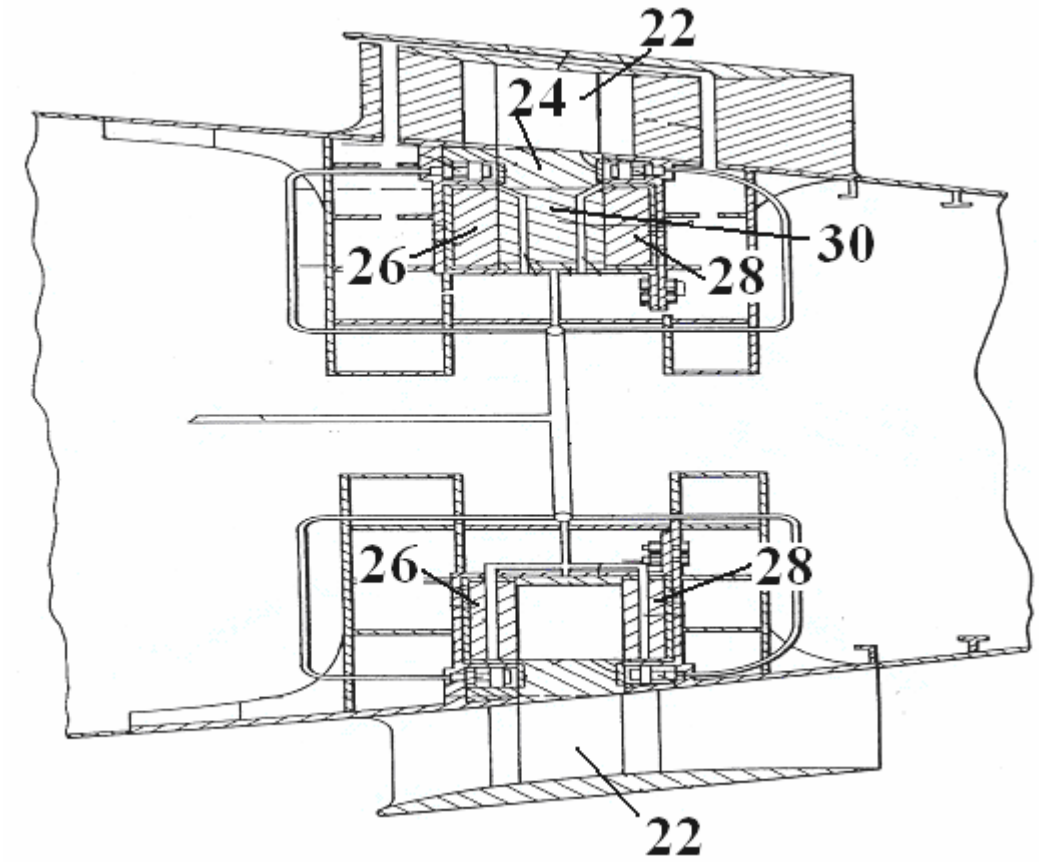

Figure 5: The Newport thruster[15]

A thruster developed by Westinghouse[12] (Figure 6) also uses an induction motor, which has a skewed-bar squirrel cage rotor that is attached to the propeller tips. The rotor propeller is supported by seawater bearings. The shaft and the stator of the motor are fixed to a mounting flange, and the electrical leads from the stator run through the shaft and out of the flange. The entire stator assembly is encapsulated in a laser welded oil-filled metal can. The rotor

core is covered by black epoxy paint. The delivered power for this motor was given to be at 7.5kW, at an operating speed of 2906rpm. This motor has a line voltage of 200V, and is a 16-pole 3-phase machine. It has 48 stator slots and 72 rotor slots, and is 394mm in diameter. It has a 1mm airgap. A disadvantage reported about this design is that the power factor, power density and efficiency were low, due to a significant amount of power lost to friction and eddy currents in the stator.

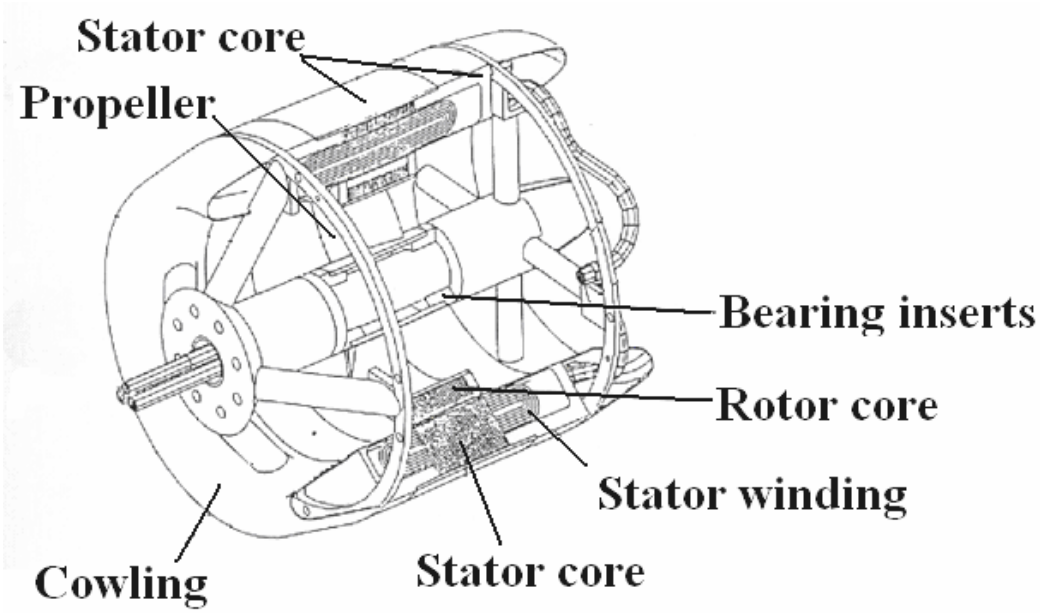

Figure 6: The Westinghouse thruster[12]

Westinghouse also has a second thruster design, which is patented and no references of any papers have been found to be published based on this design. In this design, the coils on the rotor are replaced by permanent magnets. This allowed the designers to have a larger gap between the stator and the rotor, in

which to place a squirrel-cage structure formed from damper bard and conductive wedges which the authors claim will assist in starting the motor as well as to insulate the magnets from harmonic currents which could demagnetise the magnets.

Warwick University describes the design aspects of a prototype switched reluctance motor[14] with a partial stator, that is, without a duct, for use in an integrated thruster. Figure 7 shows this thruster. The motor used is a 3-phase motor, with 6 stator slots and 20 rotor slots. The high number of rotor slots were selected in order to minimise the thickness of the rotor ring. The stator and rotor surfaces were coated with corrosion resistant paint. The stator windings are made of PVC insulated cables. The stator is supported by a fabricated frame. From this frame, two struts that house the propeller shaft bearing assembly, are suspended. This thruster has a propeller of 290mm in diameter. This propeller is mounted inside a brass ring that is fixed to the inner rotor bore. The delivered power was given to be 5kW, at a speed of 1200rpm. This motor has a phase voltage of 250V, and is approximately 466mm in diameter. The motor airgap is 0.6mm. Friction loss in the motor is estimated to be 1.5kW.

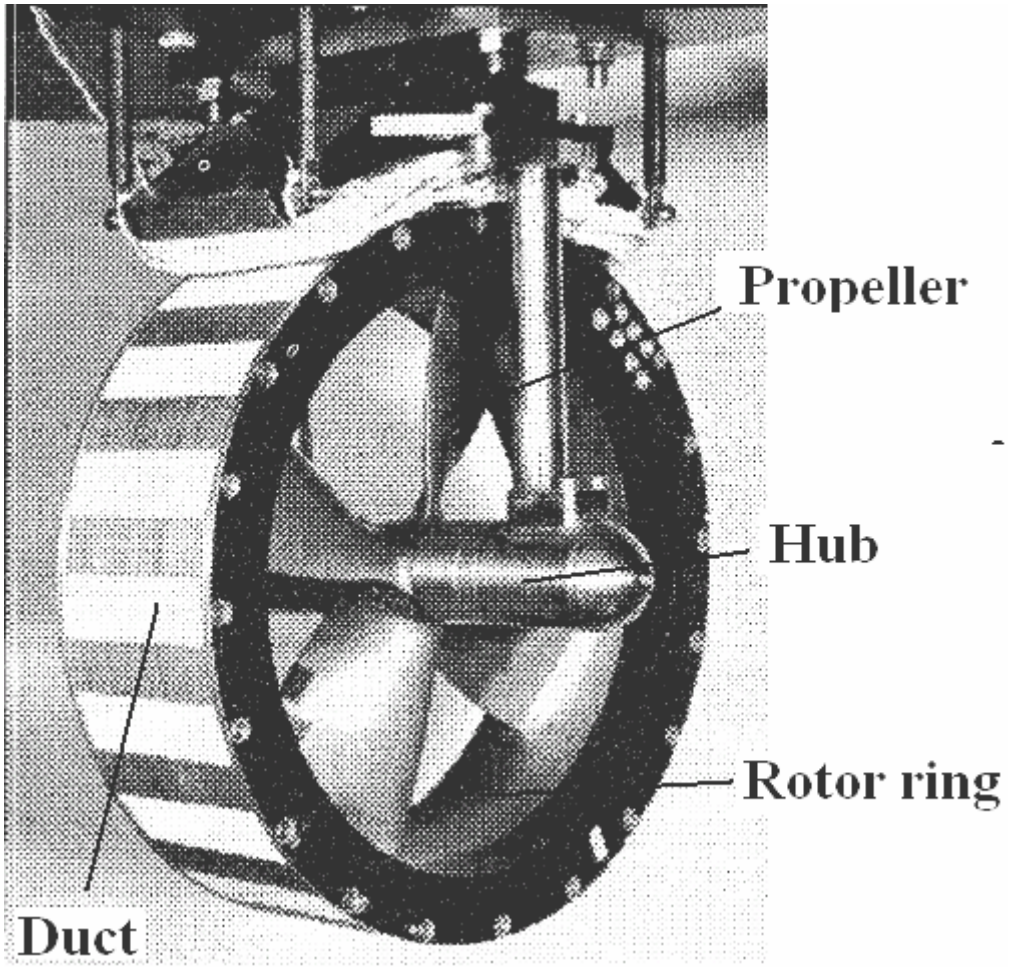

Figure 7: Warwick University Thruster[14]

The Technical University of Gdansk has also developed a ring thruster[19]. They reported having a working prototype of a ring thruster that is supported by magnetic bearings. However, there have been no test results reported, and simulation results written in their publication focuses more on the description and simulation results of the magnetic bearings. The basic description of the motor describes the use of neodymium magnets mounted on a ring around the propeller, which forms the rotor (1); motor windings embedded within a

nozzle that surrounds the rotor/propeller assembly (2), and magnetic bearings supporting the rotor assembly on the circumference of the rotor assembly (3) (Figure 8).

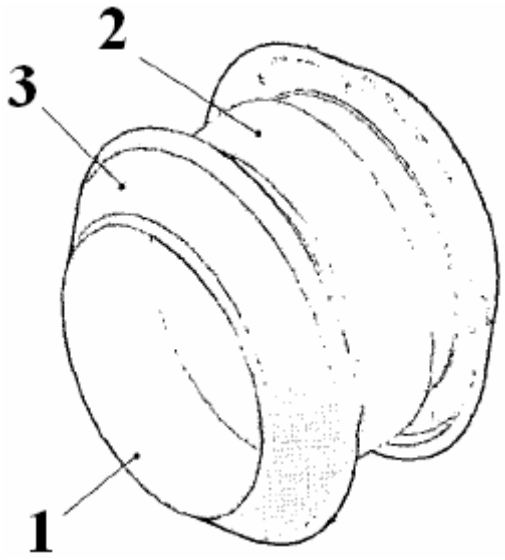

Figure 8: The Gdansk University Thruster[19]

Some of these early demonstrators of such a concept used induction motor (IM)[9, 10, 11, 12] and switched reluctance motors (SRM) with part stators[13]. But these demonstrators suffered from having relatively radially thick rotors and stators, and hence relatively radially thick ducts with high drag losses, which impair hydrodynamic efficiency at high advance speeds. The performance of IM and SRM also tends to be inferior due to the large airgap needed to incorporate corrosion protection layers on the surfaces of the rotor and stator. An axial gap motor has also been explored in the past[14]. The concept of an axial gap motor for use as an integrated motor for underwater thrusters was

proposed and patented, however no additional work or publications have been found on this concept.

In general, permanent magnet machines are well known to be more tolerant of large gaps and and can be designed to have a large number of poles, thus resulting in relatively very thin rotors and stators, yet maintaining good machine efficiency[15]. Given the particular feature of the machine under consideration of 1) thin (<2mm thickness) radial yoke thickness, 2) large airgap, 3) short axial length, 4) large magnetic gap to magnet thickness ratio and 5) high number of poles, all of which increase flux leakage, the choice of a suitable permanent magnet machine topology narrows down to surface magnet machines. Flux concentrating spoke magnet, inset magnet or modulated pole machine (transverse flux or VRPM) topologies suffer from higher magnet flux leakage, in the case of the machine under consideration, and tend to favour being thicker radially, although for machines with larger diameters some of these topologies may become more attractive. Flux weakening is not a desired feature in this application and therefore the poor flux weakening capability of a surface magnet machine is not a disadvantage. There have been designs in the past that utilise the permanent magnet machine for the integrated thruster concept.

Harbour Branch Oceanographic Institution (HBOI) developed an integrated thruster[16]. It is a permanent magnet integrated thruster,with the rotor ring is

fixed to the tips of the propeller, and has bearing races on both sides, which are matched on the stator. Plastic balls and spacers are placed within these races, and this assembly forms thrust bearing which act in the axial direction. The hub of the propeller has been removed in this design, providing an advantage in reducing entanglement by external objects in the propeller. The stator is potted in solid epoxy. The input power is 560W, and the motor has a phase voltage of 28V. The motor current is 20A, and is 533mm in diameter. The thrust produced from this thruster is 318N.

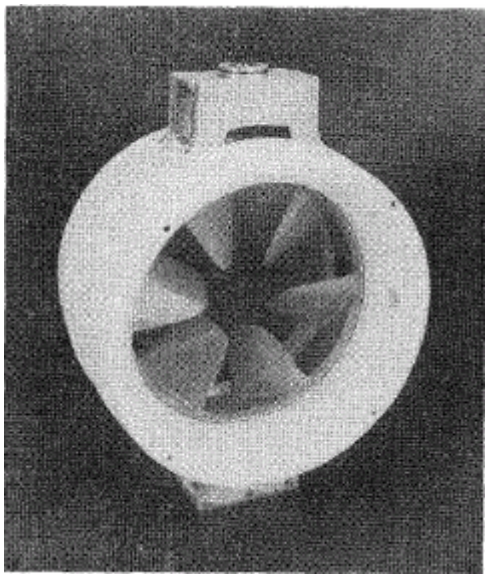

Figure 9: Harbour Branch Oceanographic Institution Thruster[18]

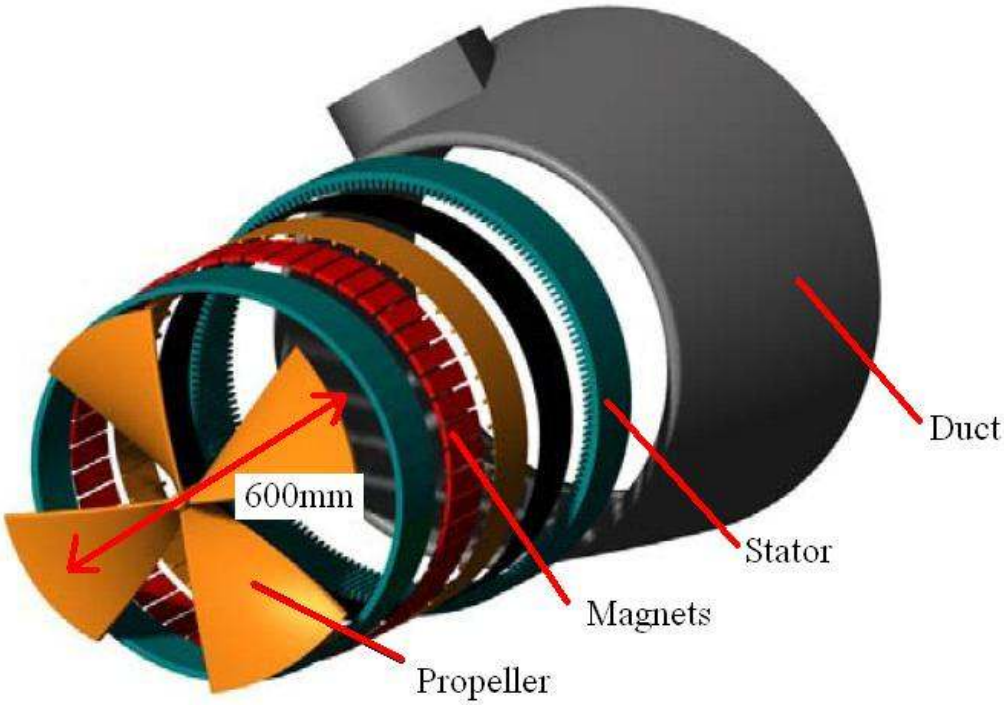

Figure 10: The NTNU Integrated Thruster[20].

NTNU of Norway has built and tested a prototype integrated motor for use with ship propulsion[17] (Figure 10). This design is similar with the design by HBOI where the bearings for supporting the propeller-rotor are located on the rim of the rotor. The thruster built has a 600mm diameter propeller, and is rated to run at 100kW at 700rpm, while drawing a winding current of 150A.

The tip-driven thruster design has generated some commercial interest over recent times as well. Schilling Sub-Atlantic Alliance[18] have a hubless ring thruster, which is based on the HBOI design, that has a width of 480mm, depth of 230mm, and a height of 610mm. They claim that the thruster produces a peak thrust of 2001N (204kgf) at a rated speed of 1,000rpm. Podded rim

driven thrusters with MW ratings are also under development by General Dynamics Electric boat for large manned submarines and ship propulsion[19, 20]. The NTNU thruster design has been further developed by Rolls-Royce[21] for an offshore support vessel. TSL Technology Limited currently have a license from the University of Southampton to produce the university's tip-driven thruster (also known as the integrated thruster) designs commercially.

Figure 11 shows a cross-sectional drawing of a Southampton Integrated Thruster design.

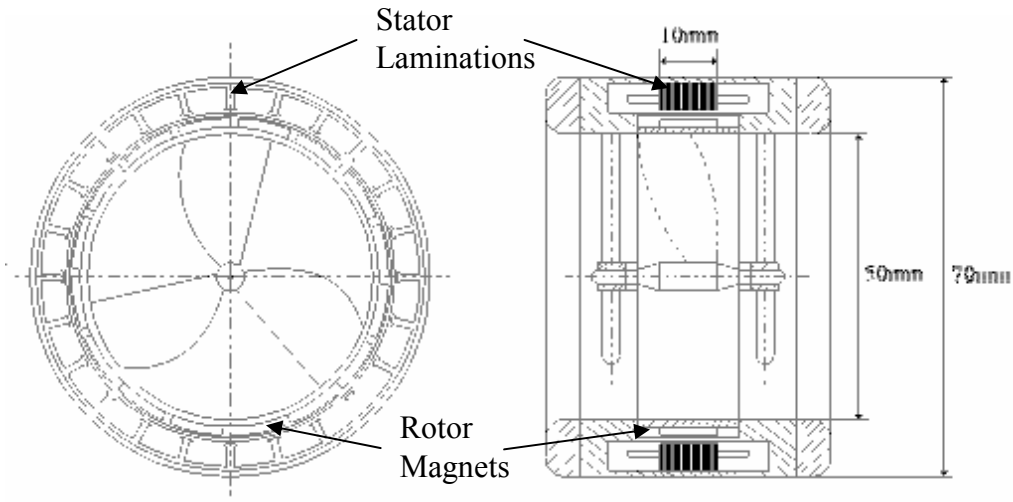

Figure 11: Cross-sectional drawing of the Integrated Thruster

The rotor steel yoke is formed as a ring around the propeller blades, with the tip of the blades welded to the ring. Permanent magnet (PM) pole pieces are mounted on this ring. The stator steel yoke and the windings of the motor are

encapsulated within the duct that surrounds the propeller. In this arrangement, both rotor and stator components fit within the volume of the duct and so do not project into the flow region of the duct, hence minimising its effects on the hydrodynamic performance of the propeller. These motor components are completely encapsulated with the use of epoxy resins, and hence there is no need for a pressure compensated housing and rotating seals. This improves the reliability and cost of the motor[8]. The propeller is supported on both sides by central hub bearings, which in turn are supported by pre- and post-swirl propeller stators. The bearings are located in a pressure-compensated oil chamber. To date, the University of Southampton has developed integrated thrusters of these types at various sizes, ranging from 50mm propeller diameter thrusters to 300mm propeller diameter thrusters. Some of these designs pose specific design issues.

Publications on a 50mm integrated thruster design[16, 22] report on the design of a 50mm propeller diameter thruster designed, built and tested at the University of Southampton. In this design, a slotted permanent magnet motor was designed to fit within a very small and thin duct, resulting in a steel yoke thickness of 1.25mm. The design is able to produce an output thrust of 9.81N (1kgf) at an input power of 63W.

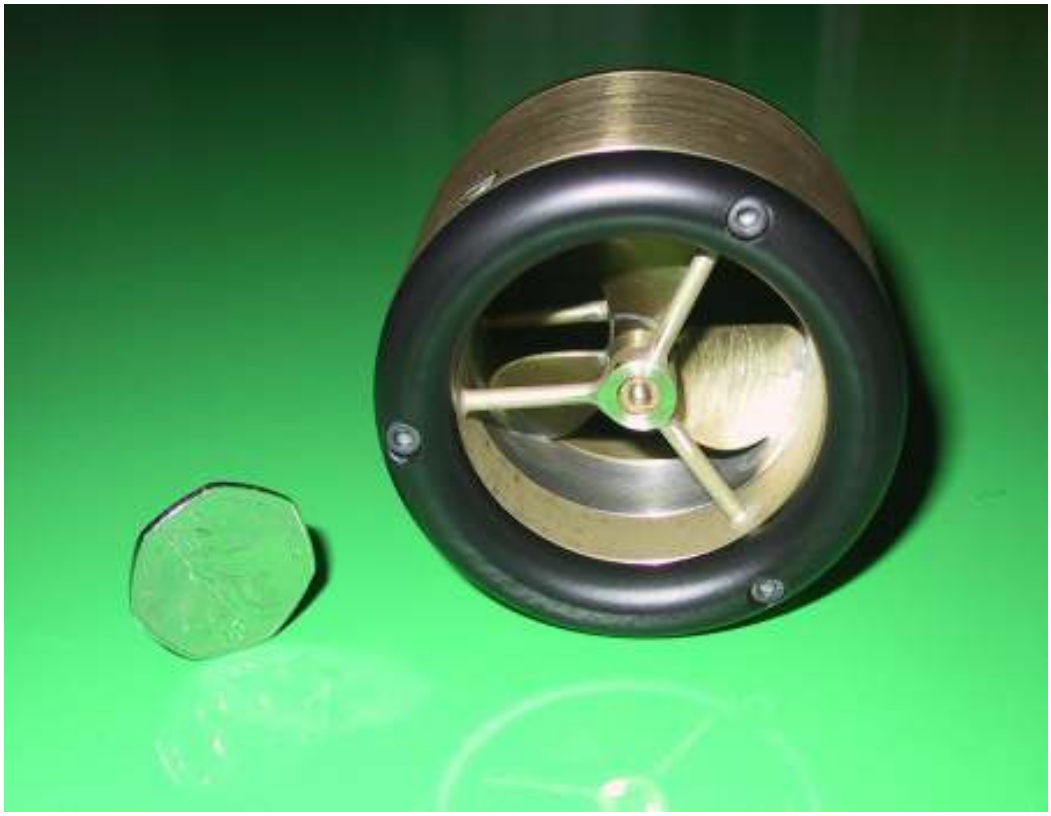

Figure 12: Southampton 50mm diameter propeller thruster

Other publications from the University of Southampton on their thruster designs focus on a 250mm diameter propeller design[1, 25, 23]. The thruster has been tested and is able to produce a peak thrust of 981N (100kgf) at an input power of 5.5kW.

The main advantage of the Integrated Thruster design is that the components of the motor are relocated into the interior of the duct, and this improves the hydrodynamic properties of the thruster. This allows additional protection to the motor, and aids in strengthening the duct. Water flow paths to the propeller

are improved, hence improving the efficiency. The motor is well cooled, with short thermal paths between the hot spots of the motor and the surrounding water.

Additionally, all the available diameter of the thruster is utilised. This provides an advantage from an electromagnetic point of view, since motor output power is approximately proportional to its volume. This allows the thruster to be made short, and yet provide the required output power.

There are some disadvantages to having a large diameter and short axial length of the motor, however. Peripheral rotor speed, and hence friction loss in the clearance gap between the rotor and the stator are increased. There is also a high proportion of end winding ohmic loss, due to a relatively high ratio of end winding length to motor length. The electromagnetic air gap of the motor is large, relative to the overall diameter and length of the motor, due to the need to accommodate protective coatings to protect the motor components from seawater, as well as the physical gap. This results in high proportion of peripheral and axial fringe fields that increase losses, as well as requires a larger rotor steel yoke[1, 2, 4, 26, 24].

These disadvantages present a challenge for the design of the Integrated Thruster. The advantages of this design, however, make it very feasible and support the development of thrusters of this kind.

1.7 The thesis

In this chapter, an introduction to this research and thesis has been presented. The motivation, objectives, and novelty of this project have also been presented. In Chapter 2, a more detailed description of the slotless motor topology designed in this research as well as the motor specifications, quantities and terms used will be presented to provide the reader with a better picture of the motor presented here. This thesis will then move on to begin to describe the design process for the slotless motor topology, beginning with Chapter 3 that details the analytical and computational methods used. Chapter 4 then describes the optimisation and results obtained for the design optimisation process. Chapter 5 describes the practical issues to be considered when moving a design into real life manufacturing, and will present the demonstrator slotless thruster developed. Experimental results and discussion will be detailed at the end of Chapter 5, along with comparisons between the results obtained for this prototype and an existing slotted design. Finally, Chapter 6 presents the main conclusions and findings from this work.

Chapter 2 Slotless Motor Topology and Specifications

In this chapter the slotless motor topology and its specifications will be discussed in more detail. The design issues and constraints of the design will also be discussed. Prior to these discussions, it is prudent to discuss the slotless motor concept and define the symbols and dimensions that will be used in the design optimisation.

2.1 Description of the slotless motor concept

The slotless brushless permanent magnet motor design will be reviewed briefly in this section. This is essentially a permanent magnet (PM) machine without slots for the armature windings; the windings are wound on the surface of the stator.

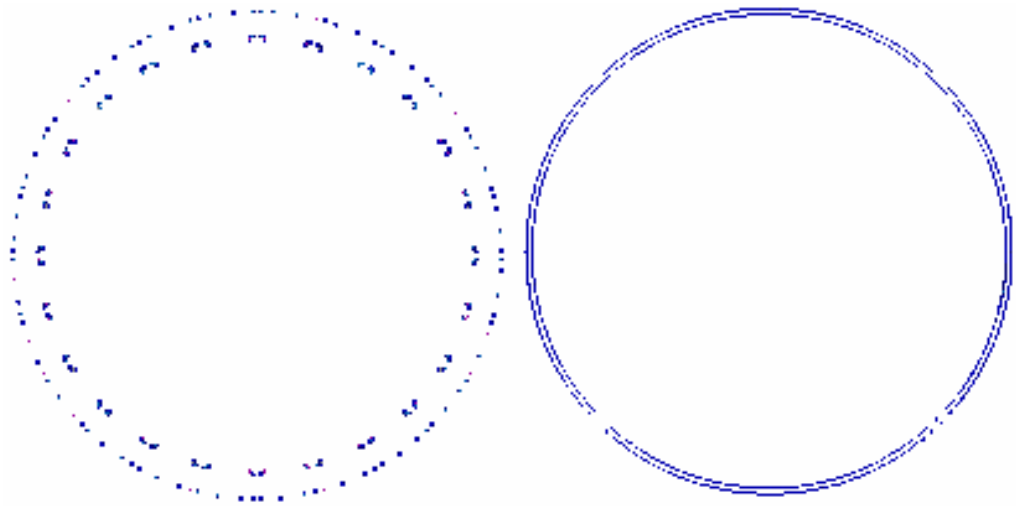

Figure 13: Illustration of a slotted stator (left) and a slotless stator (right)

The novelty of the use of this topology is two-fold. The first is that there has not been a slotless brushless permanent magnet motor designed for use as a drive for underwater thrusters. The second is that there has not been very much work done on developing a radial-flux slotless brushless PM machine that has a very small axial length to radius ratio, and that uses an edge-wound strip to form a helical lamination.

The main advantage to be explored with the use of a slotless machine design is the reduction in manufacturing costs and its simplicity in manufacture, compared to the manufacturing costs of a slotted brushless PM machine. The production of a laminated stator is an expensive process, with steel laminations cut out from sheets of steel, and these laminations are normally manually stacked together and glued. There also tends to be some material waste in this process, as there are a finite number of laminations that can be cut from a single sheet of steel. Within this research, these costs could potentially be reduced by employing a spirally wound slotless stator (to be discussed in Chapter 5).

The concept of a spirally wound stator is not a new one, with patents existing for a spirally wound slotted stator[25, 26, 27, 28]. A radial-flux spirally wound slotless stator is a fairly new design, however, in particular in the integrated thruster application where the motor needs to be radially large and axially short. The spirally wound stator involves the manufacture of the stator

laminations by winding a strip of steel in a helical edge wound fashion (like a Slinky). This allows a potential reduction in costs for the manufacture of stator laminations due to the simplicity of the design and the potential reduction in labour required and material wastes generated when compared to conventional stator laminations.

One issue with this method of stator manufacture is to do with the choice of materials used. Typical electrical steels used for stator manufacture contain 6-6.5% silicon. When the silicon content in an Fe-Si allow exceeds 4%, the material is known to become brittle[29]. This poses difficulties in the actual manufacture of the helical winding of the stator, as the material becomes too brittle to withstand the stresses formed from edge-winding the steel. As such, mild steel was chosen for use to manufacture the helical stator. One advantage in the use of mild steel is in the lower cost of mild steel material when compared to electrical steels, hence lowering overall costs; the performance of the motor using mild steel has been shown in testing the demonstrator motor (which will be further shown and discussed in Chapter 5) to have very small steel core losses, showing an acceptable use of mild steel in forming the helical laminations.

A slotless motor design also has the advantage of the elimination of the tooth ripple component of cogging as well as has little slot harmonic effects[30, 31, 32, 33]. Cogging is one of the disadvantages faced in the slotted motor design, as it

causes a ripple in the torque generated by the motor. A slotless machine, however, suffers from a generally lower magnetic flux crossing the motor airgap, this could result in a lower power output in the slotless design compared to an equivalent slotted design. As such, although iron losses in a slotless motor is inherently less than in an equivalent slotted design, due to difficulties in obtaining a similar power output for a particular input power, for a slotless design of equivalent volume to that of a slotted design, the slotless motor is less efficient.

Another characteristic of the slotless motor is that it has low winding inductance[34, 35, 36] because the magnetic gap is necessarily large, and slot leakages are absent. This has implications on the performance of the motor, as well as in the design of a suitable controller for the motor because the energy trapped in the windings are small. A faster current response can be expected[37]. Although a lower inductance generally means a lower VA rating demand on the motor drive, the faster current response does imply a faster current chopping control required (in the case of PWM controlled drives) hence requiring fast switching transistors which may result in higher switching losses[37]. [36] has also reported that this lower winding inductance makes the slotless motor more suitable to be controlled by a sensorless drive. If the rotor position of the motor is obtained by a terminal-voltage-detector instead of a typical position sensor, there is a higher accuracy of detected position resulting from a smaller winding inductance. This has implications on the components

required for the thruster. A sensorless drive results in the reduction of components on the motor (Hall sensors), and allows a more compact and lighter unit to be built compared to one driven by Hall sensors. This improves reliability due to having less components that may fail. However, a position drive normally requires additional circuits in order to measure voltage and current outputs from the motor as well as processing these signals, hence increasing costs on the inverter drive.

Cooling is not an issue with this particular motor, as the windings of the motor are placed in the airgap. The windings are placed in the path of the water flow and are encapsulated within a protective housing. This placement of windings allows for a better cooling, hence allowing for a higher electric loading in the motor.

However, there are also certain disadvantages associated with the design of a slotless PM motor. The main disadvantage of a slotless motor design is that in order to produce the same amount of torque as a certain rated conventional machine, thicker magnets are required in order to make for the reduction of magnetic flux density in the slotless motor due to the lack of teeth. A major flux path is the airgap, which tends to be large and hence has a high reluctance. This indicates that some of the cost saved in manufacturing costs may be taken up in the cost for additional magnet material. In the case of the demonstrator built for the slotless thruster, 4.5mm thick magnets were used

compared to that of the slotted design compared with, which had 3mm thick magnets. Table 2 summarises the advantages and disadvantages discussed here.

Advantages	Disadvantages
Elimination of tooth ripple and has little slot harmonic effects	Lower magnetic flux crossing to the stator surface resulting in lower power factor (or additional magnet material required)
Lower iron losses compared to the slotted design	Lower efficiency compared to equivalent slotted design due to lower magnetic flux crossing the airgap
Lower winding inductance leading to potentially lower VA rating on drive controller	Lower winding inductance may lead to higher drive losses due to higher switching frequency. This needs to be investigated further
Faster current response due to lower winding inductance leads to the motor being better suited for use with sensorless control – eliminating the need for Hall sensors in the motor and improving reliability of the machine by removing a component	Sensorless control requires more power electronic control hence leading to a potentially more expensive drive
Good cooling of windings leading to ability to have higher electric loading	

Table 2: Advantages and disadvantages of the slotless motor

The helical-wound slotless motor design merits consideration for use with the integrated thruster, as there are potential reductions in stator manufacturing costs that could be achieved due to the simplicity of design. Moreover, there are some indications that the slotless motor may be more suited for use with the integrated thruster design due to the large airgap, short motor length

conditions, where the slotless motor inherently has a large airgap due to the absence of teeth.

2.2 The slotless motor topology and specifications

The slotless brushless permanent magnet motor in this project was designed such that comparison with an existing slotted motor design could be made, for the integrated thruster application. The availability of an existing 70mm propeller diameter slotted motor thruster made it a convenient choice for use as a comparison. As such, the slotless motor in this project was designed around a 70mm diameter propeller.

There are also several dimensional constraints in the design of the motor that were imposed in order to produce a motor of equivalent size for comparison with the slotted design. These constraints were the outer motor diameter (stator outer diameter), with a diameter of 104mm, the inner motor diameter (rotor inner diameter), with a diameter of 73mm, and the physical airgap between the rotor and the stator of 4mm. The characteristics of the 70mm slotted thruster will be compared with the slotless thruster in Chapter 5.

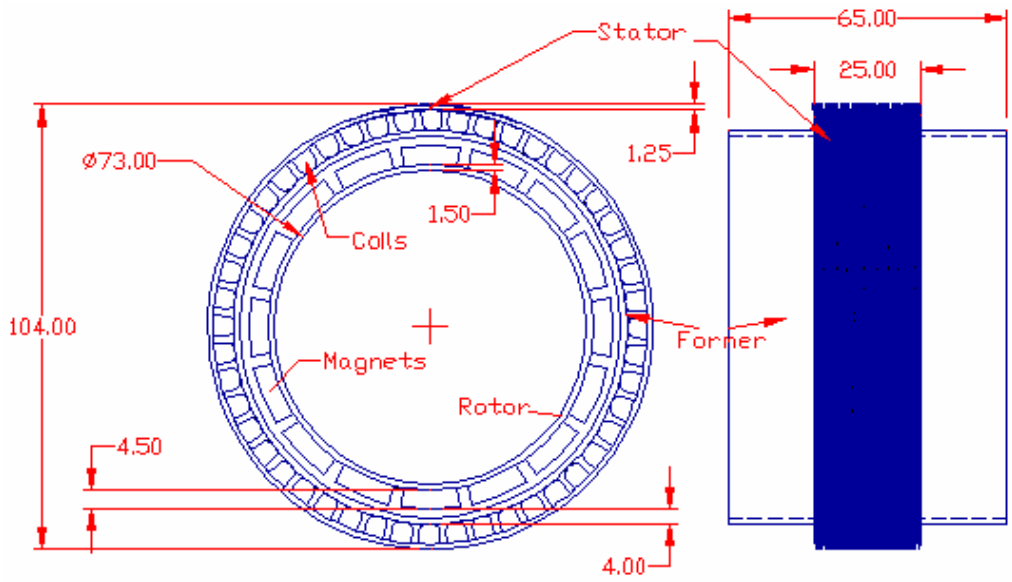

Figure 14:Drawing of the slotless motor designed for this project

Figure 14 shows a drawing of the slotless motor designed for this project. The stator consists of an edge-wound helical arrangement of steel. This sits on top of the copper coils that are wound around a former that is made out of the nylon material Delrin. The rotor is supported by struts that are attached to the thruster body (refer to Figure 38 in Chapter 5 for a view of the thrusters assembly). Table 3 shows a summary of the design's specifications.

Motor parameter	Value
Overall available length	30mm
Stator Outer Diameter	104mm

Rotor Internal Diameter	73mm
Electromagnetic airgap	4mm
Number of phases	3
Nominal torque	0.68Nm
Nominal speed	3600rpm

Table 3:Summary of the slotless motor specifications

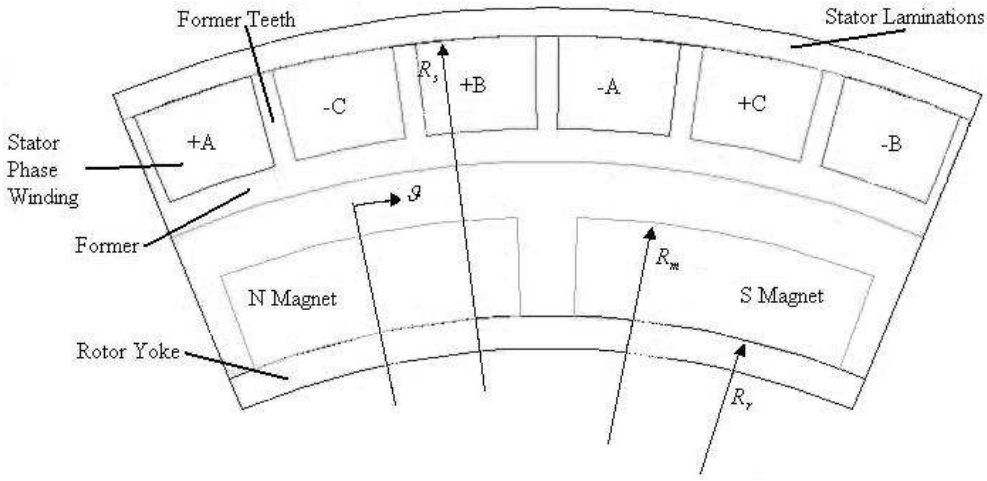

Figure 15: Design dimensions

Figure 15 shows a 2-pole radial section of a slotless motor and the symbols that are used to define basic dimensions. All radii measurements (given the symbol R with subscripts indicating measurements to different motor surfaces) are with respect to the axis of the motor. Table 4 below provides a description of the main parameters used in this thesis. Any other symbols that are used in

subsequent chapters of this thesis that are not covered by this table will be defined appropriately in that particular chapter.

Symbol	Description	Units
R_s	Radius of the stator bore	Metres, m
R_r	Radius measured from the axis to over the rotor yoke surface	Metres, m
R_m	Radius measured from the axis to over the magnet surface	Metres, m
ts	Stator yoke thickness	Metres, m
tr	Rotor yoke thickness	Metres, m
l_m	Magnet thickness	Metres, m
α_p	Magnet pole-arc to pole-pitch ratio	
p	Number of pole pairs in the motor	
n	Number of harmonics	
ϑ	Peripheral angle	Radians, rad

Table 4:Nomenclature

2.3 Design issues and constraints

There are a number of design issues and constraints that need to be considered when designing the slotless motor for the integrated thruster. The motor is designed for maximum efficiency, with torque output and rotational speed determined through matching the motor with the thruster propeller.

Short axial length

The motor length is chosen so as to achieve a good motor efficiency. The longer the axial length of the motor, the higher the efficiency of the motor, however there is a certain length beyond which the efficiency only increases slightly with increasing motor length. A short axial length is also desirable so as to reduce the moment of inertia of the rotor. The propeller and duct lengths limit the maximum length of the motor, as hydrodynamic efficiency reduces as the ratio of duct length to propeller axial length increases[8].

An additional advantage of a short axial length is this provides more space available on board the ROV for tooling, depending on the tasks the ROV is commissioned to. This also keeps the thruster length within the ROV chassis, which protects the thruster from the external environment such as collisions with rocks, and to increase the manoeuvrability of the vehicle.

Thin motor requirement

The thruster utilises a thin short duct around the propeller. A thin short duct has a better hydrodynamic efficiency compared to a long or fat duct[8]. This, however, places a constraint on the dimensions of the electric motor design, as the motor components are housed within the volume of this duct. The motor needs to be kept thin.

The motor size is minimised by careful selection of the number of poles as well as the thickness of the magnet poles, in order to minimise the motor steel whilst maintaining the torque production of the motor.

Large electromagnetic airgap

The electromagnetic airgap of the motor is relatively large when compared to the length of the motor. This is unconventional[38]. However, it is necessary, as this space is needed to accommodate a protective coating that encapsulates both the rotor and the stator components, in order to isolate and protect these components from the harsh seawater environment. This protective coating, together with the actual physical gap that is required to separate both the rotating and stationary components, results in a large electromagnetic airgap constraint that needs to be considered when designing this integrated motor.

2.4 Design considerations

Propeller Matching

As mentioned earlier, the motor is designed for maximum efficiency given output torque and rotational speed values. These are normally obtained from matching propeller hydrodynamic characteristics to motor characteristics, and is a very important part of the design process. For a given thrust output, the propeller torque, speed and power can vary considerably with pitch ratio and distribution, blade area ratio, number of blades and blade section shapes, and it is necessary to select these parameters carefully to maximize efficiency of the overall system of propeller and motor. Propeller pitch ratio is the ratio between a propeller's pitch and its diameter. The pitch is the amount that a propeller will advance when rotated one revolution. Figure 16 illustrates a propeller pitch ratio.

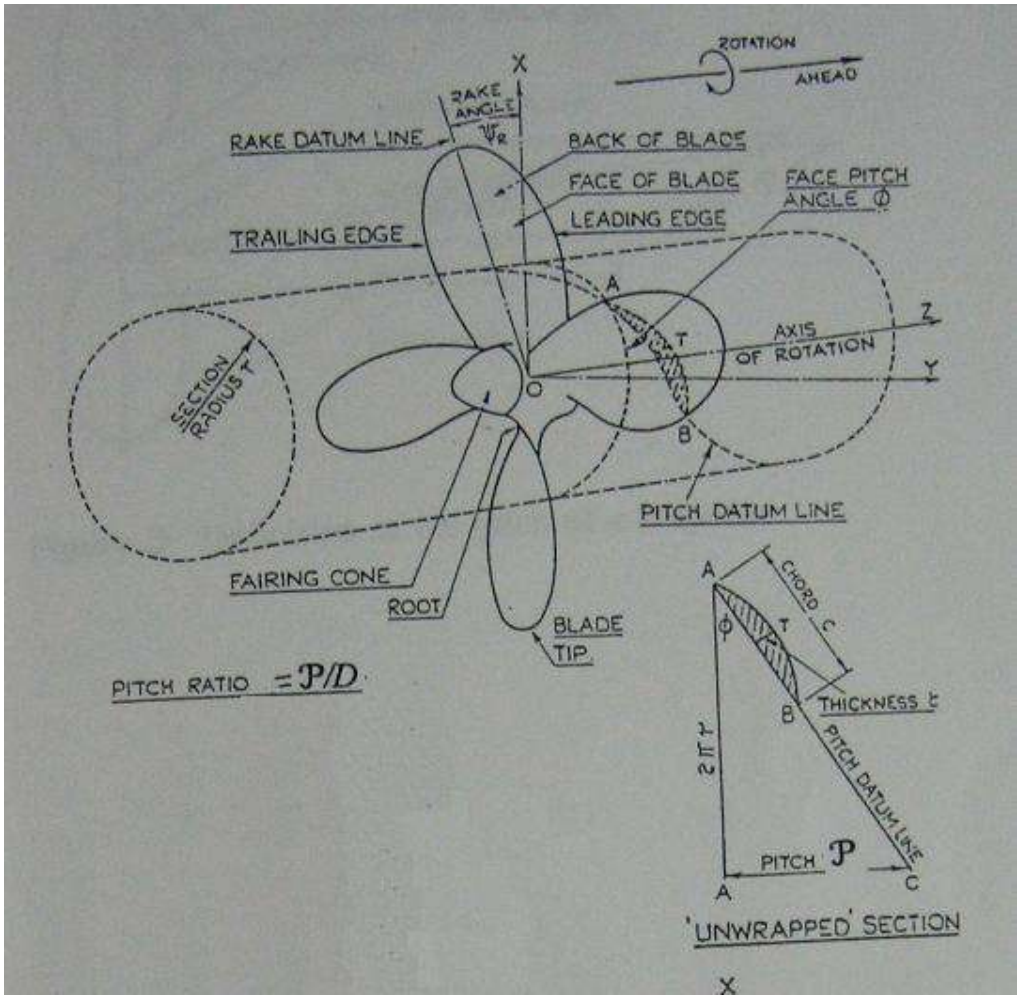

Figure 16: Illustration of propeller pitch ratio[74]

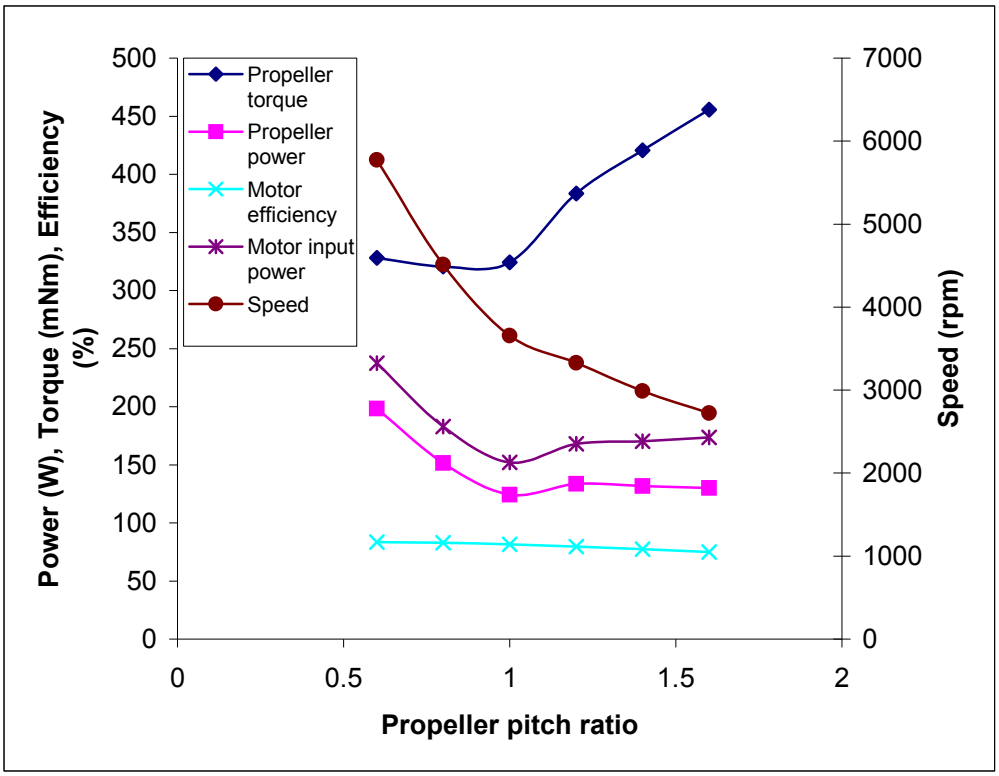

Figure 17:Dependence of motor torque, power, speed, and efficiency on propeller pitch for a propeller diameter of 70mm

Figure 17 illustrates the dependence of motor torque, power, speed and efficiency on propeller pitch, which assumes a symmetrical modified Ka4-70 type propeller in a S2037 type duct, whose characteristics are published in [25]. The propeller has a diameter of 70mm, and is assumed to produce 50N of thrust at bollard pull. Motor efficiency is the motor electromagnetic efficiency. As propeller pitch increases motor torque and hence current and associated ohmic loss increase. However, increasing the pitch reduces propeller speed

thus reducing friction and core losses, which are proportional to the cube and the square of speed, respectively.

There is a tendency for a motor designer to select a low pitch ratio to minimise torque and maximise speed. However, from Figure 17 it can be seen that that would not be the best choice. In fact, a propeller pitch ratio of 1 provides the best efficiency, i.e. minimum power for given thrust output. This puts the motor operating point at a speed of rotation of approximately 3600rpm, producing 0.32Nm torque.

In practice, however, the thruster propeller that was available for use in this project had different characteristics when compared to that of the modified Ka4-70 propeller. The propeller that was available for use in this project was one that had been used in an integrated motor that had a slotted brushless permanent magnet motor for its drive. The characteristics of the propeller supplied were insufficient for making a similar comparison as described above for motor matching. However, it was known that the propeller pitch ratio is 1.4, with propeller thrust constant, K_T and torque constant, K_Q values of 0.49 and 0.14 at bollard pull respectively, compared with the Ka4-70 propeller values of 0.84 and 0.0906 respectively at the same propeller pitch ratio. The characteristics for this propeller are different from that of the Ka4-70, hence resulting in a different operating point and torque as well as machine configuration. It was known that the propeller had an operating point at

3600rpm rotational speed, producing 0.68Nm of torque, and as such the slotless motor in this project was optimised for that operating point, within dimensional constraints in order to provide a direct comparison with an existing thruster with a slotted motor.

Selection of Poles

In order to fit the motor within the duct, and to achieve good efficiency, it is essential to use a high number of poles to reduce the thickness of rotor and stator yokes and maximize the space available for the winding and magnets. A high number of poles will reduce the stator and rotor yoke thickness needed to carry flux hence enabling a thinner steel yoke to be designed.

However, there is a limit on the maximum number of poles determined primarily by the minimum thickness possible for rotor and stator yokes. A high pole number, i.e. a short pole pitch, also results in a higher proportion of leakage flux from one magnet to the next, thus reducing machine efficiency. In principle there is an optimum number of poles at which efficiency is maximum, but in practice in the machine under consideration the yoke thickness constraint is approached first, as discussed in Chapter 4. A high pole number also increases the electrical frequency, thus increasing core loss and inverter switching losses.

In a surface magnet machine and non-modulated pole machines in general, the high number of poles also reduces the Ampere conductors per pole, thus allowing a higher current to be drawn by the machine without demagnetising the magnets[3, 15]. It also reduces the winding inductance, thus improving the effective power factor of the machine which could possibly reduce the VA ratings of the drive inverter, although this has not been fully investigated.

Motor magnet thickness

The selection of magnet thickness is one that motor designers have to take into account when designing a permanent magnet motor. A thicker magnet thickness will allow more magnetic flux to pass through the motor airgap in order to interact with the armature reaction flux to produce motor rotation and torque. In the particular case for the slotless motor, this parameter is important, as the effective electromagnetic airgap of a slotless motor is larger than that of a typical slotted motor. The absence of teeth on the stator makes the surface of the stator further from the field sources (magnets).

As such, thicker magnets as well as additional copper need to be utilised in a slotless motor when compared to an equivalent slotted motor. There is an optimum split ratio between the amount of magnet material and copper material in the airgap that will yield maximum machine efficiency. Having more magnet material beyond the optimal point also increases flux losses and increases material costs.

Motor magnet width

The magnet maximum width is determined by the number of poles. The magnet width used, however, is normally selected to be less than the maximum width. This will provide a physical gap between magnets, allowing for mechanical tolerances. Also, the contribution of the material between magnets to the gap flux is small due to the majority of the flux from these regions moving from one magnet to the next as leakage flux. This amounts to an increased use of magnet material for small gains in motor performance; moreover the leakage flux needs to be carried by the rotor yoke hence increasing the rotor yoke thickness.

Winding Design

The three common configurations of windings are the 1) Lap Winding, 2) Wave Winding, and 3) Concentrated Winding. For low current machines (<250A), the lap winding and the wave winding can be used for the same ratings with no significant difference in performance[39]. The concentrated winding is different from these two types of windings in that the coils end-windings are shorter. The concentrated winding will have a lower winding resistance due to a shorter end-winding, however is more suited to motors with a fractional ratio of phase windings to magnet poles. Between the choice of a wave or a lap winding, the lap winding was found to be an easier method for winding the slotless motor design, in this project.

Chapter 3 Design Methodology

An analytical analysis and iteration of the motor design parameters is carried out. This involves the use of analytical equations to select the motor parameters that will be used for its design. The analytical process is carried out in order to reduce the amount of design time required to design the motor, by having a quick method of selecting the range of motor parameters compared to a purely finite element based design process. After this is done, finite element analysis is used in order to verify the results obtained analytically and to further optimise the design parameters based on design requirements. This is usually a time-consuming process, however, is able to produce solutions to the complex transient analysis of a motor. This will yield a predicted performance for the motor. Once this has been carried out, a prototype can then be built and tested in experimental validation, and the results from tests compared with the required specifications as well as computational results.

3.1 Literature on analytical methods

Analytical methods were used in the design process, as these methods are fast to use and require less computing resource to carry out. They are also accurate in describing the characteristics and performance of the variables that the designer is interested in[40, 41]. Analytical techniques also have an added advantage of allowing the designer a deeper understanding of the electric motor system. In order to have effective use of analytical equations for use in

the design process, an understanding of the derivation of these equations, alongside their limitations and assumptions, is required.

There are many different types of analytical methods that can be deployed for use in designing an electric motor. These range from an analysis of fields at boundaries through the method of images[42], to analysis utilising tensors[43], to specific instances of tensors through the Maxwell Stress Tensor method[44, 45], to the use back EMF formulation (Miller and Rabinovici's method)[46], and solutions using magnetic vector potentials[47, 48]. Each of these methods has their own specific advantages and disadvantages, which are shown in Table 5. The common goal, however, is to enable a rapid and accurate analysis of fields and characteristics of electric motors to aid designers.

Method	Advantage	Disadvantage
Method of Images	Simplicity in obtaining solutions to fields at boundaries	Restricted to straight-line boundaries. For curved boundaries, analysis tends to be awkward and difficult to apply
Tensors	Simplification in analysis of a complex linear system by transforming a problem into a more manageable form	Requires careful selection of reference axes. Transformation of magnetic fields is non-linear and results in difficult manipulation
Miller and Rabinovici's method	A quick method for sizing machines, through the solutions for back-emf in machines	Oversimplification of equations, leading to inaccurate solutions. These equations were designed to be coupled with Computer Aided Design (CAD) software, and additional knowledge of motor equations required to optimise motors
Solutions using magnetic vector potentials	Accurate prediction of field variables, accounting for both magnitude and direction of field	Solution equations are hefty for calculations and require computational aid in solving
Solutions using magnetic scalar potentials	Accurate prediction of field variables	Solution equations require computational aid in solving

Table 5:Advantages and disadvantages of various analytical methods

The analytical method employed in this research uses scalar magnetic potentials derived from the solutions of Laplace's and Poisson's equation (last method mentioned in Table 4). Solutions to Laplace's and Poisson's equations

are used in order to determine magnetic field due to the permanent magnets in the motor space for different motor physical parameters[49]. The solution of Laplace's and Poisson's equations is a fairly established mathematical technique, and the use of the magnetic scalar potential yields a relatively simple derivation of solution. The magnetic field determined through these equations is then used in equations that provide a rapid prediction of motor performance.

3.1.1 Brief background to analytical solutions of Laplace's and Poisson's Equations in motor design

Background to both analytical solutions yielding magnetic scalar potentials and vector potentials will be presented, as the development and use of both techniques share many similarities. Boules[50, 51] derived an analytical solution for the magnetic field due to permanent magnets in a machine by representing the magnets by current sheets. He derived solutions for both radial and parallel-magnetised magnets, and was one of the first solutions that had significant analytical depth. Hughes and Miller[52] derived analyses for slotless superconducting machines, through obtaining solutions in terms of Fourier series of sinusoidally distributed windings. These, however, were not immediately adaptable to permanent magnet machines. Zhu wrote a series of papers describing solutions to Laplace's and Poisson's equations, that provided an analytical method for obtaining the magnetic field in a motor airgap space due to its permanent magnets[52], the electromagnetic field in the

airgap due to current carrying coils[53], the effect of slotting on this field[54], and the field when the motor is under load[55]. These solutions form a rapid and easy method for obtaining field values within the motor space, which then lead to the calculation of other motor quantities such as torque and efficiency.

Atallah[56] developed vector potential solutions for slotless permanent magnet machines. These equations are for the armature reaction field, and does not take into account magnetisation of the permanent magnets. Rasmussen[57] extended the work done in this field by bringing together both scalar and vector potential solutions to the field equations, and making comparisons of the results compared to other existing analytical techniques as well as with finite element. Zhu then moved on to develop an improved model of these solutions, which take into account the use of parallel-magnetised permanent magnets[58]. His work has been widely used for other motor design work, such as [59, 60, 61, 62, 63, 64, 65, 66, 67]. Within this body of literature, solutions of the magnetic flux density are obtained and used to determine different aspects of motors, such as iron losses, torque ripple, or motor efficiency optimisation, some with alterations to the solutions in order to match the specific instances of the motors being designed.

3.2 The analytical design process

Figure 18 shows the analytical design process in more detail. In the figure:

ts = stator yoke thickness

tr = rotor yoke thickness

lm = magnet radial thickness

p = number of poles

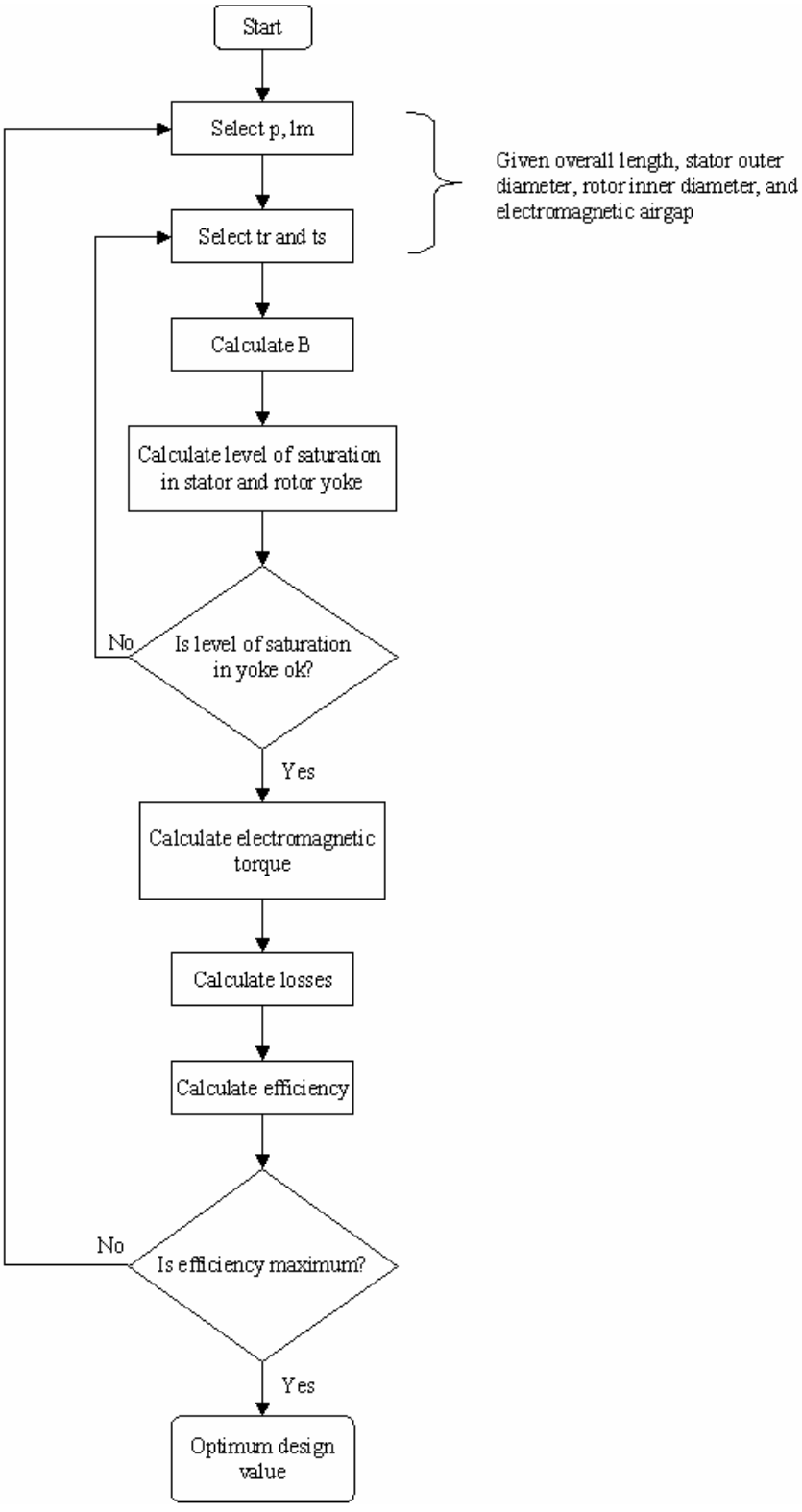

Figure 18: Analytical design process

At the beginning of this process, the number of poles, magnet thickness, rotor and stator yoke thickness are selected to fit within the constraints given. The magnetic field is then calculated for those values using the solutions for magnetic scalar potential. Flux saturation levels for the steel thickness selected can be calculated, and evaluated to determine if these levels are within the saturation limits of the stator and rotor yoke. If the steel is saturated, different values for steel thickness are then selected and this process repeated. When the level of saturation in the steel is evaluated to be within limits, the optimisation process then continues with electromagnetic torque, losses, and motor efficiency calculations. This process is repeated for different values of pole numbers and magnet thickness, and efficiency values compared. The design that yields maximum efficiency is then selected to be the optimum design.

3.3 Solutions to Laplace's Equation

Solutions to Laplace's equations have been developed, in order to obtain values of magnetic flux density within the motor space. These values can then be used to calculate magnetic flux values, saturation in core, and also used to predict motor performance characteristics such as efficiency. For permanent magnet motors, the field vectors $\vec{B}$ and $\vec{H}$ are coupled by:

$$\overrightarrow{B_I} = \mu_0 \overrightarrow{H_I} \qquad \text{in the air spaces} \qquad (1a)$$

$$\overrightarrow{B_{II}} = \mu_0 \mu_r \overrightarrow{H_{II}} + \mu_0 \overrightarrow{M} \qquad \text{in the permanent magnets} \qquad (1b)$$

For a multipole machine such as this slotless machine, using magnets with linear characteristics in the second quadrant, the magnetisation vector $\overrightarrow{M}$ is

$$M = \frac{B_r}{\mu_0} \tag{2}$$

The magnets chosen for use for this project are parallel-magnetised magnets, as they are cheaper and more available compared to radial-magnetised magnets. If the problem is expressed in polar coordinates, the magnetisation for parallel-magnetised magnets over one pole pair can be given by (Figure 19 and Figure 20):

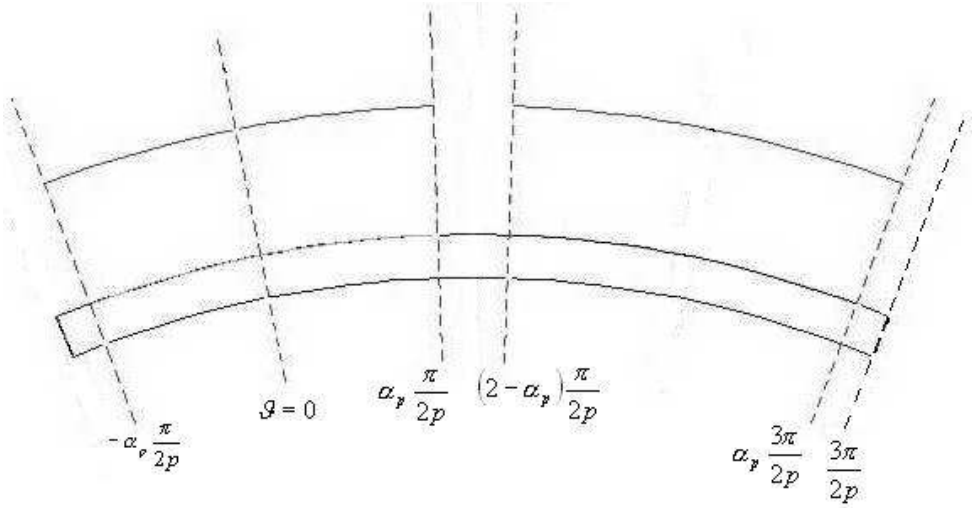

Figure 19: Magnet coordinates

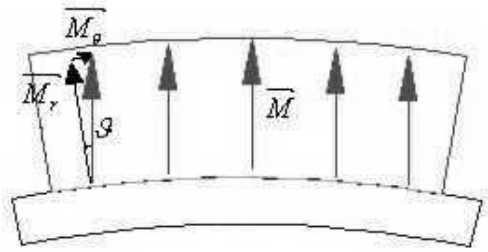

Figure 20: Magnetisation vectors for parallel-magnetised magnets

$$\left.\begin{aligned} M_r &= \frac{B_r}{\mu_0}\cos\vartheta \\ M_\vartheta &= -\frac{B_r}{\mu_0}\sin\vartheta \end{aligned}\right\} -\alpha_p\frac{\pi}{2p} \le \vartheta \le \alpha_p\frac{\pi}{2p} \tag{3a}$$

$$\left.\begin{aligned} M_r &= 0 \\ M_\vartheta &= 0 \end{aligned}\right\} \alpha_p\frac{\pi}{2p} \le \vartheta \le \left(2-\alpha_p\right)\frac{\pi}{2p} \tag{3b}$$

$$\left.\begin{aligned} M_r &= -\frac{B_r}{\mu_0}\cos\left(\vartheta-\frac{\pi}{p}\right) \\ M_\vartheta &= \frac{B_r}{\mu_0}\sin\left(\vartheta-\frac{\pi}{p}\right) \end{aligned}\right\} \left(2-\alpha_p\right)\frac{\pi}{2p} \le \vartheta \le \alpha_p\frac{3\pi}{2p} \tag{3c}$$

$$\left.\begin{aligned} M_r &= 0 \\ M_\vartheta &= 0 \end{aligned}\right\} \alpha_p\frac{3\pi}{2p} \le \vartheta \le \frac{3\pi}{2p} \tag{3d}$$

which can be expressed as a Fourier series by:

$$M_r = \sum_{n=1,3,5\ldots}^{\infty} M_{rn}\cos(np\vartheta) \tag{4a}$$

$$M_\vartheta = \sum_{n=1,3,5\ldots}^{\infty} M_{\vartheta n}\sin(np\vartheta) \tag{4b}$$

where, the magnetisation terms for parallel-magnetised magnets are given by:

$$M_{rn} = \frac{B_r}{\mu_0}\alpha_p (A_{1n} + A_{2n}) \tag{4c}$$

$$M_{\vartheta n} = \frac{B_r}{\mu_0}\alpha_p (A_{1n} - A_{2n}) \tag{4d}$$

where

$$A_{1n} = \frac{\sin\left[(np+1)\alpha_p \frac{\pi}{2p}\right]}{(np+1)\alpha_p \frac{\pi}{2p}} \tag{4e}$$

$$A_{2n} = \frac{\sin\left[(np-1)\alpha_p \frac{\pi}{2p}\right]}{(np-1)\alpha_p \frac{\pi}{2p}} \tag{4f}$$

μ_0 is the permeability of free space = $4\pi \times 10^{-7} H/m$.

μ_r is the relative permeability of the magnetic material.

B_r is the remanent flux density value of the magnetic material.

α_p is the ratio of the pole-arc width of a magnet pole over the width of the pole pitch.

The governing Laplacian equation, in cylindrical coordinates, is given by:

$$\frac{\partial^2 \phi_I}{\partial r^2} + \frac{1}{r}\frac{\partial \phi_I}{\partial r} + \frac{1}{r^2}\frac{\partial^2 \phi_I}{\partial \vartheta^2} = 0 \qquad \text{in the airgap} \qquad (5a)$$

$$\frac{\partial^2 \phi_{II}}{\partial r^2} + \frac{1}{r}\frac{\partial \phi_{II}}{\partial r} + \frac{1}{r^2}\frac{\partial^2 \phi_{II}}{\partial \vartheta^2} = \frac{1}{\mu_r} div\overrightarrow{M} \qquad \text{in the magnets} \qquad (5b)$$

The magnetisation source for equation (5b) is given by:

$$div\overrightarrow{M} = \frac{M_r}{r} + \frac{\partial M_r}{\partial r} + \frac{1}{r}\frac{\partial M_\vartheta}{\partial \vartheta} = \sum_{n=1,3,5\ldots}^{\infty} \frac{1}{r} M_n \cos(np\vartheta) \qquad (6a)$$

where:

$$M_n = M_{rn} + npM_{\vartheta n} \qquad (6b)$$

The boundary conditions used to solve these governing equations are defined by:

$$H_{\vartheta I}(R_s, \vartheta) = 0 \qquad \text{(orthogonality of the field at } R_s\text{)} \qquad (7a)$$

$$H_{\vartheta II}(R_r, \vartheta) = 0 \qquad \text{(orthogonality of the field at } R_r\text{)} \qquad (7b)$$

$$B_{rI}(R_m, \vartheta) = B_{rII}(R_m, \vartheta) \qquad \text{(continuity of the field at } R_m\text{)} \qquad (7c)$$

$$H_{\vartheta I}(R_m, \vartheta) = H_{\vartheta II}(R_m, \vartheta) \qquad \text{(continuity of the field at } R_m\text{)} \tag{7d}$$

Solving for these equations yields the solutions for magnetic flux density. In the motor airgap:

$$B_{rI}(r, \vartheta) = \sum_{n=1,3,5...}^{\infty} K_B(n) \cdot f_{Br}(r) \cdot \cos(np\vartheta) \tag{8a}$$

$$B_{\vartheta I}(r, \vartheta) = \sum_{n=1,3,5...}^{\infty} K_B(n) \cdot f_{B\vartheta}(r) \cdot \sin(np\vartheta) \tag{8b}$$

where :

B_{rI} is the radial component of B in the motor airgap.

$B_{\vartheta I}$ is the circumferential component of B in the motor airgap.

n is the harmonic component.

p is the number of pole pairs in the motor.

ϑ is the mechanical circumferential distance, in radians.

r is the radial distance where B is measured at.

For $np \neq 1$ with an internal rotor motor:

$$K_B(n)=\frac{\mu_0 M_n}{\mu_r}\frac{np}{(np)^2-1}\left\{\frac{(A_{3n}-1)+2\left(\frac{R_r}{R_m}\right)^{np+1}-(A_{3n}+1)\left(\frac{R_r}{R_m}\right)^{2np}}{\frac{\mu_r+1}{\mu_r}\left[1-\left(\frac{R_r}{R_s}\right)^{2np}\right]-\frac{\mu_r-1}{\mu_r}\left[\left(\frac{R_m}{R_s}\right)^{2np}-\left(\frac{R_r}{R_m}\right)^{2np}\right]}\right\} \quad (9)$$

$$f_{Br}(r)=\left(\frac{r}{R_s}\right)^{np-1}\left(\frac{R_m}{R_s}\right)^{np+1}+\left(\frac{R_m}{r}\right)^{np+1} \quad (10a)$$

$$f_{B\vartheta}(r)=-\left(\frac{r}{R_s}\right)^{np-1}\left(\frac{R_m}{R_s}\right)^{np+1}+\left(\frac{R_m}{r}\right)^{np+1} \quad (10b)$$

$$A_{3n}=\left(np-\frac{1}{np}\right)\frac{M_{rn}}{M_n}+\frac{1}{np} \quad (11)$$

In the magnets:

$$B_{rII}=\sum_{n=1,3,5\ldots}^{\infty}\mu_0 M_n\frac{np}{(np)^2-1}$$

$$\cdot\left\{\frac{\left(A_{3n}-\frac{1}{\mu_r}\right)\left(\frac{R_m}{R_s}\right)^{2np}+\left(1+\frac{1}{\mu_r}\right)\left(\frac{R_r}{R_m}\right)^{np+1}\left(\frac{R_m}{R_s}\right)^{2np}-\left(A_{3n}+\frac{1}{\mu_r}\right)-\left(1-\frac{1}{\mu_r}\right)\left(\frac{R_r}{R_m}\right)^{np+1}}{\frac{\mu_r+1}{\mu_r}\left[1-\left(\frac{R_r}{R_s}\right)^{2np}\right]-\frac{\mu_r-1}{\mu_r}\left[\left(\frac{R_m}{R_s}\right)^{2np}-\left(\frac{R_r}{R_m}\right)^{2np}\right]}\right\}$$

$$\cdot\left[\left(\frac{r}{R_m}\right)^{np-1}+\left(\frac{R_r}{R_m}\right)^{np-1}\left(\frac{R_r}{r}\right)^{np+1}\right]\cos(np\vartheta)+\sum_{n=1,3,5\ldots}^{\infty}\mu_0 M_n\frac{np}{(np)^2-1}\left(\frac{R_r}{r}\right)^{np+1}\cos(np\vartheta)$$

$$+\sum_{n=1,3,5\ldots}^{\infty}\mu_0 M_n \frac{npA_{3n}}{(np)^2-1}\cos(np\vartheta) \tag{12a}$$

$$B_{\vartheta II}=\sum_{n=1,3,5\ldots}^{\infty}-\mu_0 M_n \frac{np}{(np)^2-1}$$

$$\cdot\left\{\frac{\left(A_{3n}-\frac{1}{\mu_r}\right)\left(\frac{R_m}{R_s}\right)^{2np}+\left(1+\frac{1}{\mu_r}\right)\left(\frac{R_r}{R_m}\right)^{np+1}\left(\frac{R_m}{R_s}\right)^{2np}-\left(A_{3n}+\frac{1}{\mu_r}\right)-\left(1-\frac{1}{\mu_r}\right)\left(\frac{R_r}{R_m}\right)^{np+1}}{\frac{\mu_r+1}{\mu_r}\left[1-\left(\frac{R_r}{R_s}\right)^{2np}\right]-\frac{\mu_r-1}{\mu_r}\left[\left(\frac{R_m}{R_s}\right)^{2np}-\left(\frac{R_r}{R_m}\right)^{2np}\right]}\right\}$$

$$\cdot\left[\left(\frac{r}{R_m}\right)^{np-1}-\left(\frac{R_r}{R_m}\right)^{np-1}\left(\frac{R_r}{r}\right)^{np+1}\right]\sin(np\vartheta)+\sum_{n=1,3,5\ldots}^{\infty}\mu_0 M_n \frac{np}{(np)^2-1}\left(\frac{R_r}{r}\right)^{np+1}\sin(np\vartheta)$$

$$-\sum_{n=1,3,5\ldots}^{\infty}\mu_0 M_n \frac{A_{3n}}{(np)^2-1}\sin(np\vartheta) \tag{12b}$$

This equation provides a solution for evaluating the magnetic flux density due to the magnets' magnetic field for motor gap or magnets, for a range of motor design configurations.

These equations also do not account for axial flux fringing effects. The axial length of the motor is not considered here, and hence adjustments to flux values should be made to account for this.

3.4 Derivation of motor equations used in the analytical process

3.4.1 Steel saturation analysis

Steel saturation values are given by:

$$\phi_{steel\max} = \frac{1}{2}\int_{pole} B.ds = t_{steel} L_{motor} B_{sat} \qquad (13)$$

where:

$\phi_{steel\max}$ maximum magnetic flux in the steel

t_{steel} steel radial thickness

L_{motor} motor axial length

B_{sat} maximum magnetic flux density saturation value for the material

This assumes that the flux will be travelling in a perpendicular direction through the steel, and is not an unreasonable assumption due to the high permeability of steel.

Magnetic flux developed at steel surfaces are given by:

$$\phi_r = rL_{motor}\Delta\vartheta\sum_{pole} B \qquad (14)$$

where:

ϕ_r flux developed at radius r

r radius at which the flux is being evaluated at, Rs for the stator surface and Rr for the rotor surface

$\Delta\vartheta$ discrete circumferential position step through which magnetic flux density is being evaluated

$\sum_{pole} B$ sum of the magnetic flux values over a pole

The selection of $\Delta\vartheta$ should be small enough so as to allow for a smoother averaging of magnetic flux density values obtained. From steel saturation analysis, motor configurations with the smallest steel yoke thickness can be obtained.

Saturation here is evaluated using no-load flux values. Due to the large electromagnetic gap present in the motor, it was found through finite element analysis that the armature reaction flux is small and does not contribute a significant amount of flux and its effect on saturation is hence small. For initial design purposes, armature reaction flux is ignored.

3.4.2 Calculations of current and resistance

The current distribution in the coils is assumed to take on an ideal squarewave form. This squarewave spans across 120 electrical degrees.

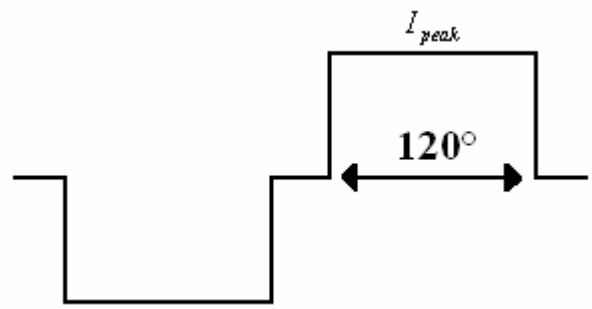

Figure 21: The ideal square-wave current

This spans across two conductors per pole pitch, and derivation of the torque equation (from which the peak current value can be calculated from) has to take this into account. The torque equation is derived as follows. Torque in the motor can be given by the following vector equation:

$$T = -2pL\int_{A} \vec{R} \times (\vec{J} \times \vec{B}) dA \qquad (15)$$

This describes the torque in a 2-dimensional motor model with axial length L, measured at a radius $\vec{R}$ with a current density $\vec{J}$ and a magnetic flux density $\vec{B}$ over an area A. The radius, and the magnetic flux density value, is taken at an average value across the coils. The equation then reduces to:

$$T = -2pLR_{coil}\int_{2/3\,pole} B(\int_r J \cdot dr)d\vartheta \tag{16}$$

where R_{coil} is the radius measured from the axis of the motor to the average radius of the coils. Assuming that the current density is uniform:

$$T = -2pLR_{coil}\int_{2/3\,pole} Bi_L R_{coil} d\vartheta \tag{17}$$

where $i_L = J \cdot \Delta r$

Discretising the equation for numerical analysis:

$$T = -2pLR_{coil}\sum_{2/3\,pole} B(i_L R_{coil}\Delta\vartheta) \tag{18}$$

Taking $\Delta\vartheta$ to be equal to a slot width; $i_L R_{coil}\Delta\vartheta$ can be represented by a term $I(\vartheta)$ that is a current value that varies with circumferential direction. This is a constant value since the current waveform is assumed to be a squarewave. The equation hence can be summarised as:

$$T = -2pLR_{coil}\sum_{2/3\,pole} B(\vartheta)I(\vartheta) = -2pLR_{coil}I_{peak}\sum_{2/3\,pole} B(\vartheta) \tag{19}$$

This is the torque equation per conductor. Multiplying the equation with $2N$ number of effective conductors per coil per pole, and rearranging Equation 19 for current yields Equation 20, which is used to calculate current in the coils for finding machine efficiency:

$$I_{peak} = \frac{T}{2p(2N)\sum_{2/3\,pole} B(\vartheta)LR_{coil}} \tag{20}$$

N is the number of turns per coil per pole

For coil resistance calculations, Figure 22 shows a diagram used for calculations of the length of coil.

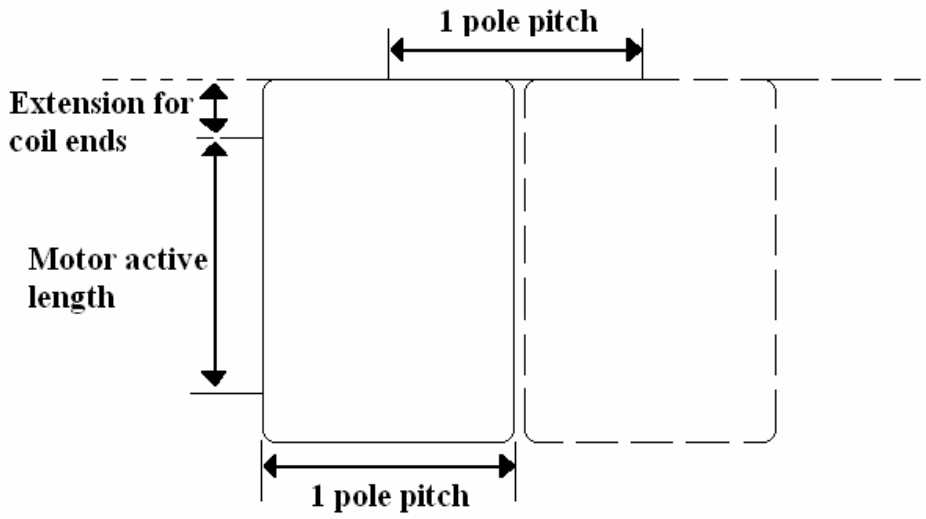

Figure 22: Diagram of motor winding for coil length calculations (broken lines depict subsequent connections)

The figure shows the winding over 1 pole. It is assumed that the winding spans across a pole pitch, with subsequent connections between coils also spanning a coil pitch. The length of the coil can thus be calculated with this equation:

$$l = 2p\left[N\left(2L_{motor} + 4l_{end} + 2\left(\frac{\pi}{p}R_{coil}\right)\right) + \left(\frac{\pi}{p}R_{coil}\right)\right] \quad (21)$$

l_{end} is the length of the extension at the ends of the coil

Calculating the copper cross sectional area is done by multiplying the available copper area per pole pitch by a fill factor (this is assumed), per coil per phase. Equation 13 shows how the cross sectional area is calculated:

$$A_c = \frac{1}{2}\left(R_s^2 - (R_m + g)^2\right)\left(\frac{\pi}{p} - 3\frac{l_{ft}}{R_{coil}}\right) \div N \div 6 \times ff$$

$$A_c = \frac{ff}{12N}\left(R_s^2 - (R_m + g)^2\right)\left(\frac{\pi}{p} - 3\frac{l_{ft}}{R_{coil}}\right) \quad (22)$$

g is the motor electromagnetic airgap

l_{ft} is the circumferential length of the former teeth on which the coils are wound

ff is the copper fill factor

In the equation, the area is divided by a factor of 6 because the windings considered are from 1 phase, and are assumed to be wound in a double-layer fashion. The resistance of the coils are then calculated from the resistance formula:

$$R = \rho_{copper} \frac{l}{A_c} \tag{23}$$

These values for current and resistance are then used in calculating the efficiency of the machine.

3.4.3 Calculations of efficiency

The motor electromagnetic efficiency is given by the following equation:

$$Efficiency, \eta = \frac{Power_{out}}{Power_{out} + Power_{totalloss}} = \frac{\omega T}{\omega T + P_{totalloss}} \tag{24}$$

where:

ω	is the rated speed, in rad/s
T	is the rated torque, in Nm
$P_{totalloss}$	is the total power loss in the motor

The electromagnetic power loss in the motor consists of copper losses and steel core loss:

$$P_{totalloss} = 3P_{copper} + P_{coreloss} = 3(I_{rms}^2 R) + P_{coreloss} \quad (25)$$

Since it is assumed that the current distribution in the coils is a squarewave current, the peak value of the current can be used to calculate copper losses:

$$P_{copper} = 3I_{rms}^2 R \quad \text{(for three windings)}$$

$$= 3\left(\sqrt{\frac{2}{3}} I_{peak}\right)^2 R$$

$$P_{copper} = 2I_{peak}^2 R \quad (26)$$

Core loss can be divided into a further three components, that are the steel hysteresis loss, eddy current losses, as well as an excess loss that is a component of eddy current loss that arises from induced eddy current concentration around moving domain walls of a magnetic domain structure[68]:

$$P_{core} = (P_{hyst} + P_{eddy} + P_{exc})m \quad (27)$$

where m is the mass of the steel core

Hysteresis losses are given by:

$$P_{hyst}(W/kg) = K_h f B^2 \tag{28}$$

Eddy current losses are given by the Steinmetz's equation:

$$P_{eddy}(W/kg) = K_c f^2 B^2 \tag{29}$$

Excess losses are given here for completeness, but are not calculated during the analysis, by the equation:

$$P_{exc}(W/kg) = \frac{K_e}{T}\int_T (B(t))^{1.5}\,dt \tag{30}$$

where

$$K_c = \frac{\pi^2 \tau^2}{6\rho_{resistivty}\rho_{steel}} \tag{31}$$

f	is the electrical frequency of rotation
T	is $1/f$
τ	is the thickness of the steel laminations
$\rho_{resistivity}$	is the electrical resistivity of the steel material
ρ_{steel}	is the density of the steel material

m is the mass of the steel core

K_h is an experimentally derived figure (or can also be calculated if the hysteresis curve of the steel material is known). The value for K_h was calculated by using known core loss values for electrical steel material that had high permeability, as there were no available data for the mild steel material used. K_e is also an experimentally derived figure, that is obtained from single-sheet tests (normally provided by manufacturers). In this instance, however, K_e values were unknown and as such excess losses were undetermined. However, it was found through testing of the demonstrator unit that core losses are small in this design, and as such excess losses could be ignored for the purposes of initial design optimisation leading to finite element analysis.

3.4.4 Calculations of winding voltage

After the motor steel and magnet parameters have been selected, the next step is to select the number of coils in the motor. This predominantly affects the winding voltage drawn into the motor, with little effect to the motor's efficiency. The general rule of thumb is that as the number of coils increases, the voltage required to drive the motor for the same torque increases, conversely the current decreases. This is mainly matched with the controller that is used to drive the motor. A prediction of the winding voltage required to drive the machine is necessary in order to have the appropriate number of

winding turns in the machine, and to have a motor controller that is rated appropriately without needing added expenses for a large controller.

The winding voltage is calculated based on the calculated peak current in the windings as well as a calculated back-emf. The line-to-line voltage is used as this effectively reduces any shifts to a motor's neutral point and allows for a more accurate sizing:

$$V_{line-to-line} = 2(I_{peak}R + K\omega) \tag{32}$$

K is the machine constant, which can be obtained by calculating the gradient of a torque-current graph:

$$K = T / I_{peak} \tag{33}$$

Care has to be taken when using these equations, as they are based on the assumption that torque, speed and current values in the motor are constant. These are rough calculations for moving into finite element analysis modelling, where a transient circuit analysis model will be able to take into account the effect of winding inductance.

3.4.5 Motor axial length selection

The final step in this analytical design is to select the motor axial length that fits within the overall length of the design. Increasing motor length will increase motor efficiency, because torque production is increased with a lower required current loading, however there is an increase in rotor inertia and magnet material costs. The best increase in efficiency has to be selected for an increase in motor length.

3.5 Computational verification phase

Following the analytical design, finite element analysis is then used to refine the design and for selection of the number of turns, saturation checking and production of transient waveforms of voltage and current. To do this, a 2-dimensional transient analysis was used.

3.5.1 Methodology for 2 - Dimensional Finite Element Analysis

The finite element package used to model the motor is a 2-dimensional transient package from Ansoft Corporation. The transient model simulates a time-varying motor model by combining magnetostatic solutions with time-varying circuit analysis over a user-specified time. Modelling the motor in the finite element package involves various steps. The first step is to create the actual model to be analysed. Here, a model with 1 pole pair was selected for modelling the motor. This was chosen because the solutions yielded are symmetrical beyond that, and hence it is not required to create a larger model.

This also minimises the computing resources consumed in running this FE analysis. Figure 23 illustrates a typical Finite Element Model created for analysis.

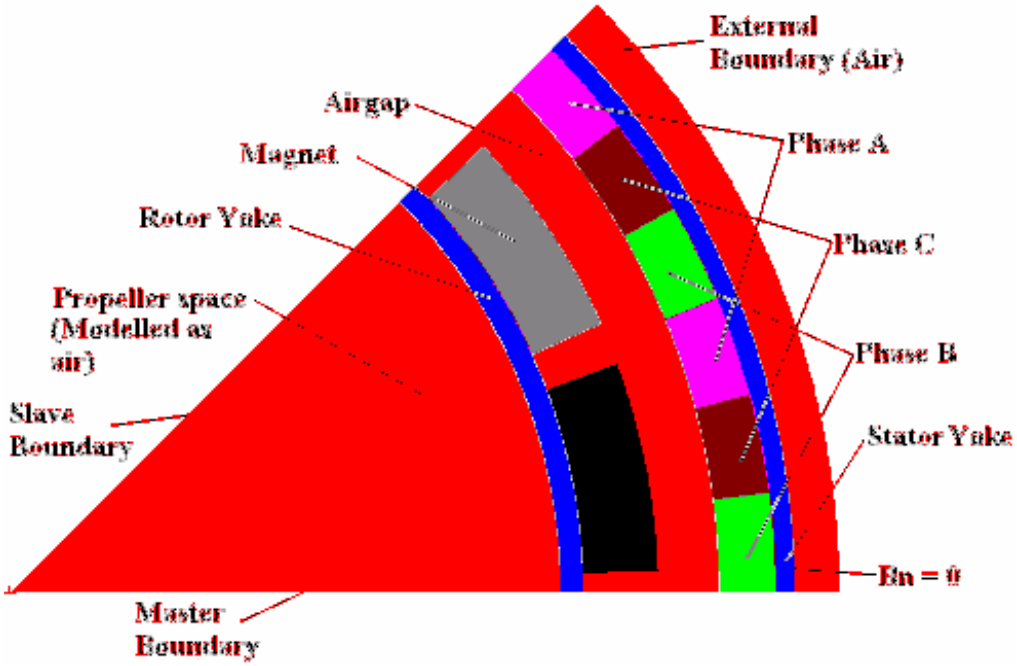

Figure 23: A 2 dimensional Finite Element Model

The next step in creating this FE model is to specify the materials used in the motor. For the coils, copper material is used. For the stator and rotor, steel is used. The conductivity of the steel used in the stator is set to zero, as the stator is laminated. For the magnets, a magnetic material with properties similar to those of Samarium Cobalt was predefined for use. Table 6 summarises the properties of the magnet modelled in finite element.

Property	Value
Magnet grade	Samarium Cobalt, Sm_2Co_{17}
Remanence flux density, B_r	1.010T
Magnetic field coercivity, H_c	733.3kA/m
Recoil permeability, μ_r	1.096

Table 6: Properties of magnet material modelled in finite element analysis

The motor has a non-magnetic inner diameter, as the propeller and shaft are non-magnetic. As such, air was used to represent the space through the rotor, as was used to represent the gap between the rotor and the stator and the surrounding area beyond the stator.

Boundary conditions for the model are then specified. A master-slave boundary was selected for the edges of the model bordering the periodic portion of the model. The slave boundary was assigned a positive symmetry, as the field for the model at that boundary has the same direction as that at the master boundary. For the outer edge of the model, a Dirichlet boundary condition was selected, where the normal component of flux was specified to be zero, in order to limit the flux distribution within the boundaries of the model. For all other boundaries of the motor, a natural (or Neumann) boundary condition was selected (this is the default boundary condition selected for all boundaries which are not otherwise defined).

The coils were connected to an external circuit. This is a useful aspect of the transient finite element package used, which allows an external electric circuit to be coupled with the model. In our model, the coils are represented in an inverter circuit as shown in Figure 24.

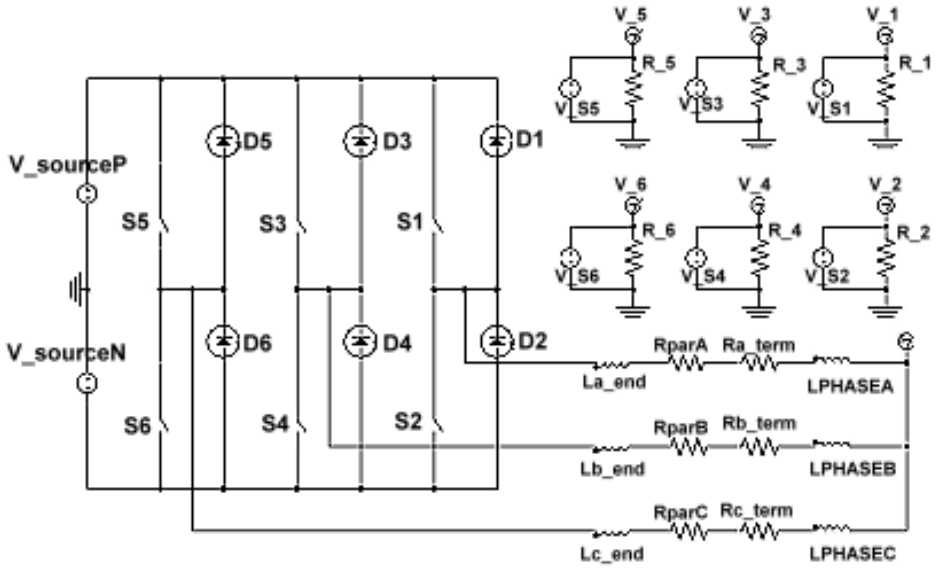

Figure 24: Inverter circuit coupled with the FE model

The three phases are represented in the circuit as coils (LPHASEA, LPHASEB, LPHASEC). This motor is a star-wound motor. Each individual phase's terminal resistance and end inductance are also represented on the three branches as Rx_term, and Lx_end (where x represents the corresponding phase). There is an additional resistive term, Rparx, which is included in the circuit to represent the parasitic effects due to internal transistor resistances, cables and connectors in a real model. This resistance is significant. This value

of resistance was found experimentally by measuring the resistance of the experimental setup from the inverter to motor. Six switches with free-wheeling diodes are connected to the three phases, with the switches taking the place of transistor switches as in a standard three phase inverter. These switches have an almost negligible switching on resistance (0.001Ω). These switches are controlled by voltage pulses, which are provided by six independent power supplies (V_Sx) which pulse based on the switching pattern required. This provides a simple way for controlling the switching pattern in the inverter. The switching pattern required is determined by first running the model as a generator, and calculating the back EMF waveforms for each phase. From these back EMF waveforms, the order of switching can then be determined by examining the order of back EMF generation in the three phases. Figure 25 shows the switch-timing diagram for the slotless motor.

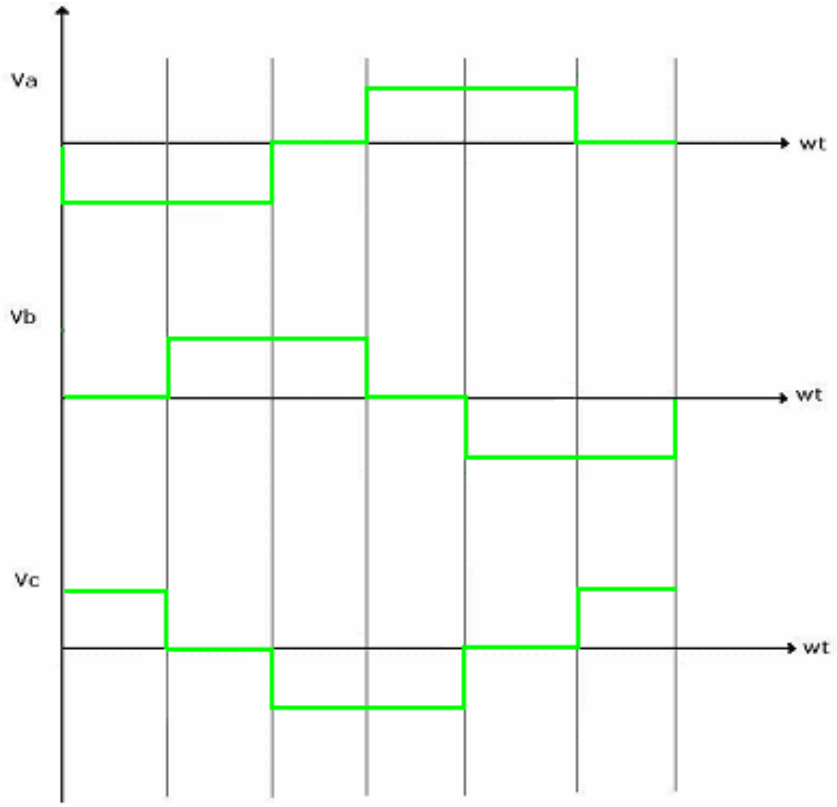

Figure 25: Switch-timing diagram

After the boundary conditions have been specified, the finite element meshing for the model needs to be created. The mesh was given a higher density around regions of the model that were known to have eddy current effects, as well as at points of higher flux density. Particularly in regions such as the magnets, the seeding of the mesh was done such that a minimum of three nodes resides within the skin depth of these areas. It was found that the skin depth of the magnets was approximately 2.69mm, calculated using Equation 34.

$$S = \sqrt{\frac{2}{2\pi f_{harmonic} \sigma_{steel} \mu_{rsteel} \mu_0}} \tag{34}$$

where $f_{harmonic}$ is the frequency of the 10^{th} harmonic

μ_{rsteel} is the relative permeability of the steel material modelled

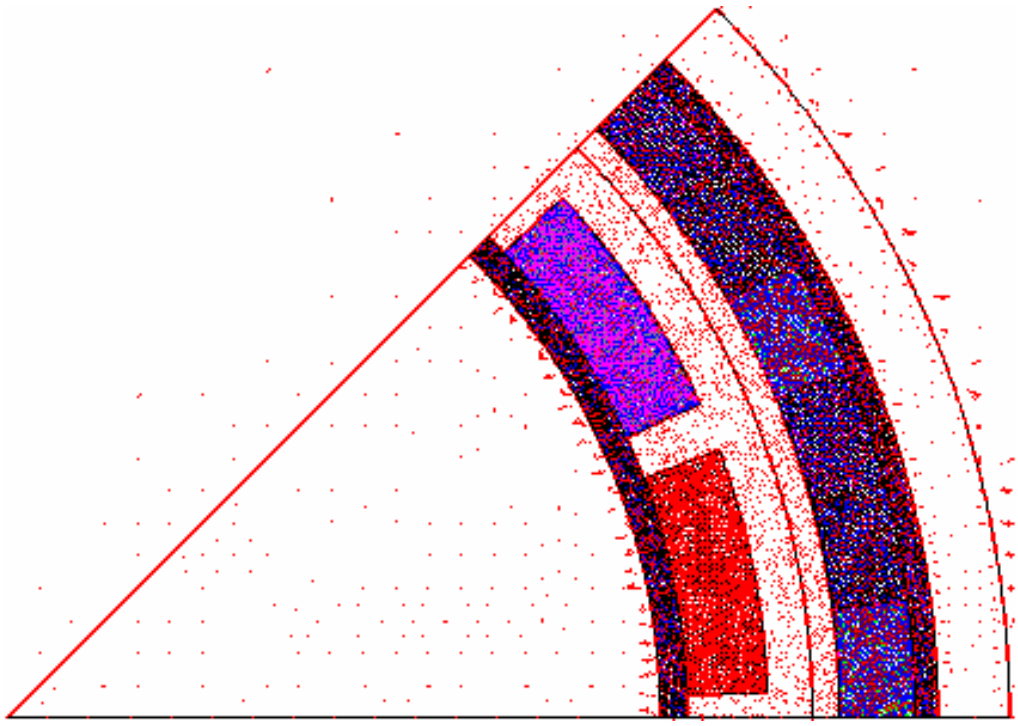

Figure 26: The mesh generated for the 2-dimensional slotless motor model

Once the mesh is created and refine, the solution process is then set up. The stop time and the time step are specified for this transient analysis. The stop time selected is the time required for the motor to rotate through 180 mechanical degrees, as this was sufficient for the model to reach steady state and yield enough transient waveforms for analysis. A longer stop time would

require additional computational time. The time step selected such that there are 20 points of analysis for the time it takes to step through one slot of the motor. The equation used to calculate this is shown (Equation 35):

$$Timestep = \frac{1}{\frac{speed(rpm)}{60}} \div NumberofPoles \div NumberofPhases \div 20$$

$$Timestep = \frac{3}{speed(rpm)} \times \frac{1}{NumberofPoles} \times \frac{1}{NumberofPhases} \quad (35)$$

The model depth is then specified in this solution process, and the symmetry multiplier provided (this is to tell the software what division this model is of the entire actual model required). The maximum residual allowed in the analysis for convergence was a 0.001, this was determined to be sufficiently small enough to obtain an accurate result, without once again taking too long in the analysis time to converge. The residual is the measure of how close the field solution gets to solving the electromagnetic field equation which is being solved, that is, Maxwell's equations. The final step before running the analysis is to specify motion within the model. This is done by first specifying an object in the model that acts as the 'band', within which all the objects are moving, either in a translational or rotational way. For motor analysis, the motion is obviously rotational, with the magnets and rotor lying within this band object. The speed of this rotation is also selected here.

Chapter 4 Design optimisation

In this chapter, the design optimisation results as well as the selection of the slotless motor parameters will be discussed.

4.1 Analytical design of the slotless motor

The range of parameters analysed for use with the design of this slotless motor are selected based on the parameters fitting within the constraints of the motor design as well as prior experience from other integrated thruster designs. These values are summarised in a table in Table 6.

Parameter	Minimum value	Maximum value	Step size
Number of Pole Pairs	7	12	1
Stator thickness	1.25mm	2mm	0.25mm
Rotor thickness	1.25mm	2mm	0.25mm
Magnet thickness	3mm	6mm	1mm
Circumferential position	0 elec deg	120 elec deg	6 elec deg
Parameter	Value		
Pole-arc to Pole-pitch ratio	1		
Number of harmonics	399		

Table 7: Iteration values for motor parameters

Efficiency calculations were made with the assumption that the windings would be a double-layered winding that are wound on a non-conducting former. This former would then sit within the available space for coils. Due to the presence of 'teeth' on the former on which the coils are wound on, there is less available space for the winding copper. The fill factor used in these

calculations assumed a 25% copper fill factor within the coil-space. Figure 27 shows the results of efficiency calculations for different possible motor pole numbers and magnet thickness that were determined from steel saturation analysis:

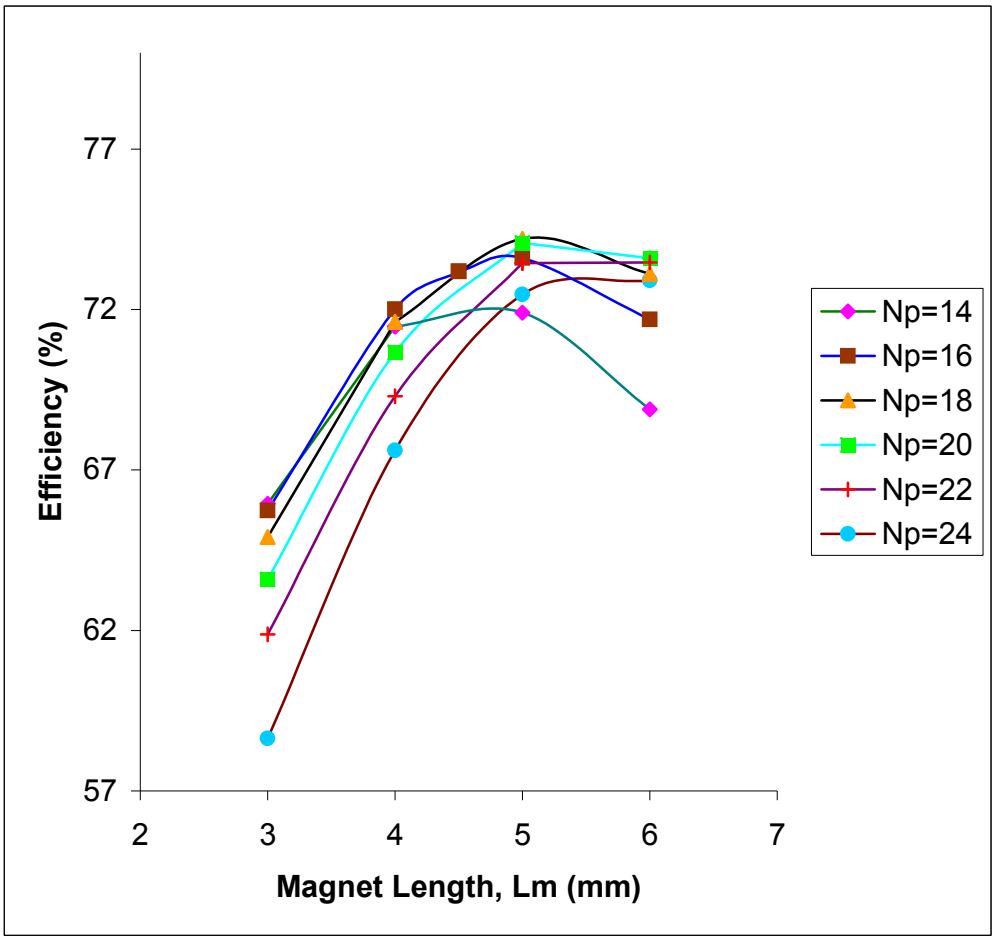

Figure 27: Graph of motor efficiency versus magnet length for different number of pole-pairs

Figure 27 shows the graph of motor efficiency versus magnet length for the different configurations identified in the table above. From the graph above, it can be seen that the best configuration would be to have a 16-pole machine at 4.5mm magnet thickness, an 18-pole machine at 5mm magnet thickness, or a 20 pole machine at 5mm magnet thickness. A 16 pole machine was selected for this project, due to the required tooling for producing 16 magnet poles of this size existing, hence saving tooling costs.

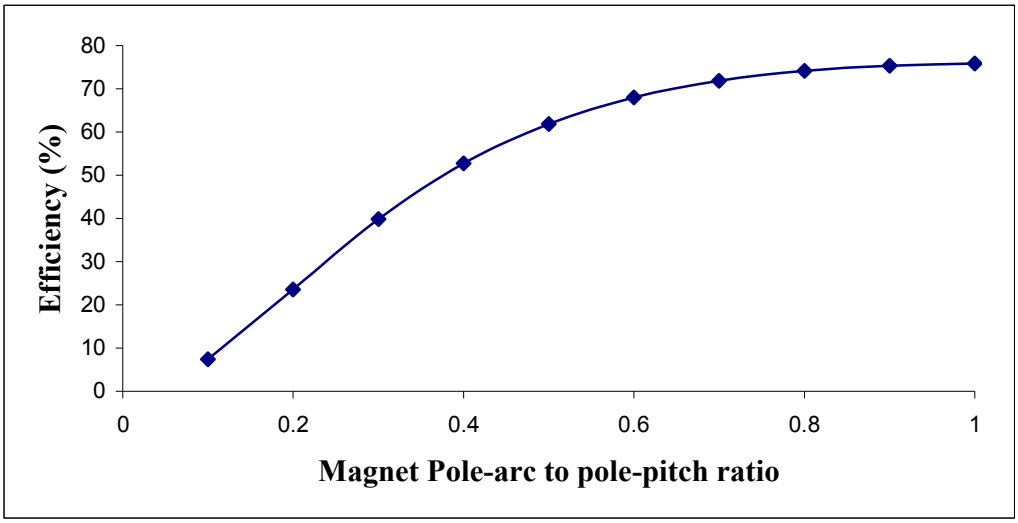

Figure 28: Graph of efficiency versus magnet pole-arc to pole-width ratio

Figure 28 shows a graph of efficiency versus magnet pole-arc to pole-pitch ratio. It can be seen that the efficiency of the motor increases with increasing magnet pole-arc ratio. As discussed in Chapter 2, the magnet pole width is chosen to be slightly less than the maximum available width for the purposes

of allowing for mechanical tolerance between magnet poles. It can also be seen from the graph that gains in efficiency are less at higher magnet widths, due to an increased proportion of flux fringing occurring from one pole to the next. A magnet pole-arc to pole-pitch ratio of 0.833 was chosen as the point that yields the best gains in efficiency for the added magnet material required.

With these various results, the motor physical dimensions are almost complete. The number of turns on the motor coils remains to be selected. The inverter that will be used to drive the motor supplies 30V D.C. link to the machine, and from calculations it has been found that the 3 turns per pole is required.

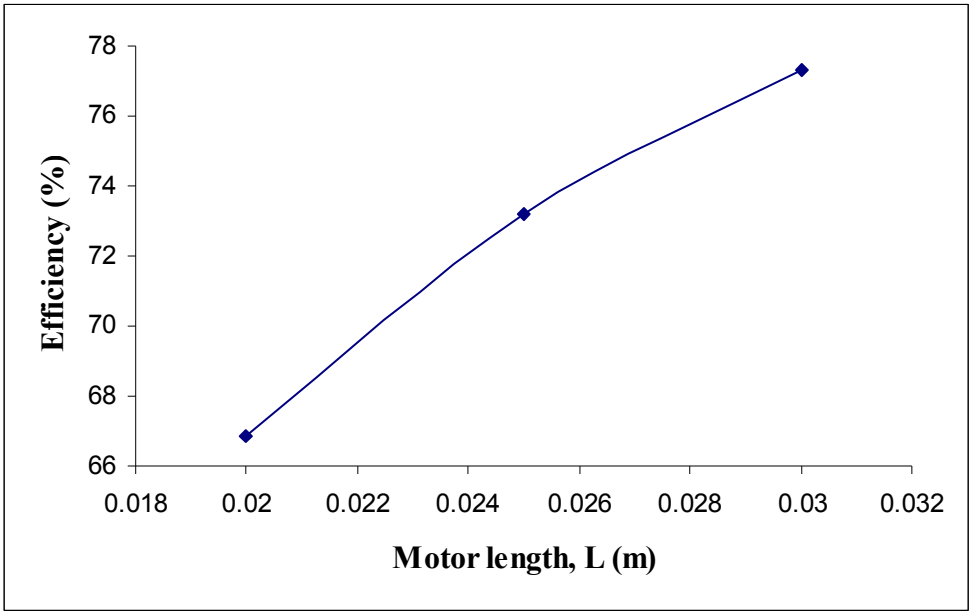

Figure 29: Efficiency versus motor axial length

The final stage of this design is the selection of the motor axial length. From Figure 29, it can be seen that the motor efficiency increases with an increase of motor axial length. The lengths selected for iteration are a 20mm, 25mm, and 30mm motor axial length. These are the available lengths that are able to fit within the constraints of overall length. From the efficiency curve, it can be seen that a longer motor would result in a higher efficiency, which is desirable. However, the increase in efficiency at a motor length of 30mm does not justify the gain in rotor inertia as well as the additional magnet material required to make up that motor length, and as such it was determined that a motor length of 25mm provided the best increase of efficiency for an additional volume of magnet material. As such, the final motor dimensions and performance prediction are summarised in Table 8:

Motor parameter	Value
Stator steel thickness	1.25mm
Rotor steel thickness	1.5mm
Number of poles	16
Magnet thickness	4.5mm
Magnet pole-arc to pole-width ratio	0.833
Number of phases	3
Number of turns per pole	3
Motor active axial length	25mm
External motor diameter	104mm
Internal motor diameter	73mm
Electromagnetic airgap	4mm
Nominal torque	0.68Nm
Nominal speed	3600rpm
Calculated motor efficiency	73.19%

Table 8: Motor final dimensions and performance prediction

4.2 Computational Analysis of Slotless Motor

From the analytical design stage, a motor configuration has been selected. This configuration has been modelled in FEA, and the results from this computation will be shown and discussed. A comparison between the predicted performance calculated from analytical methods and FEA will also be made, in order to examine further any specific optimisation that needs to be done to the design.

4.2.1 Computational Results

The results of computational work are presented in this section. Figure 30 shows a flux plot obtained from finite element analysis:

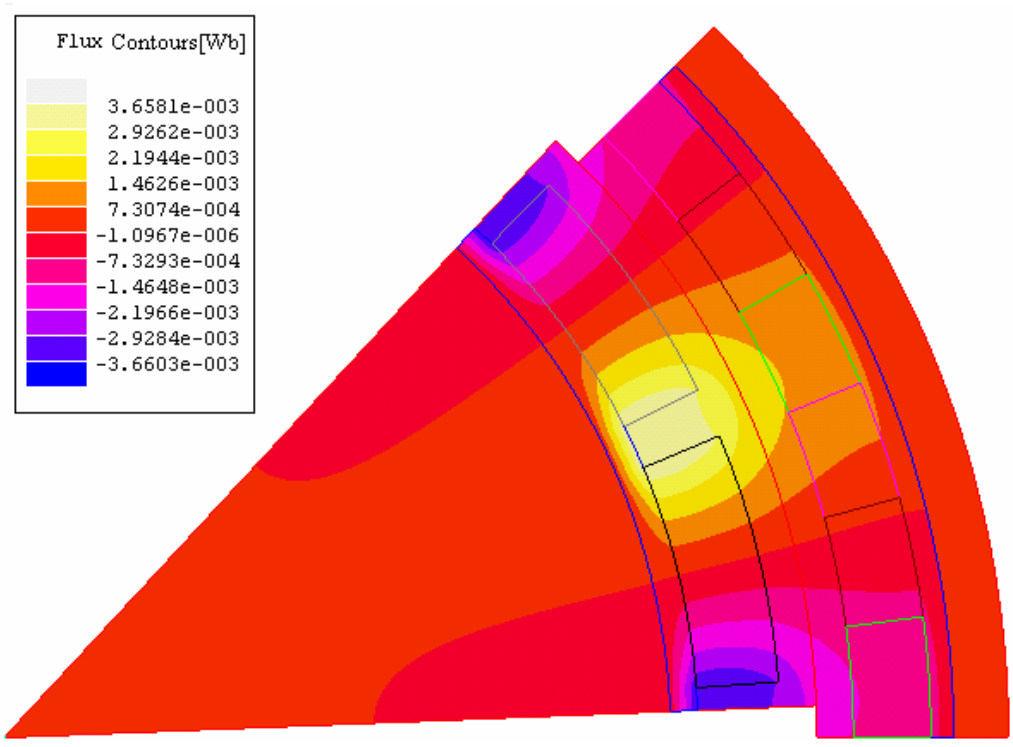

Figure 30: Flux plot in the 2D FEA model

From this plot, it can be seen that the flux is greatest in the magnets and the area surrounding them. The flux areas are at the corners of the magnets, and in the vicinity of the rotor steel where these magnet corners lie. There is saturation in the steel in these areas, and the choice is for the steel thickness to be increased in order to avoid this saturation, or for this effect to be ignored. It was chosen to ignore the saturation at the magnet edges, as they do not affect motor performance substantially; these predominantly belong to magnet flux leakage. It can be seen from this plot that the stator steel and the main sections of the rotor steel that provide the path for the useful flux remain below the steel flux saturation limit, which was calculated to be at 4.69×10^{-5}Wb. The flux levels in the steel are at the limits of saturation, however, and as such the design has reached its minimum thickness, as it is likely that the steel will saturate if the thickness was made smaller.

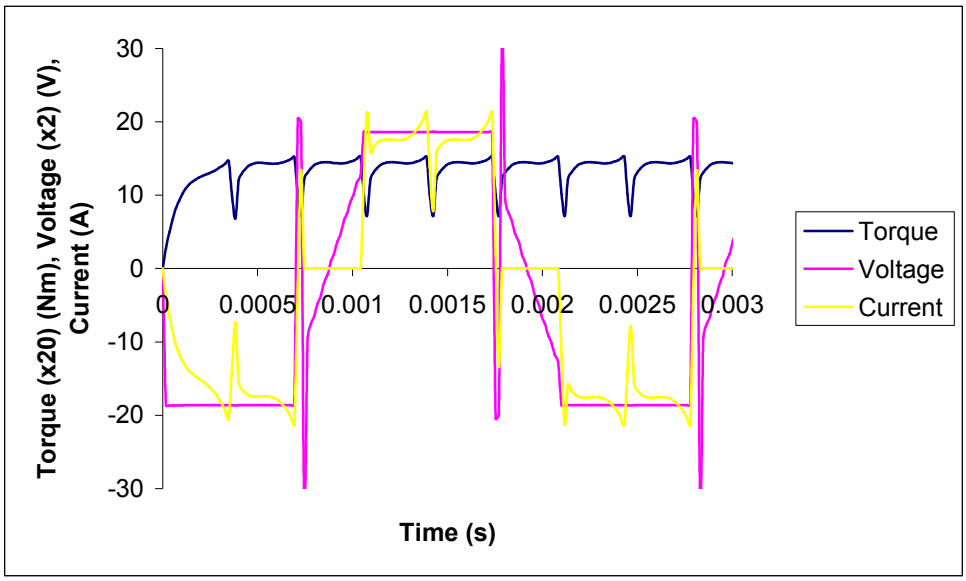

Figure 31: Graph of predicted torque, winding voltage and current versus time from 2D FEA computation

Figure 31 shows a plot of predicted torque, winding voltage and current versus time, as derived from FEA computation. The torque and voltage values have been scaled up to match scales used for winding current, for clarity. It is observed that there is a ripple in the torque produced by the motor. However, it can also be observed that this ripple occurs in high frequency, over small periods of time. This ripple corresponds to when switching occurs in the inverter drive, as can be seen by the current waveform. It is predicted from these results that in the motor's actual operation, these ripples will not be significantly noticed and the motor's operation will be essentially smooth. The torque developed by the motor is the average value of the torque ripples.

For the curve showing computed winding voltage, in one phase, of the motor, this is typical of the phase voltage due to the switching in the inverter. It can be seen that the voltage holds at a constant level for a period of time. This is when the phase is energised, and corresponds to when the corresponding transistor is 'on'. When the transistor is switched off, the voltage drops to the negative, and this occurs due to the free-wheeling diode dissipating the voltage in the circuit, when the switch switches 'off'. The voltage then reduces gradually, and this corresponds to the back-EMF of the motor. When the second transistor switched on, the voltage then rises to a constant value in the opposite polarity, hence repeating the cycle.

Winding current in one phase of the windings in the motor can be seen to rises at a certain rate to a peak value, due to the time constant of the winding. It then dips down momentarily, before returning to its peak value. This is due to the switching of transistors for another phase, in the inverter. At the end of the switching cycle, when the transistor is switched off, the current decreases at a gradual rate rather than an instantaneous decrease. This is due to the current being dissipated in a free-wheeling diode, in order to prevent a large voltage developing due to inductance if the current is switched off instantaneously. The decrease in the current at the end of the switching cycle is not an instantaneous decrease, and this is due to the current in the free-wheeling

diode. The current is zero for the duration of time when the switches are 'off', and only the back-EMF is present in the windings.

4.2.2 Comparison of results from finite element analysis with analytical results

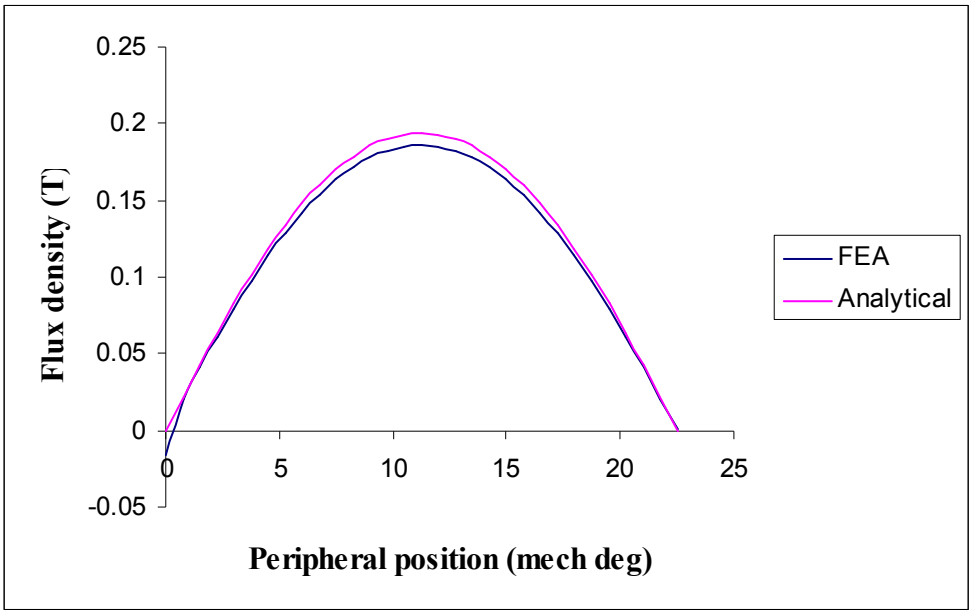

Figure 32: Comparison of flux density in the motor airgap evaluated over the stator bore for analytical and FEA results

From the results shown above, the motor's characteristics can be predicted. Comparisons between finite element analysis and analytical calculation results will be shown in this section in order to further validate the design chosen by evaluating the accuracy of the analytical calculations employed. Figure 32 shows a comparison for the flux density in the motor airgap evaluated over the stator bore between analytical and finite element results. It can be seen that

there is a close agreement between the flux density values obtained. The peak of the analytical flux density curve is slightly higher (approximately 0.008T) when compared to that obtained from FEA. This is because the armature reaction flux is not taken into account in the analytical calculations. However, due to the small differences in the flux density results obtained, it is an indication that the armature reaction flux effects are very small, enhancing confidence in the use of open circuit flux density equations in the analytical calculations.

Table 8 summarises the values obtained from analytical calculations and finite element analysis.

	Analytical	Finite element analysis
Efficiency	73.19%	71.44%
Peak current	21.92A	21.29A
Core loss	8.16W	7.05W
Torque	0.68Nm	0.684Nm

Table 9: Comparison of analytical and finite element analysis values

From Table 9, it can be seen that the values obtained analytically and through finite element analysis agree closely. There is a difference of 1.75% predicted efficiency values between the analytical and finite element analysis results,

which can be attributed due to the differences in estimation of peak current and core loss, as well as the flux density differences arising from armature reaction flux taken into account in FEA.

The peak current calculated in the analytical calculations is approximately 0.7A more than that from finite element, for the same torque. This difference most likely arises from the squarewave current waveform modelled in the analytical calculations, compared to the transient waveform produced in FEA. The difference is small, however, verifying the validity of the squarewave current model. There is a difference between the core loss values calculated through analytical calculations and those obtained from finite element as well, a difference of approximately 1.1W. Once again, this difference can be attributed to the difference in flux density values calculated in the analytical calculations compared to finite element. As these values influence both hysteresis and eddy current core losses, a slight variation in the flux density value calculated would results in a difference in core loss calculations.

As a result of finite element analysis, validation of the motor design and the expected performance has been carried out. The next stage of this design process is prototyping and testing of the slotless motor, and this will be described in Chapter 5.

Chapter 5 Prototyping and Testing the Slotless Motor

In this chapter, the prototyping process for the slotless motor will be presented. In particular, specific issues to do with the manufacture of the prototype will be addressed, and the techniques used described. A quantitative analysis of the costs for manufacturing the slotless motor has not been carried out, however a qualitative analysis reveals that the method used is a potentially cheaper method of manufacture compared to conventional methods.

One of the largest areas of cost in current manufacture of motors is in the production of stator laminations. This is due to two factors: 1) The motor stator laminations are expensive to make due to the high costs for labour and manufacturing. The typical process involves either laser cutting or stamping lamination shapes out of metal sheets, and manually stacking and gluing these laminations into a stack. In order to reduce the overall costs of producing a motor for the integrated thruster unit, methods need to be found to reduce these labour and manufacturing costs. 2) There is some material waste generated when producing steel laminations from metal sheets. It is advantageous to seek a method of manufacture that will allow less material waste to be generated, hence improving the efficiency of material use and reduce overall costs of production of a motor unit.

With the slotless stator, material waste can be reduced due to a less complicated stator lamination shape (without the teeth). In addition to that, the stator is a novel design, in which, the stator will be made up by forming a rectangular-sectioned strip of steel in a helical pattern. This would potentially reduce the amount of labour involved in having to stack and glue individual sheets of lamination together.

5.1 Prototyping Issues

There were a number of specific issues related to the prototyping of this slotless motor design:

1) *How the windings were to be wound on the slotless stator* - as there is an absence of teeth for the windings to be wound on, a method needed to be found in order to wind the motor windings and locate them on the surface of the slotless stator.

2) *How the helical stator would be made* - the helical method of constructing the stator is intended to replace the conventional method of stacking laminations. As such, the thickness of each coil of the helical stator is required to be thin, in order to provide a similar performance to a conventional lamination. However, due to the radial thickness of this helical form being thicker than the axial thickness (approximately 2.25 times thicker), there are difficulties in forming a helical structure such as this. Ideally such a helical

stator is formed as the steel is turned out in its molten state. However, this requires specifically designed equipment to achieve, and many steel manufacturers in the UK are not able to produce such rectangular-sectioned steels. The closest cheaper alternative that could be found was to obtain strips of steel that were wound with the wider face of the steel lain flat when the steel is turned out. This, however, provides difficulties in re-winding the steel into the right shape due to high stresses in the formed steel. An edge winding technique had to be developed in order to accomplish this.

5.1.1 Winding the coils on the stator

After exploring a number of different alternatives, it was decided that the windings would be wound on a small light former that had teeth in order to guide the winding of the coils. Figure 33 shows a picture of this former.

Figure 33: Picture of the former for winding coils

The purpose of this former is for supporting the coils as they are wound around the circumference of the stator, and is made of a non-electrically and magnetically conducting material. A nylon material, Delrin, was selected for this purpose. Table 9 shows the main material properties for Delrin.

Physical Property	**Value**
Density	$1.42 g/cc$
Water absorption	0.31%
Mechanical Property	**Value**
Yield tensile strength	$69 MPa$
Modulus of Elasticity	$3.3 GPa$
Electrical Property	**Value**
Electrical resistivity	$1\times10^{15}\,\Omega/cm$
Surface resistance	$5\times10^{15}\,\Omega$
Dielectric constant	3.6
Dielectric strength	$16.5\ kV/mm$
Dissipation factor	0.005
Thermal property	**Value**
Melting point	$178°C$
Deflection temperature at 0.46MPa (66psi)	$165°C$
Deflection temperature at 1.8MPa (264psi)	$112°C$
Flammability, UL94	HB

Table 10: Material properties for Delrin[73]

The diameter of this assembly fits within the diameter of the stator, where the stator sits over the teeth that the coils are wrapped around. The former also provides additional protection to the coils. The ends of the former will be enclosed by end-caps. Figure 34 shows a picture of the wound former.

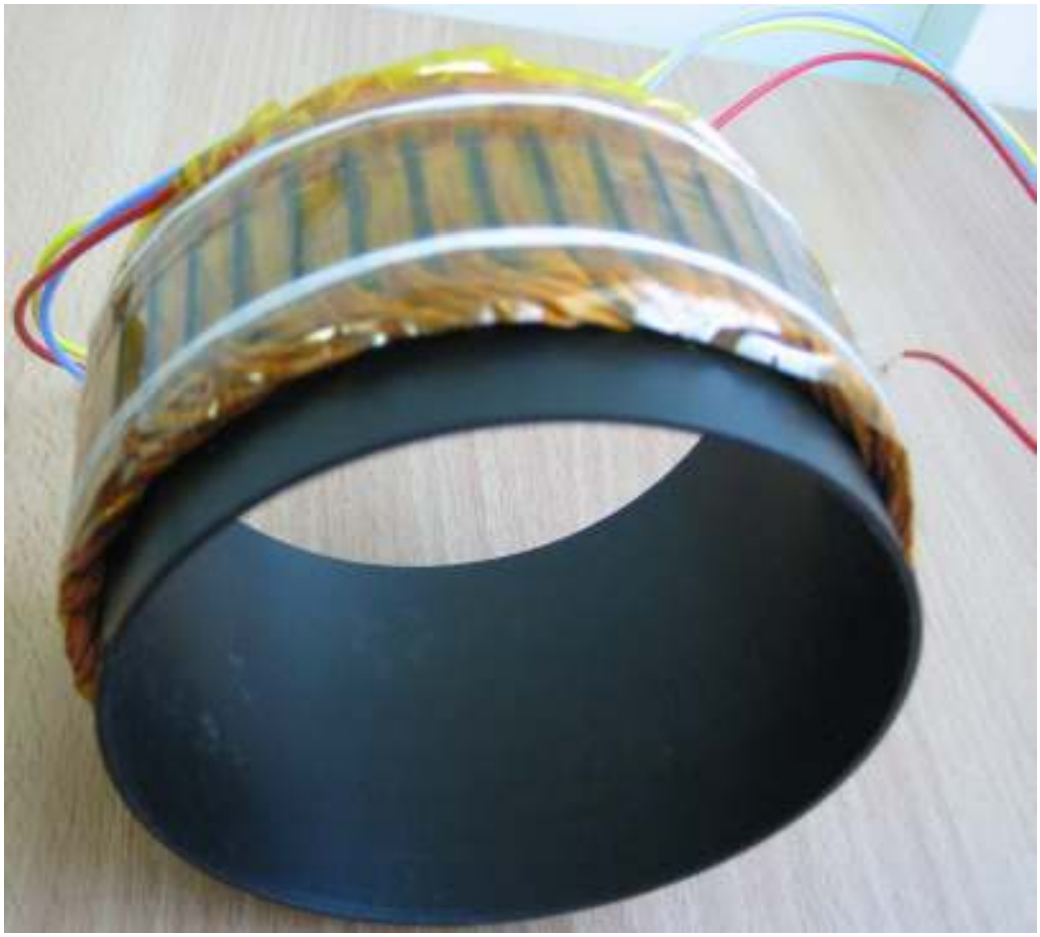

Figure 34: Slotless motor wound former

An aluminium sleeve is then added to encapsulate this entire assembly, including the coils and stator. The space inside this assembly is then filled with oil in order to pressure compensate the assembly. This forms the stator-coil assembly without the need for coatings such as epoxy for protecting the motor components.

5.1.2 Making the helical stator

The issue of the spring-like stator is not a straightforward one to solve. The difficulty inherent in attempting to form a helical stator of this type is due to the shape of a section of coil. In essence the rectangular-sectioned strip of steel is being bent on the long edge, and this creates extremely high stresses in the inner and outer edges of the wire. This causes difficulties in the actual bending of the wire, as shaping it into the correct helical shape against such high stresses is not an easy task. Also, the strip has a tendency to twist and fall on to its flat face, again due to the high stresses created when twisting it on its long edge and in a helical shape.

The technique developed in this project involves a number of stages in manufacturing a helical slotless stator. The first stage of this process involves forcing the steel into the helical winding shape. This is accomplished by bending the steel in a former that has thread-like grooves machined into it. There are a number of issues to be aware about, however, when using this method. The first is that the grooves cut into the former have to be of a certain pitch; too fine a pitch results in the walls of the groove becoming too thin, and the strip that is being formed on the former may damage the grooves and hence deform in shape. The second issue to note is that the former needs to be of a diameter that is sufficiently smaller than the actual diameter being formed. The reason for this is because the formed coils have to be allowed to ‘spring’ open naturally, to be able to form the helical stator shape. When the coils are

forced to be at a diameter that is too much smaller than its natural diameter, the stresses become too large and cause twisting in the coils. It was found, through trial and error, that in order to produce a stator of inner diameter 101.5mm the former had to be turned down to a diameter of 75mm.

Following winding the stator, the stator is then left wound on the former for a number of hours (in this project's case, the stator was left overnight, for approximately 12 hours). This ensures an even distribution of stresses on the formed coil, so that when the coil is released from the former it springs open uniformly. The stator is released a coil at a time, with each free coil stretched out as the next comes off in order to ensure that the coils do not entangle together when the entire stator is free of the former.

With this released stator, it is then wound on to another former that has a diameter equal to the required stator diameter. The coils are arranged to achieve the maximum stacking factor, and then bound together with steel wire. This stacked and bound stator is then heat treated to relieve the stresses within the coils. This is done by heating the stator in an oven up to 580°*C*. The stress relieving process only requires the temperature to be ramped up from 0°*C* to 580°*C* and then to be ramped down immediately after[69]. The heating up process takes approximately 90 minutes to complete. The stator is then left to air cool. The entire process takes approximately 120 minutes to complete, for the slotless motor. Figure 35 shows the stator after it is heat treated.

Figure 35: The heat-treated stator with coils stretched out

This stator is then fitted and tightened over the former containing the motor coils, and insulating varnish is then applied to the stator, which aids in insulating the steel as well as to glue the coils together and on to the surface of the former. Figure 36 shows the stator after it has been coiled and varnished, and Figure 37 shows the completed former-stator assembly.

Figure 36: Varnished stator

Figure 37: Completed stator-winding assembly

5.1.3 The prototype slotless thruster

The rotor and magnets were outsourced to a magnet manufacturer. The stator assembly is completed by fitting an aluminium sleeve around the stator/former, with O-rings in place to seal the gaps. Oil is then pumped, through openings in the sleeving, to fill up the remaining space inside the assembly. Nozzles with struts and bush bearings in the middle support the

rotor-propeller assembly through a shaft. Figure 38 shows an expanded view of the thruster parts.

Figure 38: Thruster parts expanded

In this picture, the encapsulated stator can be seen, with the rotor part and a propeller. The propeller is glued within the rotor ring. The nozzles fit on to the ends of the encapsulated stator assembly. Figure 39 shows the assembled thruster.

Figure 39: Slotless thruster

5.2 Testing the prototype thruster

Experimental testing was carried out on the demonstrator motor using a general-purpose dynamometer rig, as well as water loading the completed thruster assembly in a flow tank. It was not possible to load the motor to its thermal limit on the general-purpose dynamometer rig tests as water-cooling was not available. The tests carried out were sufficient to provide validation for the results obtained from finite element analysis, as well as provide an observation on the motor's characteristics. Thruster tests made, however, tests the motor's performance as a drive for a tip-driven thruster. Figure 40 shows a picture of the dynamometer test rig.

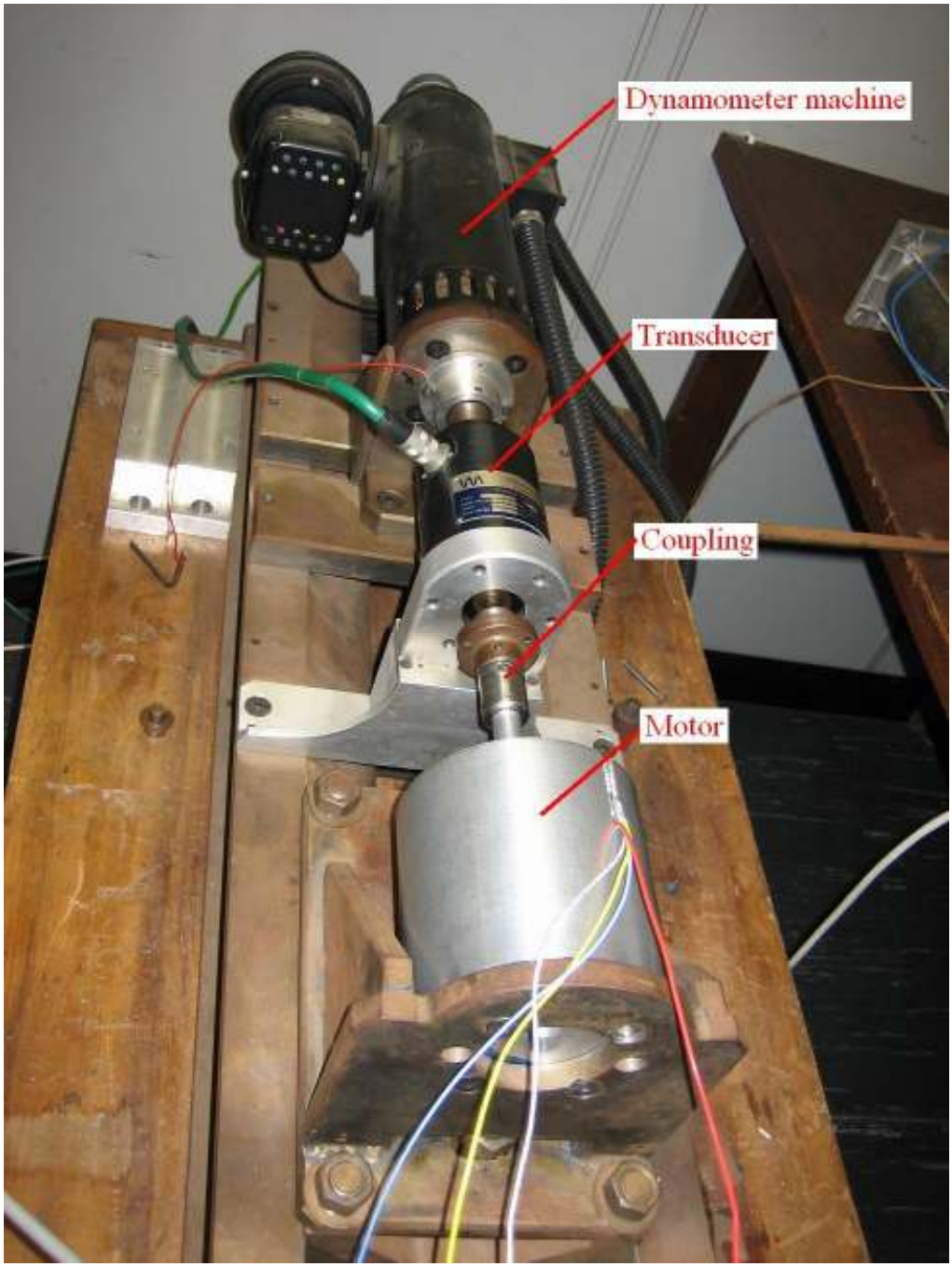

Figure 40: Dynamometer test rig

Dynamometer tests were conducted for the motor under no-load and load. No-load tests were conducted by disengaging the motor from the dynamometer

and collecting a series of voltage and current data. Load tests were conducted by connecting the motor to the dynamometer, and with the dynamometer running at a fixed speed, results on the torque on the shaft and winding voltage and current can be collected. Test results for motor torque at different input voltages and running speeds were collected. The tests were done for a maximum motor current of up to 11A and speed of 1000rpm (equating to approximately 11V on the d.c. link voltage). This limitation was enforced, as the motor does not have a proper cooling system at its windings, as the application is designed to operated underwater, and care had to be taken so as not to overheat the windings. Also, the rotor and magnets are not potted in epoxy, and as such care had to be taken so as not to run the rotor at too high a speed and allowing the magnets to slip from their position on the rotor. Bearing friction was also calculated from the tests.

The dynamometer has an error of approximately ±0.07Nm, due to the resolution of the torque measurement. Shaft vibrations, unbalanced loads on the motor or dynamometer drive, or cogging torque from the dynamometer drive can produce torque measurements of up to the magnitude of the dynamometer error, and these have to be taken into account as measurement errors when interpreting the results.

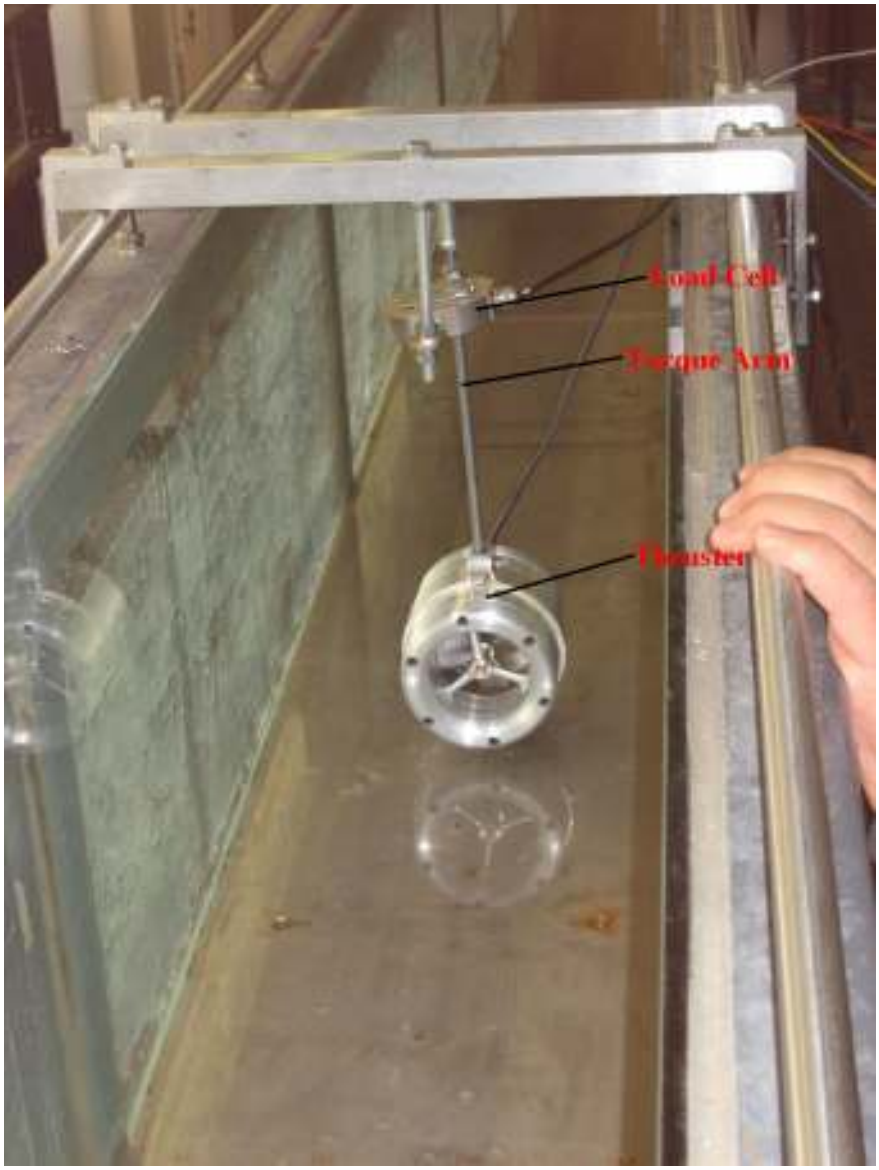

Figure 41: Testing the thruster in the flow tank

Figure 41 shows a picture of the thruster testing set-up for water loading tests in the flow tank. The tank dimensions are 300mm (W) x 390mm (H) x 900mm (L). The thruster is suspended in the tank on a torque arm that is held by a pivot point near the top frame. A load cell is attached to this torque arm on to a

fixed point. The tank is filled with water, and the thruster run at different speeds, and the thrust output measured at these speeds. A power analyser is used to measure frequency and power into the thruster. The load cell measurements taken at a low thruster rotational speed (from 200 - 1200rpm) have an error of ±0.05kg, and at higher thruster rotational speeds (from 1200rpm - 2600rpm) the error increases to ±0.5kg. The increase in error in the measurements is due to the onset of ventilation during higher testing speeds; air from the surface of the water is drawn into the propeller blades due to pressure differences generated by the thrust produced, and as the air reaches the propeller blades a sudden change in loading occurs. This causes the thruster to undergo sudden no-load conditions during ventilation, and this causes large changes to the thrust measurements. The thrusters was not tested up to the design speed of 3600rpm due to the lack of a suitable controller that was able to drive the thrusters up to the power level required (>200W).

Results for the dynamometer tests will be shown in subsection 5.2.2, while thruster test results will be shown under 5.4.2 to make direct comparisons with an existing slotted 70mm propeller diameter thruster.

An additional locked-rotor test was carried out following the tests described above, by locking the motor shaft against a load cell and measuring static torque. This is due to the poor accuracy of the dynamometer tests, as the motor torque values measured were at the lower end of the resolution of the torque

transducer used. The locked-rotor test allows a more accurate measurement of motor characteristics, as well as allows a more meaningful comparison between experimental and FEA results obtained. The results of this test is shown in Figure 50 under section 5.3 showing comparisons between experimental and FEA results.

5.2.1 Error analysis

Test	Instrument	Measurement taken	Error
Dynamometer test	Dynamometer torque transducer	Torque (Nm)	±0.07Nm
	Dynamometer speed transducer	Speed (rpm)	±0.1rpm
	Voltage probe	Voltage (V)	±0.01V
	Current clamp	Current (A)	±0.01A
Thruster test in flow tank	Load cell	Force (kg)	±0.05kg under low thrust conditions (thruster speeds <1200rpm) ±0.5kg under high thrust conditions (thruster speeds >1200rpm)
	Voltage probe	Voltage (V)	±0.01V
	Current clamp	Current (A)	±0.01A
Locked-rotor test	Load cell	Force (kg)	±0.01kg under static conditions

Table 11: Summary of instrumentation errors related to tests conducted

Table 11 shows a summary of the instrumentation errors for the measurement equipment used in the tests conducted. These errors are related to both instrument resolution, as well as dynamic conditions that may exist in each

test. Errors in measurements are obtained by analysing the instrument resolution, however no statistical error analysis can be conducted due to the small data sample size (of 1-2 data samples in each test).

These errors have to be taken into account when analysing the data collected, by adding these uncertainties to the measurements. In particular motor torque values collected on the dynamometer have to be verified using analysis methods due to the low values of torque measured, and large resolution errors.

5.2.2 Dynamometer load test results

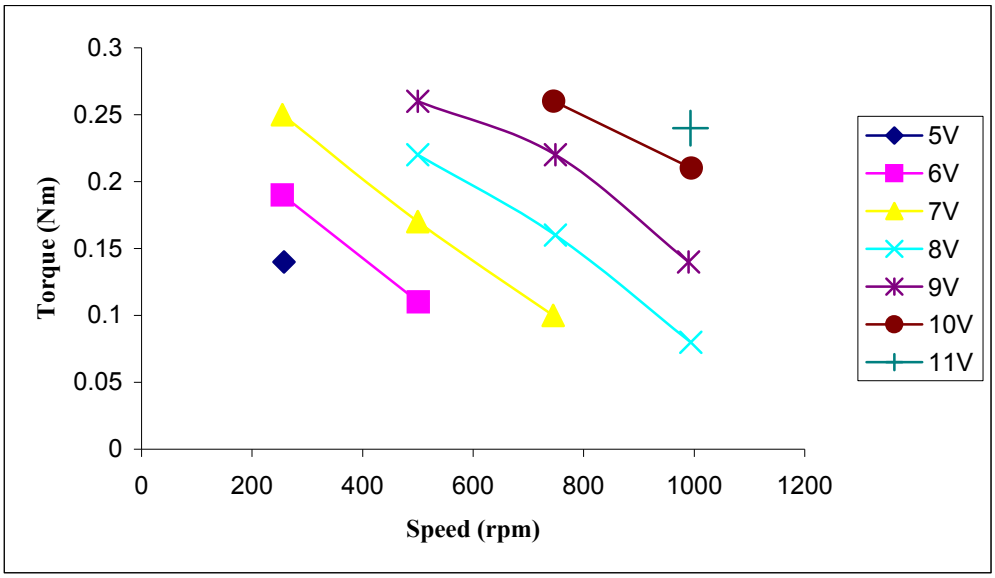

Figure 42: Shaft torque versus speed for motor load test results at various D.C. link voltages

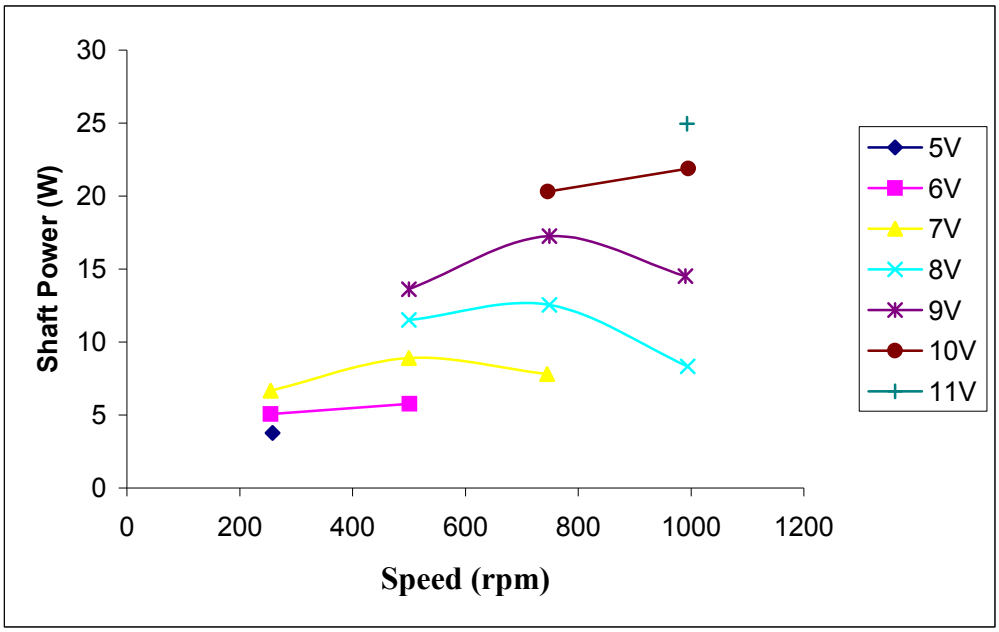

Figure 43: Graph of shaft power versus speed at various D.C. link voltages

Speed (rpm)	DC Link V (V)	Winding input power (W)	Torque on shaft (Nm)	Power developed on shaft (W)	Electromagnetic torque (Nm)	Electromagnetic power (W)	Motor efficiency (%)
258	5	11.38574744	0.14	3.782477555	0.21	5.673716333	49.83174239
255	6	16.69790662	0.19	5.073672136	0.26	6.942919765	41.57958195
255	7	23.06913195	0.25	6.67588439	0.32	8.545132019	37.04141117
501	6	15.63369218	0.11	5.771105705	0.21	11.01756544	70.47321457
500	7	21.82910405	0.17	8.901179186	0.27	14.13716694	64.76292801
500	8	29.71310699	0.22	11.51917306	0.32	16.75516082	56.38979737
500	9	37.04887201	0.26	13.61356817	0.36	18.84955592	50.87754336
745	7	18.99071884	0.1	7.801621757	0.2	15.60324351	82.16246917
749	8	27.32142944	0.16	12.54961546	0.26	20.39312511	74.64150132
749	9	36.09081876	0.22	17.25572125	0.32	25.09923091	69.54464259
746	10	44.15387003	0.26	20.31144371	0.36	28.12353744	63.69438833
994	8	22.45848279	0.08	8.327314928	0.2	20.81828732	92.69676637
990	9	31.81707825	0.14	14.51415806	0.26	26.95486497	84.71822824
995	10	41.53840583	0.21	21.88119284	0.33	34.3847316	82.77816857
993	11	49.99545965	0.24	24.95681204	0.36	37.43521807	74.87723551

Table 12: Test data for the slotless motor

Figure 42 shows shaft torque versus motor speed, obtained from motor load tests. Shaft torque measured in these tests refer to the torque developed on the external shaft connected to the motor, and is the net torque developed after overcoming motor losses such as bearing friction. It should be noted that the losses overcome in these tests include the friction in the motor test casing, and is not entirely reflective of the total motor electromagnetic torque, and the actual motor output torque developed in the thruster application for which this motor is designed for. However, it is useful to observe the trend and characteristics of the motor from these curves. From the curves, it can be seen that shaft torque decreases linearly with an increase in motor speed. This is an expected result, as for a given power:

$$P = \omega T \tag{36}$$

As such, when the motor speed increases, torque is expected to decrease linearly.

From Figure 43, it can be seen that the power developed on the motor shaft (friction and core loss not included) takes on a maximum curve trend. It can be seen from this graph that at different input voltages, there is an optimum operational point for the motor in order for it to produce maximum power output. This optimum point also shifts towards a higher operational speed as the input voltage increases.

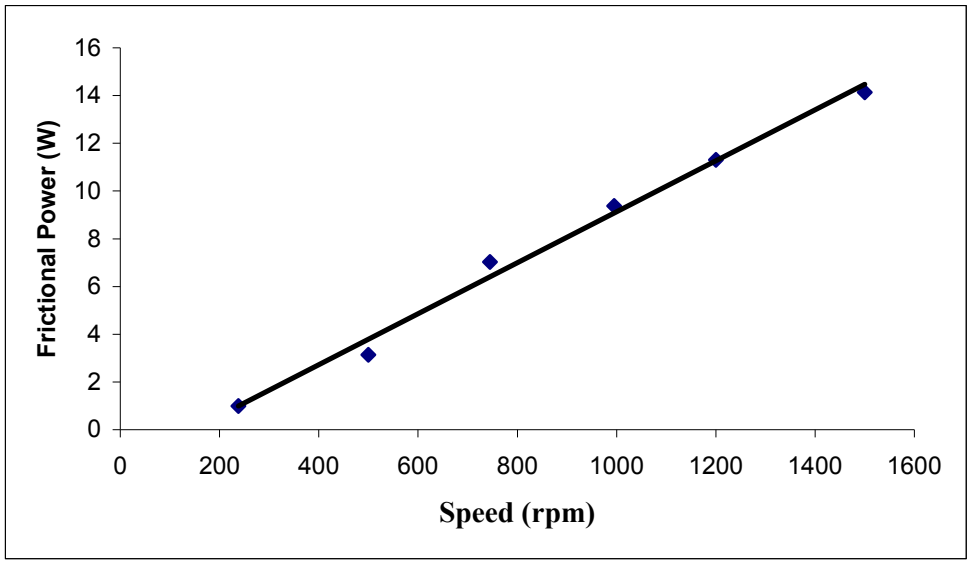

Figure 44: Test casing friction power loss versus speed

Figure 44 shows the power loss due to the friction developed in the motor test casing during the load tests. It can be seen that the friction power loss increases with motor speed. Equation 37 shows the relation between power developed to overcome friction, with friction.

$$P_{friction} = Fv = Fr\omega \tag{37}$$

Power to overcome friction has a linear relationship to the friction value of the surface, F, and tangential velocity at the point of contact, v. Tangential velocity is then related to rotational speed by $r\omega$ where r is the outer radius of the bearing. It can be seen from this equation that the measured power loss

due to friction in the motor test casing is expected. The power loss measured ranges between 1W to 14W in the range of motor speeds tested.

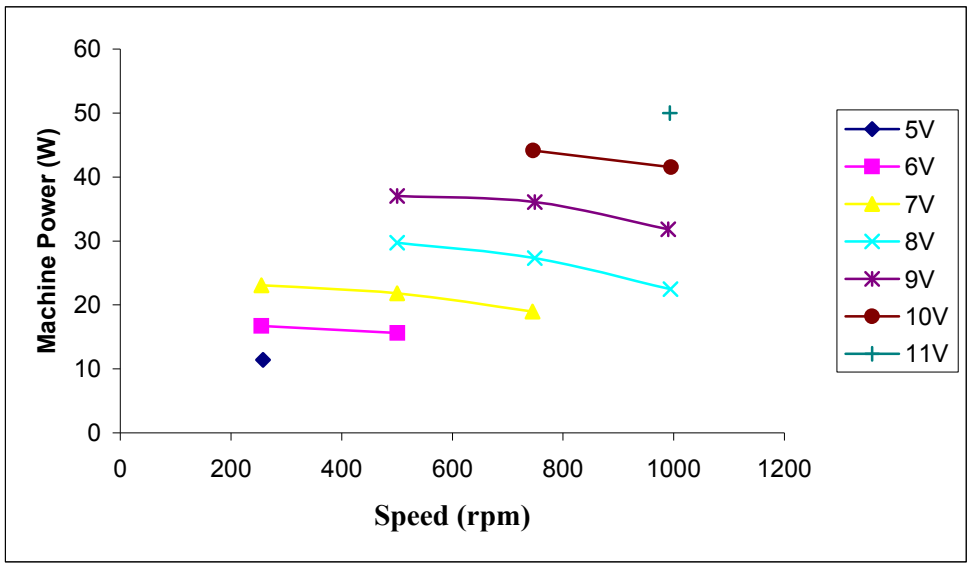

Figure 45: Machine input power versus speed at various D.C. link voltages

Figure 45 shows a graph of winding input power versus motor speed. This was measured by connecting voltage probes at the terminal leads of the motor, and by clamping the motor terminal leads with current clamps. The power drawn by the motor decreases with increasing speed. At a steady state, the losses in the motor are linear and hence power input requirements vary linearly as well. Equation 38 shows the relationship between machine output power, shaft power, frictional power shown above, and core losses, and Equation 39 shows the relationship between efficiency, machine output power, and machine input power. It should be noted in these results that core losses were not shown. This

is because the resolution of the results obtained from the dynamometer were too coarse, and it was difficult to determine the differences in torque measured that was due to friction loss and core loss. This however indicates that the core loss is minimal and does not contribute very much to the overall motor losses. It is also an indication of the effectiveness of the prototyping method for making the slotless stator using a helical winding method.

$$P_{output} = P_{shaft} + P_{friction} + P_{coreloss} \tag{38}$$

$$Efficiency, \eta = \frac{P_{output}}{P_{input}} \tag{39}$$

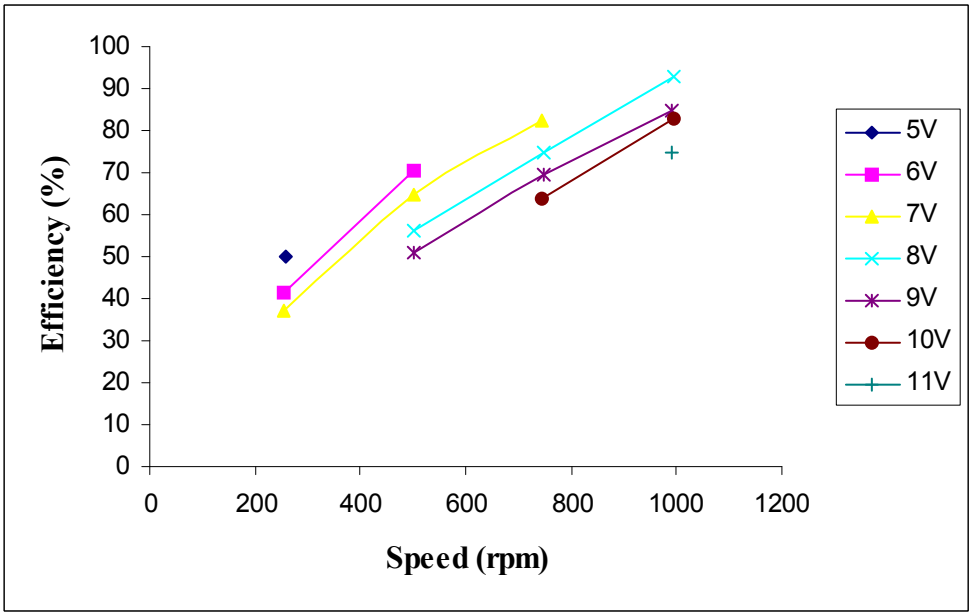

Figure 46: Motor efficiency versus speed at various D.C. link voltages

Figure 46 shows a graph of motor efficiency versus speed. The efficiency calculated here is for the motor electromagnetic efficiency, which accounts for the power output at the shaft as well as for friction losses. It can be seen that the efficiency increases with increasing speed, which is expected once again due to the reduction in required input power as speed increases. From these tests, the motor efficiency is approximately 35% at low speeds, but rises to as high as 90% at higher speeds. It can also be observed that the rate in increase of efficiency decreases with increasing speed, and as such it is expected that the efficiency would decrease at speeds higher than those conducted in these tests. There will be an optimum operational point depending on the power drawn and the running speed for the motor. It can also be seen that the efficiency improves with increasing speed and increasing input power. However, it is expected that there is an optimum operating point for input power and speed that will produce the motor maximum efficiency, however further tests need to be conducted to determine this point.

5.3 Comparisons between finite element analysis and experimental results

Following the presentation of experimental results obtained, it is of interest to make comparisons between the finite element analysis results and the experimental results obtained. This will lend confidence and validation to the design techniques used for designing this motor, and also serves to bring to light any errors that exist in the design techniques that will help in improving

the techniques for more accurate future designs. The results obtained for the motor at 1000 rpm were used for comparison, as these results had the greatest range of data points obtained that will allow for a better trend for comparisons.

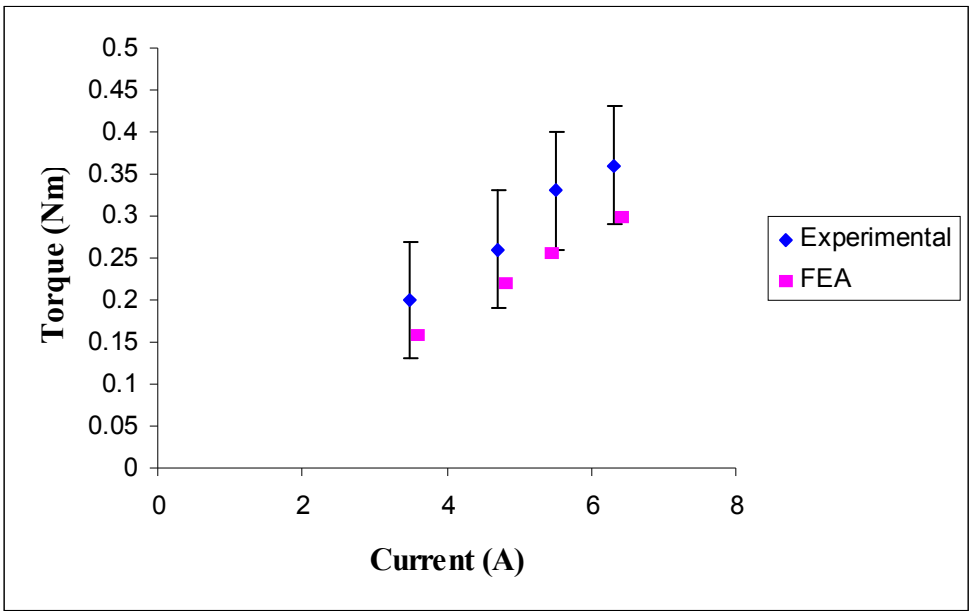

Figure 47: Electromagnetic torque versus winding RMS current for experimental and FEA results at an operating speed of 1000rpm

Figure 47 shows a comparison between the experimental and FEA results for the torque generated for certain winding currents. The experimental and FEA points do not line up exactly, on the current axis, due to slight errors resulting from minor differences in the adjustment for parasitic resistance losses that arises in the experimental case from cabling and the inverter circuit. This results in a slightly different current waveform when compared to that in FEA, and hence produces the slight difference in magnitude for current values seen.

It can be seen that the experimental torque values obtained are higher than that obtained from FEA. This is attributed to the large experimental errors that were seen when testing the motor. The FEA torque results still fall within the experimental errors observed, and as such some confidence can still be maintained in the experimental results obtained as well as in the validity of the FEA model used. It can be observed that the trends of both curves are similar, lending more confidence to the FEA model used for the design optimisation.

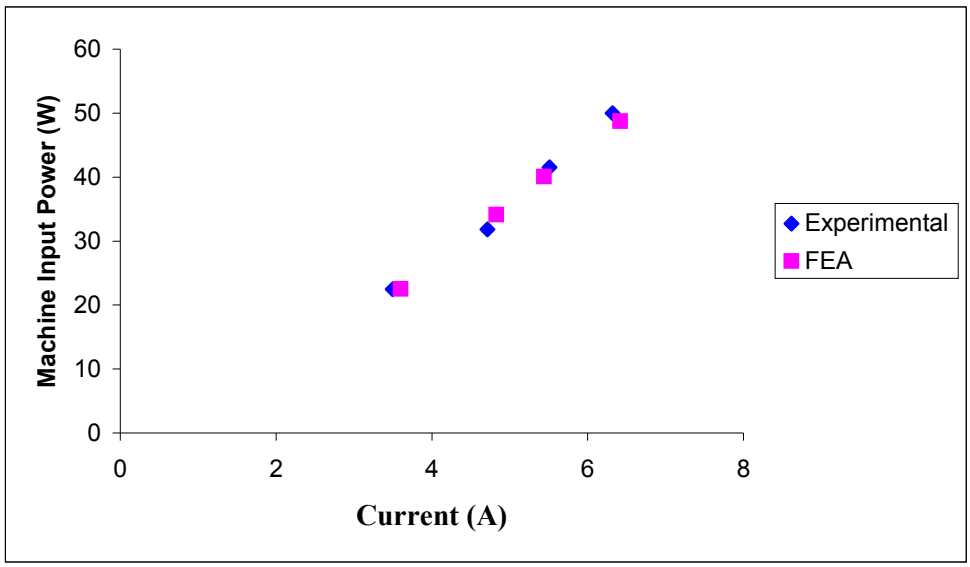

Figure 48: Machine input power versus winding RMS current for experimental and FEA results at an operating speed of 1000rpm

Figure 48 shows a graph of the winding input power versus winding RMS current for both experimental and FEA results. It can be seen that there is a close agreement between both results. This shows that the FEA model has a

reasonable degree of accuracy due to the actual motor power requirements matching. The next Figure 49 will show experimental and FEA efficiencies; however, due to the large experimental errors from torque measurement, these efficiency values will not show a good agreement.

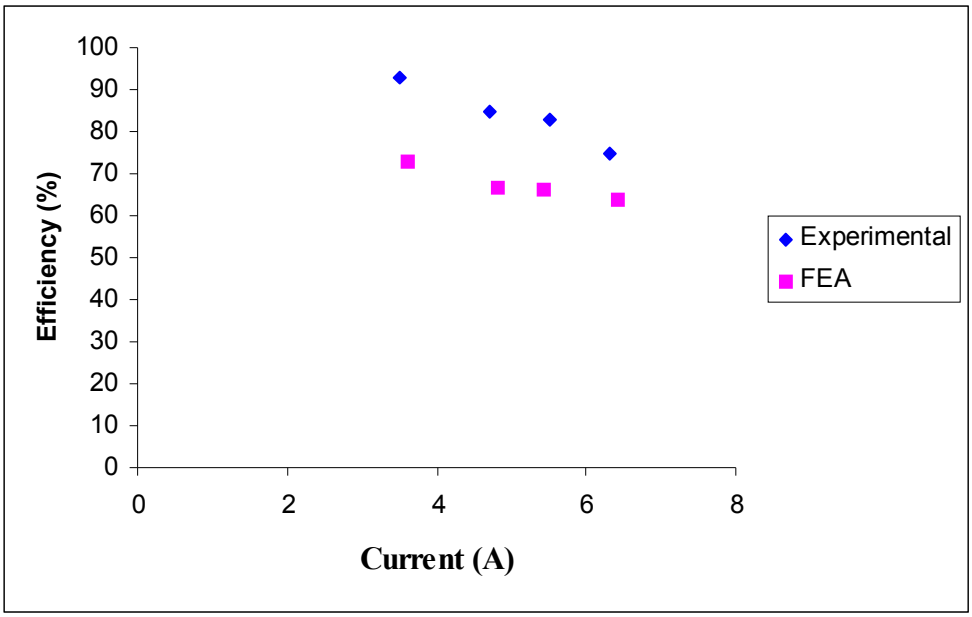

Figure 49: Motor efficiency versus winding RMS current for finite element and experimental results at 1000rpm

It should be noted, however, that the difference between both FEA and experimental values obtained are still within the boundaries of measurement errors.

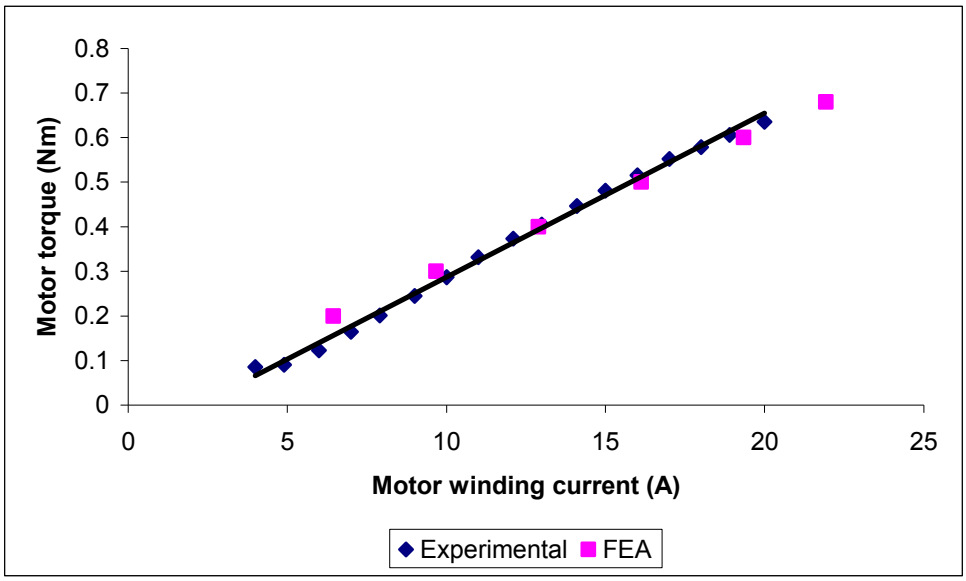

Figure 50: Graph of motor torque versus motor winding current under locked-rotor tests

Figure 50 shows a graph of motor torque versus motor winding current measurements taken under static conditions (locked-rotor tests). It can be seen that the motor requires 5A before producing any noticeable torque; this initial current is required in order to overcome friction and inertia in the machine. The torque then increases linearly with current, up to a value of 0.64Nm at 20A. It can also be seen from the figure that these results agree very well with finite element analysis. Comparing this figure with Figure 47, the torque measurements in this test are more reliable and gives confidence to the finite element analysis results obtained, hence showing that the efficiencies calculated through finite element in Figure 49 are the expected efficiencies.

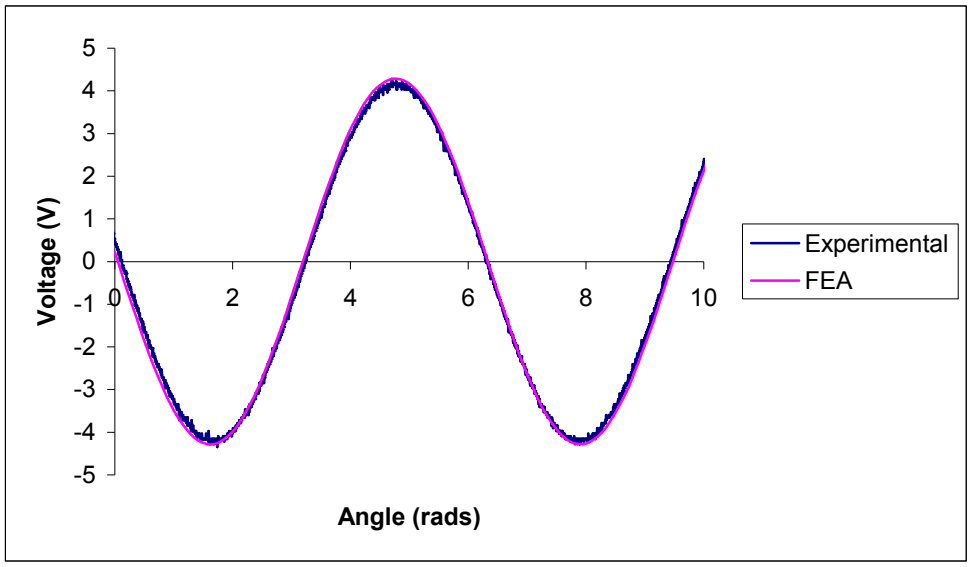

Figure 51: Comparisons of experimental and finite element analysis back emf results for the case of the motor running with 11V D.C. link and at 1000rpm

Figure 51 shows a comparison between experimental and finite element analysis back emf waveforms for a particular point of operation of the motor. It can be seen from the figure that results match very closely to one another, validating the accuracy of the finite element model used to aid in optimising the design of this slotless motor (and also hence validating the accuracy of the analytical technique used since the analytical results and FEA matched closely).

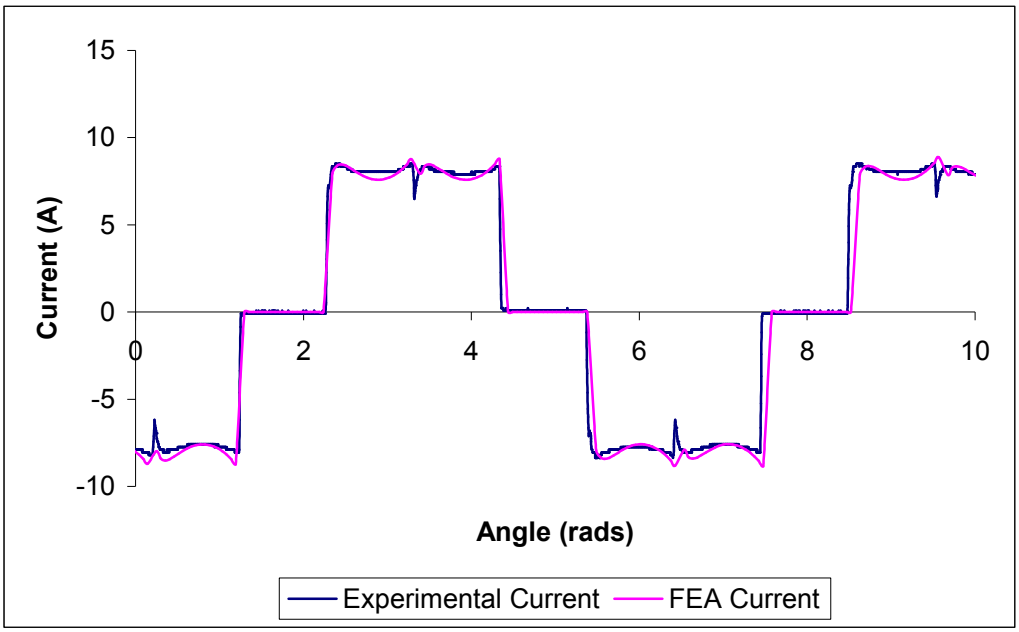

Figure 52: Winding current versus electrical angle from finite element and experimental results for the case of the motor running with 11V D.C. link and at 1000rpm

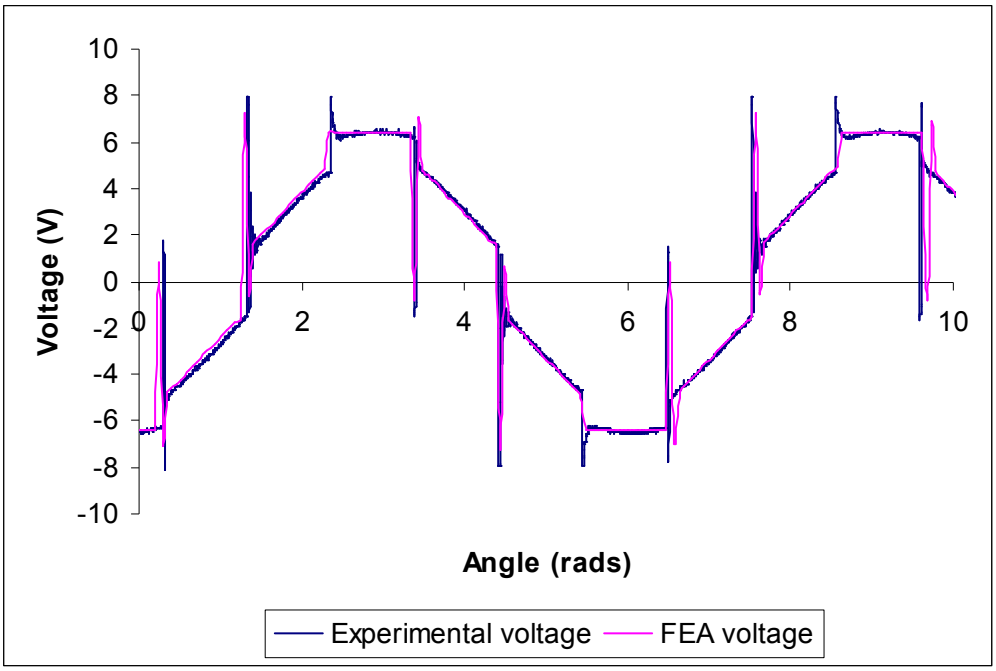

Figure 53: Winding line-to-line voltage versus electrical angle from finite element and experimental results for the case of the motor running with 11V D.C. link and at 1000rpm

Figure 52 and Figure 53 show comparisons between the winding currents and winding line to line voltages obtained from finite element analysis as well as experimentally. It can be seen that the waveforms agree very closely. It can be observed that the experimental current waveform has a slightly 'flatter' waveform. This is due to a higher back-EMF produced in the coils due to the slotless motor's low winding inductance. This causes the peak of the current to be slightly suppressed, hence creating this 'flat' top effect. This effect is also seen in the finite element analysis waveform, however a lower end-winding

value used in the model causes a slightly more pronounced effect of this 'dipping' compared to the experimental waveform.

It can be seen from the results shown above in this section that there is a good agreement in the results obtained from finite element analysis with the experimental results obtained. A prediction of the motor performance can be made to some degree, and confidence has been obtained to the validity of the techniques used for design optimisation.

5.4 Comparisons between slotted and slotless design

The final stage of this thesis is aimed to make comparisons between how this design compares to the existing slotted motor design. The slotted motor design has similar dimensions to the slotless design, with the main differences existing within the electromagnetic airgap of the motor. Table 13 shows the dimensions of the two designs.

Motor parameter	Slotless Motor	Slotted Motor
Stator steel thickness	1.25mm	1.5mm
Rotor steel thickness	1.5mm	1.5mm
Number of poles	16	16
Magnet thickness	4.5mm	3mm
Magnet pole-arc to pole-pitch ratio	0.833	0.833
Number of turns per pole	3	8
Motor active axial length	25mm	20mm
External stator diameter	104mm	104mm
Internal rotor diameter	73mm	73mm
Electromagnetic airgap	4mm	4mm

Table 13: Comparison of design parameters for the slotless and slotted motor designs

The slotless design is able to utilise a smaller back of core due to the decrease in magnetic flux density arriving at the steel surface, when compared to the slotted design. This allows for less material waste as well as a lighter stator. The disadvantage of the slotless design, however, is in order to compensate for the larger electromagnetic airgap, more magnet material needs to be used. In this case, a magnet thickness of 4.5mm compared to 3mm in the slotted case was used. A longer motor axial length is also used in the slotless design, but this was not due to any distinct disadvantage in the motor topology. It was identified in the design optimisation that the slotless motor is able to have a slightly longer axial length due to the available space on the thruster propeller, and it is worthwhile using this length in order to have a better machine efficiency. The constraints of both designs have still been met, however, with a 104mm outer diameter, 73mm inner diameter and a 4mm electromagnetic airgap in the motor.

Due to the commercial aspect of the existing 70mm slotted motor design, there are limitations to the results accessible for use to compare with the slotless design. As such, the following discussions will be made based on the results that are available.

5.4.1 Comparisons between analytical calculations

Data is available on the 70mm slotted design for analytical calculations performed on the motor. Table 14 summarises some of these values for comparison.

Motor parameter	Slotless Motor	Slotted Motor
Nominal torque	0.68Nm	0.68Nm
Nominal speed	3600rpm	3600rpm
Calculated winding voltage	29.3V	29V
Calculated winding peak current	21.93A	15.56A
Calculated core loss	8.16W	Yoke: 7.68W Teeth: 6.72W
Calculated motor efficiency	73.2%	82.2%

Table 14: Comparison between analytical values for slotless and slotted motor designs

It can be seen from Table 14 that the calculated motor efficiencies have a difference of approximately 9%, for similar output performances. This can be attributed to the difference in design for the motor topologies. In the slotted design, the teeth on the stator steel aid in focusing the magnetic flux produced by the permanent magnets, hence producing a higher torque per unit volume magnet. In addition, the teeth allow for a smaller electromagnetic airgap in the motor space compared to the slotless design, hence allowing a higher proportion of magnetic flux to reach the stator steel. These factors add together to allow a lower winding loading for the desired torque output, hence making

the machine a more efficient one. This can in fact be seen from the calculated winding peak currents, with the analytical calculations producing a winding peak current of 21.9A in contrast to the slotted motor calculations of 15.6A.

Comparing the core loss values between the slotless and slotted motor designs, it can be seen that the slotless motor has a calculated core loss value of 8.16W, whilst the slotted motor has a calculated core loss value of 7.68W at the stator yoke and 6.72W at the stator teeth. It can be seen that the core loss value differs by 0.5W, which is a negligible amount when compared to other motor losses such as winding heating loss. As such, it can be seen that the slotless design does not suffer from much additional losses, and in fact has less core loss overall due to the absence of teeth.

5.4.2 Comparisons between experimental results

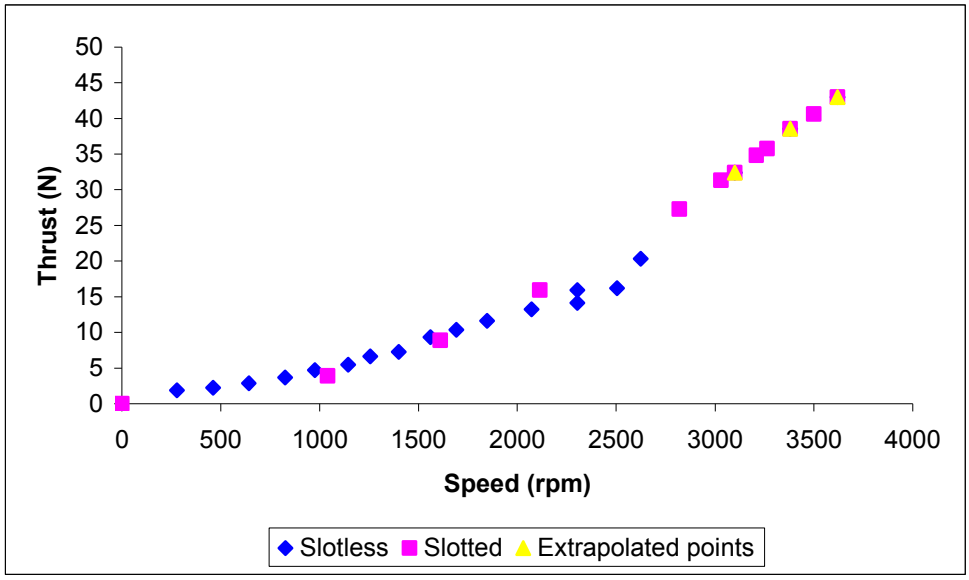

Figure 54: Comparison of thrust versus speed characteristics for the slotless and slotted thruster motor configurations for thruster load tests in water

Figure 54 shows a graph of thrust versus speed obtained from water tests with the motor fitted as a drive for the rim-driven thruster. This figure shows a good fit between the results obtained for the slotless thruster when compared to results obtained for an existing slotted thruster. This provides an indication of the performance of the propeller used in both thrusters, and confirms a similar propeller hydrodynamic characteristic. It can be seen that thrusts of as high as 21.6N (2.2kgf) were obtained for an operating speed of 2600rpm for the slotless motor, and it can be expected that the thrust produced by the slotless

thruster would approach that produced by the slotted thruster at higher operating speeds.

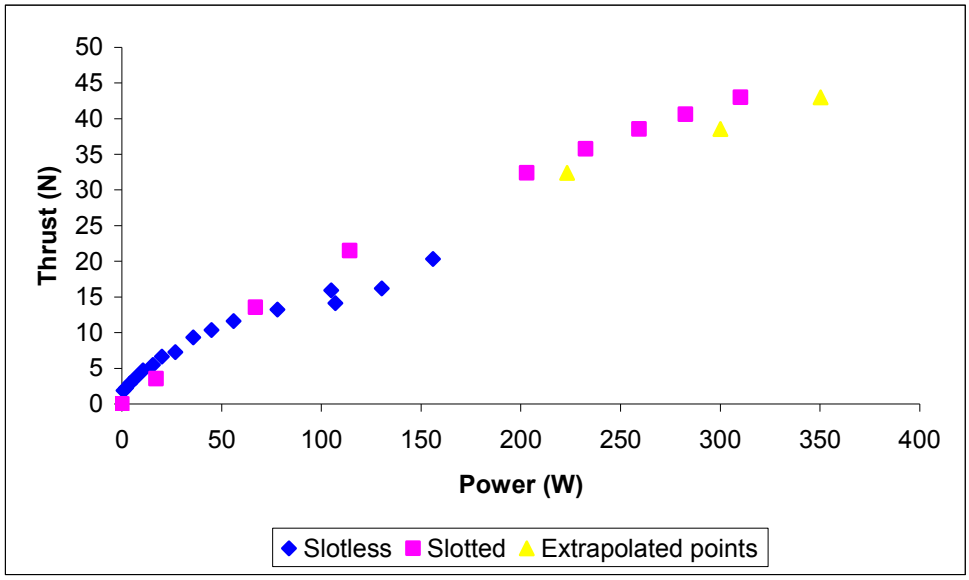

Figure 55: Comparison of thrust versus motor power characteristics for the slotless and slotted thruster motor configurations for thruster load tests in water

Figure 55 shows a graph of thrust versus motor power for the slotless and slotted thrusters. It can be seen that there are similar characteristics between thrusters at the lower operating points, however the slotless thruster begins to draw a higher power for similar thrust production at higher operating points. This indicates similar motor efficiencies for lower operating points, however as the slotless motor approaches the nominal operating point the motor

efficiency is less than that of the slotted motor. This is as expected, as it is predicted that the motor efficiencies differ by approximately 10%.

The testing of the slotless thruster could only be conducted at up to a motor power of 160W, as the motor controller used was unable to sustain higher power outputs and the thrust measurements were becoming very erratic due to ventilation occurring in the small tank. As such, the point at motor input power of 350W was extrapolated for the slotless thruster curve, based on the calculated efficiency difference between the slotless and slotted motors at that operating point. This is done to provide a better picture of the expected slotless thruster performance at that operating point.

5.4.3 Cost comparison

Motor Part	Slotted	Slotless
Stator laminations	£0.88 per lamination (using laser cutting) Each motor unit has 57 laminations = £50.16	£335 for 25kg of steel Each motor unit uses approximately 300g of steel = £4.02 Labour required to make stator approximately 3 man-hours @£10 per hour = £30 **Subtotal = £34.02**
Magnets Rotor	Magnet-rotor assembly = £120	Each magnet pole is £11 x 16 poles = £176 Magnet-rotor assembly = £295.50
Copper coils	£190	£250
Encapsulation	Uses polyurethane potting = £20	Uses self encapsulated former assembly = £75
Total	**£380.16**	**£654.52**

Table 15: Cost comparison between the slotted and slotless thrusters

Table 14 shows a cost comparison between the slotted and slotless thrusters, with costs derived for the slotless motor obtained from prototyping activities, and costs derived for the slotted motor obtained from production units. The main motor components are shown here for comparison, which is one of the drivers of this project, that is, to reduce the costs of manufacture of the motor for the tip-driven thrusters. Thruster propeller and housing are not shown as both the slotted and slotless thrusters utilise similar propeller and housings.

From the above cost comparison, it can be seen that the slotless motor designed for this project does not save costs in manufacturing. The overall costs of the slotless motor is 72% more expensive (it costs £273.92 more), with a significant amount of these costs attributed to the costs of the extra magnet material required in the slotless machine.

From the laminations perspective, it can be seen that the helical edge-wound method employed in the slotless motor offers a savings, although at not a very significant amount. The slotless motor laminations are £16 cheaper to make compared to the slotted motor, offering a savings of 32%; however the absolute costs of the laminations are not very high when compared to other motor components. The slotless motor utilises 87.5% more magnet material by volume, and the costs reflect this; the slotless motor magnet-rotor assembly costs £175.50 more than the slotted motor which is an increase in costs by 146%.

It should be noted however that the costs shown for the slotless motor are for a prototype, versus a production slotted unit. The slotted unit is able to command a lower cost due to higher volumes of production and favourable prices from manufacturers. It can also be noted that the edge-wound stator lamination technique does offer cost savings when compared to the conventional slotted laminations, although these savings might only be beneficial for other motor applications and not for the thruster application developed in this project.

The method of winding as well as protective encapsulation used in this project could be re-designed to have comparable costs as the methods utilised in the slotted motor, that is, to pot the motor windings in polyurethane or similar resins. This will lower costs to be more comparable to that of the slotted motor, and this method of protective encapsulation would be preferred in a thruster used in the actual underwater environment over the prototype built in this project. Sizing the thrusters to larger diameters may also reduce the proportion of flux losses in the slotless machine when compared to that of the slotted machine, hence allowing for a more comparable volume of magnet material used and lowering the cost difference required in both machine topologies for magnetic material. It can also be noted that laminations in machines can often be more than that used in the slotted machine (57 laminations), and as the number of laminations increase the cost savings offered by the edge-wound slotless lamination may become more attractive.

5.5 Design options

The slotless machine designed in this project has been optimised to fit within the constraints of the application required. However, this does not produce the optimum efficiency that the machine could have. The following are recommendations on design options that could be carried out in order to produce a more efficient slotless machine.

Bigger diameter

Increasing the overall diameter of the machine will allow for more copper to be fitted in the electromagnetic airgap of the machine. This improves the efficiency of the machine, by allowing a lower current to be drawn for the same torque generation. It is expected that there will be an optimum point at which increasing this diameter will cause efficiency to decrease, unless additional magnet material is used. However, for the purposes of the current design, a bigger diameter would allow for an increase in efficiency.

Longer axial length

It has been shown in the optimisation studies that increasing the motor axial length also increases efficiency. The limitation in this project is due to the available axial space allowed, due to hydrodynamic limitations. It is expected, however, if the overall volume of the thruster is increased (hence diameter is icreased too), the motor axial length can then be increased without increasing

the hydrodynamic drag appreciably. As discussed in Chapter 4, increasing the axial length will increase the machine efficiency.

Different operating point

Running the motor at a different operating point will also improve machine performance. It was seen from the studies done in this project that the operating point that the machine was designed for was not the point of best operating performance for a machine with such constraints. At a lower operating point, for example, it can be seen that the machine efficiency was in the 80-90% range when compared to the predicted efficiency of 73% at the operating point designed for. Selecting a suitable operating point for the machine under the specific design constraints can help in producing the best performance for the machine in consideration.

Chapter 6 Conclusions

This thesis has presented the work that has been carried out in designing, building, and evaluating a novel motor topology for use with underwater propulsion. Investigation was carried out into the slotless motor topology for this purpose. A literature review was carried out that revealed that this motor topology has not been applied to the application of an integrated thruster previously.

With respect to the achievable objectives of the project outlined in Chapter 1:

1) *To develop a combinational approach to designing electric motors for the integrated thruster through the use of analytical and generic Finite Element (FE)/circuit model of brushless Permanent Magnet (PM) motors.*

A design optimisation process for designing electric motors for integrated thrusters has been demonstrated in this thesis. The design issues and constraints related to the application were highlighted and discussed. The design process consists of the use of an analytical iteration technique that makes use of a solution to magnetic scalar potential obtained by solving Laplace's and Poisson's equations coupled with analytical derivations for motor torque, losses and efficiency. The process is then followed by a validation of the design by finite element analysis, with the analytical stage yielding fast designs and the finite element analysis yielding a slower and

more computer intensive analysis that is more accurate when compared to the analytical stage.

2) *To use analytical and FEA tools to optimise the design of a slotless motor for an integrated motor, and investigating the difficulties of manufacture of this topology*

The design optimisation process developed was then applied to designing a slotless motor for use with the integrated thruster. The difficulties of manufacture for this design primarily consisted of finding a method for fixing the motor winding to the surface of the stator, as well as manufacturing the stator itself. To this end, a non-conducting nylon former was devised for winding the coils on as well as encapsulating the entire stator unit, and the manufacture of the stator uses a helical-winding method. Both methods are novel, and have been shown to work with success, with no significant difference in performance from a conventionally made motor. It was found in this design process that the optimum motor configuration that fits within the constraints has the following parameters:

Motor parameter	Value
Stator steel thickness	1.25mm
Rotor steel thickness	1.5mm
Number of poles	16
Magnet thickness	4.5mm
Magnet pole-arc to pole-pitch ratio	0.833
Number of Phases	3
Number of turns per phase	48
Motor active axial length	25mm
External stator diameter	104mm
Internal rotor diameter	73mm
Electromagnetic airgap	4mm
Nominal torque	0.68Nm
Nominal speed	3600rpm
Calculated motor efficiency	73.19%

Table 16: Slotless motor parameters

3) *To build a demonstrator slotless PM motor thruster*

A demonstrator thruster has been built to validate the feasibility of the slotless motor topology. The material selected for making the helical edge-wound stator was mild steel, as conventional electrical steels are brittle and hence cannot be edge-wound. A technique for the manufacture of the prototype helical edge-wound stator from available manufactured steel strips was developed, which consisted of winding the coils of the stator in a grooved former and then normalising the stresses in the coils developed.

4) *To test and investigate the characteristics of this new motor design and validate the design results obtained.*

The results show that compared to a slotted machine in the same volume, the slotless machine favours having thicker magnets, which increases magnet cost.

More crucially, the slotless machine was found to be 10% less efficient than an optimised slotted machine in the same diameter.

A cost evaluation was also conducted, which yielded that the overall costs of the prototype slotless motor built in this project is 72% more expensive when compared with the production slotted motor, with a significant amount of these costs attributed to the costs of the extra magnet material required in the slotless machine. The laminations for the slotless motor are 32% cheaper to manufacture, but these costs are offset by the need for more magnet material, which increases the costs by 146%.

6.1 Future work

A slotless motor for use with the integrated thruster concept has been designed, built and tested. There is scope for more work to be done on this design in further improving and testing the design as well as in further investigating various aspects of the motor's characteristics. As such, there are a few aspects that are proposed for future work for anyone who wishes to continue the work carried out in this thesis:

1) *Investigate suitable materials, and core losses in helical edge-wound laminations*

A novel approach derived from this research is the manufacture of slotless motor stators using a helical-winding method. This helical stator has been used

in this project and the motor tested overall; further studies could be conducted into the selection of a suitable material for use in making these helical edge-wound stators due to the unsuitability of conventional electrical steels for this purpose. Core losses in laminations formed using this method can also be further investigated, in particular when a suitable material with available core loss data is used, and in the examination of how stresses formed in the material when edge-wound affect core losses.

2) *Investigation into the use of a Halbach array of magnets*

Further work could be done in investigating the use of Halbach arranged magnets. The Halbach array offers a potential as an alternative magnet arrangement for the slotless motor topology due to the lack of a need for a rotor ring, which would reduce the rotor inertia for the thruster. Additionally, the Halbach array concentrates the flux produced on to the airgap and this may improve the efficiency in a slotless motor.

3) *Investigation into the hydrodynamics of the existing slotless thruster design*

The work undertaken in this project is focused on optimising the motor driving the rim-driven thruster. Additional work can be done on optimising the hydrodynamics of the thruster propeller, as well as the duct and nozzles, in order to increase the thrust produced by the thruster for the same operating point, hence improving the overall device efficiency.

References

[1] S.M. Abu Sharkh and S.H. Lai, “Finite element analysis of a miniature electric thruster”, *Digest of the Eleventh Biennial IEEE Conference on Electromagnetic Field Computation (CEFC)*, Seoul, Korea, 235,2004

[2] A.W.Hughes, S.Abu-Sharkh, and S.R.Turnock, "Design and testing of a novel electromagnetic tip-driven thruster", *International Offshore and Polar Engineering Conference (ISOPE)*, 2000, pp. 299-303

[3] S.M. Abu-Sharkh, M.R.Harris, S.R.Turnock, R. Crowder, and P. Chappell, "Prototype integrated electric thrusters for work-class underwater vehicles : design construction and test", EPSRC Research Grant Report, 2002, pp. 1-8

[4] D. Given, "ROV review 1993-1994, 5th Edition", Spring Valley, Calif.: Windate Enterprises, 1993

[5] S.M. Abu-Sharkh, “Characterisation of Unmanned Underwater Vehicles and Their Thruster Systems”, Technical Note UVD05, *Design Studies of Power Electronic Drive Systems for the Thrusters of Unmanned Underwater Vehicles*, June 1995

[6] S.M. Abu-Sharkh, “Electro-Hydraulic Thruster Drive Systems”, Technical Note UVD02, *Design Studies of Power Electronic Drive Systems for the Thrusters of Unmanned Underwater Vehicles*, December 1993

[7] S.M. Abu-Sharkh, “Electric Motors for the Thrusters of UUVs”, Technical Note UVD04, *Design Studies of Power Electronic Drive Systems for the Thrusters of Unmanned Underwater Vehicles*, July 1994

[8] S.M. Abu-Sharkh, “Design and Performance of an Integrated Thruster Motor”, Technical Note UVD06, *Design Studies of Power Electronic Drive Systems for the Thrusters of Unmanned Underwater Vehicles*, June 1995

[9] F.R.Haselton, "Submarine Hydrodynamic Control System", US Patent number US3101066, 20 August 1963

[10] A. Ono and K. Yamamoto, "Electrically driven propeller", Patent number GB1439806, 16 June 1976

[11] O.S.Taylor, J.R.Repp, and D.W.Brown, "Submersible electric propulsion motor with propeller integrated concentrically with motor rotor", US Patent number US4831297, 16 May 1989

[12] v.C. Dietrich, "Strahlantrieb mit Elektromotor", 2001

[13] K.M.Richardson, C.Pollock, and J.O.Flower, "Design of a Switched Reluctance Sector Motor For An Integrated Motor/Propeller Unit", *Electrical Machines and Drives, 1995. Seventh International Conference on* (Conf. Publ. No. 412), 11-13 Sep 1995, pp. 271 - 275

[14] C.A.Garis, Jr., "Marine propulsor", US Patent number US5078628, 7 January 1992

[15] S.M. Abu Sharkh, S.H. Lai and S.R. Turnock, "A Structurally Integrated Brushless PM Motor for Miniature Propeller Thrusters", *IEE Proc.-Electr Power Appl*, **151** (5), pp. 513-519, (2004)

[16] G.C. Kennedy and J.K.Holt, "Developing a high efficiency means of propulsion for underwater vehicles", *Southcon Conference Record*, 1995, pp. 352-356

[17] O. Krovel, R. Nilssen, S. E. Skaar, E. Lovli, N. Sandoy, "Design of an integrated 100 kW Permanent Magnet Synchronous machine in a prototype thrusters for ship propulsion", *International Conference on Electrical Machines ICEM2004*, Krakow, Poland, 2004, pp.117-118

[18] "The Schilling electric ring thruster", www.ssaalliance.com last accessed on 1 February 2006

[19] M. Lea, D. Thompson, B. Van Blarcom, J. Eaton, J. Friesch, J. Richards, "Scale model testing of a commercial rim driven propulsor pod", *Journal of Ship Production*, **19** (2), 2004, pp. 121-130

[20] J. Richards, 'Further development in pod propulsion,' *New Wave*, **1**, 2003, p. 4

[21] "Rolls-Royce introduces Rim Drive thruster technology", Press release published on http://www.rolls-royce.com/marine/overview/news/2005/newsitem12.htm, 15 November 2005, last accessed on 1 February 2006

[22] S. M. Abu Sharkh, A. Hughes and S. R. Turnock, "Design and performance of an electric tip-driven thrusters", *Proc. Instn Mech. Engrs M: J. Engineering for the Marine Environment*, **127**, 2003, pp. 133-147

[23] S.M. Abu-Sharkh, M.R. Harris, R.L. Stoll, "Design and performance of an integrated thruster motor**",** *Electrical Machines and Drives, Seventh International Conference on* (Conf. Publ. No. 412), 11-13 Sep 1995, pp. 395 - 399

[24] S.M., Abu-Sharkh, M.R. Harris, "Electric thrusters for autonomous underwater vehicles**",** *Autonomous Underwater Vehicles and their Systems - Recent Developments and Future Prospects, IEE Colloquium on*, pp. 5/1-5/6, 1 May 1996

[25] Nippon Denso Kabushiki Kaisha, "A Helical Strip Forming and Take-up Means for Stator Cores", US Patent number US1162395, 4 November 1966

[26] S. Nakamura and T. Shiga, "AC generator for vehicle with helical stator having bolt recesses on outer cylindrical surface", US Patent number US6337530, 8 January 2002

[27] V.T. Belikov, A.D. Ivlev, and V.G. Chelak, "Electric Motor having Helical Stator", US Patent number US4439702, 27 March 1984

[28] B.F. Hart, R.P. Carlson, and A. Zubal, "Electric Motor Edgewise Wound Helical Core", US Patent number US3243623, 29 March 1966

[29] JFE Steel Corporation, “Electrical Steel Sheets”, http://www.jfe-steel.co.jp/en/products/electrical/aboutsupercore/english.html last accessed on 1 February 2006

[30] T.R.England, "Unique surface-wound brushless servo with improved torque ripple characteristics", *IEEE Transactions on Industry Applications*, 1988, pp. 972-977

[31] U.K.Madawala, A.W.Green, and J.T.Boys, "A brushless ironless DC machine", *IEE 4th International Conference on Power Electronics and Variable-Speed Drives*, 1990, pp. 440-445

[32] Z.Q.Zhu, Z.P.Xia, D.Howe, and P.H.Mellor, "Reduction of cogging force in slotless linear permanent magnet motors", *IEE Proceedings on Electric Power Applications*, 1997, pp. 277-282

[33] Y. Chen, J. Shen, and Z. Fang, "Topology and Preliminary Design of Slotless Brushless DC Motor", *IEEE International Electric Machines and Drives Conference Record*, 1997, pp. 7.1-7.3

[34] T. Kosaka, N. Matsui, T. Shikayama, and R. Oguro, "Drive Characteristics of Slotless PM Motors", *34th IAS Annual Meeting Conference Record (IEEE)*, 1999, pp. 894-899

[35] E.A.Mendrela, R. Beniak, and R. Wrobel, "Influence of stator structure on electromechanical parameters of torus-type brushless DC motor", *IEE Transactions on Energy Conversion*, 2003, pp. 231-237

[36] E.Spooner and B.J.Chalmers, "'TORUS' : A slotless, toroidal-stator, permanent-magnet generator", *Electric Power Applications, IEE Proceedings B*, Volume 139, Issue 6, Nov. 1992, pp. 497 - 506

[37] R. Krishnan, "Electric Motor Drives: Modeling, Analysis, and Control", Prentice Hall, 2001, p. 6

[38] J. R. Hendershot and T. J. E. Miller, "Design of Brushless Permanent Magnet Motors", Magna Physics Publications, 1994

[39] A. Binder, "Comparison of the electromagnetical performance of simplex wave and lap windings", *Energy Conversion, IEEE Transactions on*, Volume 8, Issue 4, Dec. 1993, pp. 698 - 703

[40] Z.P. Xia, Z.Q. Zhu and D. Howe, "Analytical Magnetic Field Analysis of Halbach Magnetized Permanent-Magnet Machines", *IEEE Transactions on Magnetics*, Volume 40, Number 4, July 2004, pp. 1864 - 1872

[41] Z.Q. Zhu, K. Ng and D. Howe, "Analytical Prediction of Stator Flux Density Waveforms and Iron Losses in Brushless DC Machines, Accounting for Load Condition", *Proceedings of the 5th International Conference on Electrical Machines and Systems (ICEM)*, Volume 2, August 2001, pp. 814 - 817

[42] K.J. Binns, P.J. Lawrenson, "Analysis and Computation of Electric and Magnetic Field Problems", Elsevier, September 1973

[43] W.J. Gibbs, “Tensors in Electrical Machine Theory”, Chapman and Hall, 1952

[44] T.K. Chung, S.K. Kim, and S. Hahn, “Optimal Pole Shape Design for the Reduction of Cogging Torque of Brushless DC Motor using Evolution Strategy”, *IEEE Transactions on Magnetics*, Volume 33, Number 2, March 1997, pp. 1908 - 1911

[45] G.H. Jang, and J.H. Chang, “Development of Dual Air Gap Printed Coil BLDC Motor”, *IEEE Transactions on Magnetics*, Volume 35, Number 3, May 1999, pp. 1789 - 1792

[46] T.J.E. Miller and R. Rabinovici, “Back-EMF waveforms and core losses in brushless DC motors”, *IEE Proceedings in Electrical Power Applications*, Volume 141, Number 3, May 1994, pp. 144 - 154

[47] G. Madescu, I. Boldea, and T.J.E. Miller, “An Analytical Iterative Model (AIM) for Induction Motor Design”, *Industry Applications Conference, 1996. Thirty-First IAS Annual Meeting, IAS '96., Conference Record of the 1996 IEEE,* Volume 1, 6-10 October 1996, pp. 566 - 573

[48] K.F. Rasmussen, J.H. Davies, T.J.E. Miller, M.I. McGilp, and M. Olaru, “Analytical and Numerical Computation of Air-Gap Magnetic Fields in Brushless Motors with Surface Permanent Magnets”, *IEEE Transactions on Industry Applications*, Volume 36, Number 6, December 2000, pp. 1547 - 1554

[49] Z.Q. Zhu, D. Howe, E. Bolte, and B. Ackermann, "Instantaneous magnetic field distribution in brushless permanent magnet DC motors. I. Open-circuit field", *IEEE Transactions on Magnetics*, Volume 29, Issue 1, Part 2, January 1993, pp. 124 - 135

[50] N. Boules, "Two-dimensional Field Analysis of Cylindrical Machines with Permanent Magnet Excitation", *IEEE Transactions on Industry Applications*, Volume IA-20, October 1984, pp. 1267 - 1277

[51] N. Boules, "Prediction of no-load flux-density distribution in permanent-magnet machines", *IEEE Transactions on Industry Applications*, Volume IA-21, June 1985, pp. 633 - 643

[52] A. Hughes and T.J.E. Miller, "Analysis of fields and inductances in air-cored and iron-cored synchronous machines", *Proceedings of the Institute of Electrical Engineering*, Volume 124, Number 2, February 1977, pp. 121 - 126

[53] Z.Q. Zhu, and D. Howe, "Instantaneous magnetic field distribution in brushless permanent magnet DC motors. II. Armature-reaction field", *IEEE Transactions on Magnetics*, Volume 29, Issue 1, Part 2, January 1993, pp. 136 - 142

[54] Z.Q. Zhu, and D. Howe, "Instantaneous magnetic field distribution in brushless permanent magnet DC motors. III. Effect of stator slotting", *IEEE*

Transactions on Magnetics, Volume 29, Issue 1, Part 2, January 1993, pp. 143 - 151

[55] Z.Q. Zhu, and D. Howe, "Instantaneous magnetic field distribution in permanent magnet brushless DC motors. IV. Magnetic field on load", *IEEE Transactions on Magnetics*, Volume 29, Issue 1, Part 2, January 1993, pp. 152 - 158

[56] K. Atallah, Z.Q. Zhu, D. Howe and T.S. Birch, "Armature Reaction Field and Winding Inductances of Slotless Permanent-Magnet Brushless Machines", *IEEE Transactions on Magnetics*, Volume 34, Number 5, September 1998, pp. 3737 - 3744

[57] K.F. Rasmussen, J.H. Davies, T.J.E. Miller, M.I. McGilp and M. Olaru, "Analytical and Numerical Computation of Air-Gap Magnetic Fields in Brushless Motors with Surface Permanent Magnets", *IEEE Transactions on Industry Applications*, Volume 36, Number 6, December 2000, pp. 1547 - 1554

[58] Z.Q. Zhu, D. Howe, and C.C. Chan, "Improved analytical model for predicting the magnetic field distribution in brushless permanent-magnet machines", *IEEE Transactions on Magnetics*, Volume 38, Issue 1, January 2002, pp. 229 - 238

[59] J. Faiz, and H. Jafari, "Two-Dimensional Magnetic Field Analysis of Internal-Rotor Permanent-Magnet Motors", *IEEE Transactions on Magnetics*, Volume 35, Number 5, September 1999, pp. 4232 - 4237

[60] A.B. Proca, A. Keyhani, A. EL-Antably, W. Lu, and M. Dai, "Analytical Model for Permanent Magnet Motors With Surface Mounted Magnets", *IEEE Transactions on Energy Conversion*, Volume 18, Number 3, September 2003, pp. 386 - 391

[61] X. Wang, Q. Li, S. Wang, and Q. Li, "Analytical calculation of air-gap magnetic field distribution and instantaneous characteristics of brushless DC motors", *IEEE Transactions on Energy Conversion*, Volume 18, Issue 3, September 2003, pp. 424- 432

[62] C. Mi, M. Filippa, W. Liu, and R. Ma, "Analytical method for predicting the air-gap flux of interior-type permanent-magnet machines", *IEEE Transactions on Magnetics*, Volume 40, Issue 1, January 2004, pp. 50-58

[63] M.A. Jabbar, N.P. Hla, Z. Liu, and C. Bi, "Modeling and numerical simulation of a brushless permanent-magnet DC motor in dynamic conditions by time-stepping technique", *IEEE Transactions on Industry Applications*, Volume 40, Issue 3, May-June 2004, pp. 763- 770

[64] U. Kim, and D.K. Lieu, "Magnetic field calculation in permanent magnet motors with rotor eccentricity: without slotting effect", *IEEE Transactions on Magnetics*, Volume 34, Issue 4, July 1998, pp. 2243 - 2252

[65] S. Hwang, J. Eom, Y. Jung, D. Lee, and B. Kang, "Various design techniques to reduce cogging torque by controlling energy variation in permanent magnet motors", *IEEE Transactions on Magnetics*, Volume 37, Issue 4, July 2001, pp. 2806 - 2809

[66] H. Cho, and H. Jung, "Analysis and design of synchronous permanent-magnet planar motors", *IEEE Transactions on Energy Conversion*, Volume 17, Issue 4, December 2002, pp. 492 - 499

[67] A. Parviainen, M. Niemela, and J. Pyrhonen, "Modeling of axial flux permanent-magnet machines", *IEEE Transactions on Industry Applications*, Volume 40, Issue 5, October 2004, pp. 1333 - 1340

[68] K. Atallah, Z.Q. Zhu and D. Howe, "An Improved Method for Predicting Iron Losses in Brushless Permanent Magnet DC Drives", *IEEE Transactions on Magnetics*, Volume 28, Issue 5, Sept. 1992, pp. 2997 - 2999

[69] The Contract Heat Treatment Association, "Stress Relieving, Normalising and Annealing", *CHTA Datasheet for Non-Heat-Treaters*, 1996, pp. 1 - 2, http://www.chta.co.uk/downloads/data_3.pdf last accessed on March 2006

[73] MatWeb - Online Material Data Sheet, "DuPont Delrin® 500 NC010, Medium Viscosity Acetal", *http://www.matweb.com/search/SpecificMaterial.asp?bassnum=PDTAM029* last accessed on 1 February 2006

[74] S.M. Abu-Sharkh, "Propeller Hydrodynamics", Technical Note UVD01, *Design Studies of Power Electronic Drive Systems for the Thrusters of Unmanned Underwater Vehicles*, August 1993